High Energy Particles in Heavy Ion Collision & Solar Observation

Thesis for the Degree of Doctor of Philosophy (PhD)

Nour Jalal Abdulameer
Supervisor: **Balázs Ujvári**

UNIVERSITY OF DEBRECEN
Doctoral Council for Natural Sciences and Engineering
Doctoral School of Physics
Debrecen, 2025

Hereby I declare that I prepared this thesis within the Doctoral Council for Natural Sciences and Engineering, Doctoral School of Physics, University of Debrecen in order to obtain a PhD Degree in Natural Sciences at Debrecen University.
The results published in the thesis are not reported in any other PhD theses.

Debrecen, 2025.08.15

Signature of the candidate

Hereby I confirm that Nour Jalal Abdulameer candidate conducted her studies with my supervision within the Particle physics Doctoral Program of the Doctoral School of Physics between 2020 and 2025. The independent studies and research work of the candidate significantly contributed to the results published in the thesis.
I also declare that the results published in the thesis are not reported in any other theses.
I support the acceptance of the thesis.

Debrecen, 2025.08.15

Signature of the supervisor

High Energy Particles in Heavy Ion Collision & Solar Observation

Dissertation submitted in partial fulfilment of the requirements for the doctoral (PhD) degree

in Physics

Written by **Nour Jalal Abdulameer**, certified Ms.c. in Physics

Prepared in the framework of the Physics Doctoral School of the University of Debrecen
Particle physics programme

Dissertation supervisor: **Dr. Balázs Ujvári**

The official opponents of the dissertation:

Dr. .....
Dr. .....

The evaluation board:

Chairperson: Dr. .....
Members: Dr. .....
Dr. .....
Dr. .....
Dr. .....

The date and venue of the dissertation defence: Debrecen, 20. . .

Acknowledgment

To my supervisor Dr. Balázs Ujvári who have been a significant support, I am eternally grateful.

I would also like to sincerely thank Dr. Gábor David for his guidance throughout my research.

For all the ways they have helped me, my family, friends, and colleagues at the University of Debrecen and the Wigner Institute will always have my heartfelt gratitude.

Furthermore, I express my appreciation to the University of Debrecen, Stipendium Hungaricum, BNL Lab, and Stony Brook University for the excellent resources they provided.

Contents

List of Figures

List of Tables

Abstract

High-energy photons function as effective indicators across several physical processes, including ultra-relativistic heavy-ion (URHI) collisions and astrophysical events like solar flares, both fields depend on photons to investigate the underlying dynamics of energetic systems under severe conditions.

In solar particle events, photons provide insights into particle acceleration and magnetic reconnection. In high-energy nuclear collisions, direct photons serve as crucial probes for investigating the first phases of quark-gluon plasma (QGP) formation, due to their ability to escape the medium without strong interactions. This conceptual overlap motivates the investigation presented in this thesis, which focuses on direct photon and neutral pion production in relativistic heavy-ion collisions as a window into quantum chromodynamics (QCD) and parton energy loss.

The Standard Model is a theoretical framework in modern particle physics that explains the behavior and interactions of Elementary particles, including quarks, leptons, and gauge bosons, that are fundamental components in the study of QCD, which is the theoretical framework that clarifies the mechanisms behind the powerful interactions between quarks and gluons. QCD exhibits two fundamental characteristics: The terms "color confinement" and "asymptotic freedom" pertain to distinct topics within the field of physics. Quarks as well as the gluons exhibit color properties which usually restricted to exist within hadrons as color-singlet states. However, the strong coupling constant (α_s) decreases when this momentum transfer increases in high-energy reactions or in settings characterized by an exceedingly high temperature or density. Therefore, when the temperature of either density of a many-body hadronic structure rises, it is anticipated that it undergoes a phase transition through an individual type of existence in which both gluons and quarks become no longer contained. The state referred to here is commonly referred to QGP.

A state of matter is expected to be formed in ultra-relativistic collisions. Several tests with heavy ions were recently performed to identify distinctive indications of this state. The RHIC at Brookhaven National Laboratory (BNL) in the USA conducted Au+Au collisions at a center-of-mass energy for each nucleon ($\sqrt{s_{NN}}$) of 200 GeV. This thesis reports preliminary findings on a study that measured neutrality pions and direct photons during high-speed collisions between gold nuclei using the RHIC-PHENIX spectrometer. Both the pions and direct photons are observed at mid-rapidity with high transverse momentum (p_T) values of up to 20 GeV/c. The pion and direct photon production in Au+Au collisions are examined by comparing these results with run 4 data obtained from the same

experiment.

During high-energy gold-gold collisions, an impressive drop in neutral pion formation at high transverse momentum (p_T) is observed compared to the yield in proton proton collisions at identical centers of mass energy ($\sqrt{s}$), adjusted to the number of interactions between nucleons during gold-gold collisions. This suppression is significant, approximately five times, and remains nearly changing within the range of transverse momentum from around 5 to approximately 20 GeV/c. However, direct photon production in Au+Au collisions lines up with the p+p results scaled with the number of binary collisions. Considering how many high-p_T direct photon come from early hard scatterings, the suppression is understood as a result of parton energy exhaustion resulting from gluon bremsstrahlung in the dense medium. The neutral pion suppression pattern was compared to a theoretical calculation by I. Vitev using the GLV energy loss formalism. This comparison allowed for a quantitative estimation of the effective gluon density (dN_g^{eff}/dy) during this high-density substance produced in $\sqrt{s_{NN}} = 200\,\text{GeV}$ when two gold particles collide, which is approximately 1300^{+300}_{-100}. As a plasma dominated by gluons forms within a time frame of 0.6 femtoseconds, the resulting energy density is 18 (GeV/fm^3) [1].

This thesis examines the unique variables affecting photon generation and behavior across multiple fields, including electromagnetic processes in solar environments and partonic interactions in the quark-gluon plasma produced during heavy-ion collisions.

Keywords

Heavy Ion Collisions, Au+Au Collisions, Direct Photons, Neutral Pions (π^0), Dead Hot Map (DHM), Detector Calibration, Timing Calibration, Particle Flow, Coronal Mass Ejections (CMEs), Solar Energetic Particles (SEPs), Solar Cycle 25, Photon Production, Space Weather, High-Energy Physics, PHENIX Experiment.

CHAPTER 1

INTRODUCTION & THEORY

QCD is a non-Abelian theory of quantum fields that describes the strong interactions between particles. Investigating non-perturbative phenomena in QCD represents a primary objective in the field of URHI physics. During URHI collisions, a state of matter known as QGP forms [2], which allows for the investigation of the QCD phase transition. QGP describes an environment characterized by the absence of binding between quarks and gluons. At the very beginning of the universe, an extremely quick period after the Big Bang, such a situation was present.

Upon examining Fig. 1.1, you will observe a diagram having a specific focus regarding the QGP phase. The temperature is represented on the vertical axis, while the baryon density is shown on the horizontal axis. The baryon density is around 0.15 GeV/fm^3 (or 2.7×10^{14} g/cm^3), which is almost equivalent to the density of normal nuclear matter. What is the main point to be understood from this? QGP arises exclusively in conditions characterized by exceptionally high temperatures or densities.

Jet quenching is a notable effect of QGP in URHI collisions, where highp_T hadrons are observed to be suppressed compared to p+p collisions [3–6]. The significant decrease (approximately fivefold) of hadrons in the final state was initially detected at the RHIC during Au+Au collisions at a center-of-mass energy of $\sqrt{s_{NN}}$ = 130 GeV [7, 8] and 200 GeV [9], Subsequently, this phenomenon was also observed at the Large Hadron Collider during Pb+Pb collisions at a center-of-mass energy of $\sqrt{s_{NN}}$ = 2.76 TeV [10].

The experiments conducted at SPS/CERN in Pb+Pb collisions at a center-of-mass energy of $\sqrt{s_{NN}}$ = 17.3 GeV did not observe a significant suppression of hadrons. However, there was a slight indication of suppression in the high-p_T π^0 yield explored by the WA98 experiment [11].

As the universe expanded and cooled, quarks and gluons, the components of subatomic particles referred to as partons, were more scattered. A phase transition transpires. Particles combine and become confined inside colorless hadrons due to an increased binding force between them [12].

One might reasonably anticipate that the threshold collision energy, at which

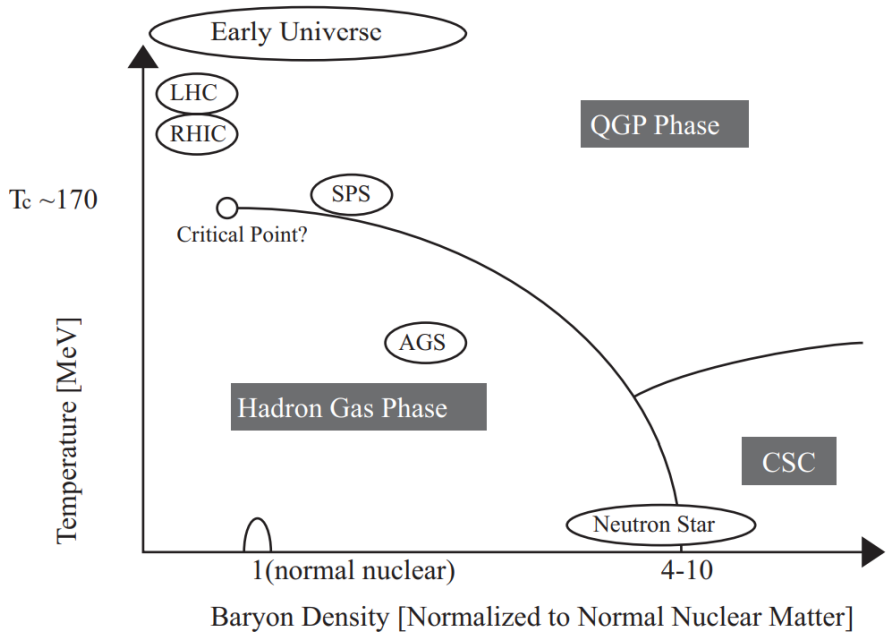

Figure 1.1: The simplified diagram showing the importance of hadronic phenomena includes the QGP.

the suppression of other nuclear effects becomes more significant, is going to be connected to the threshold energy required for the development of the QGP. The low-energy initiative was initiated by RHIC in 2010 with the purpose of studying the properties of QGP. The low-energy initiative at RHIC (or BES, Beam Energy Scan) was primarily not meant to study the properties of the QGP, but rather to find the threshold where it is beginning to form. You see, at SPS - 17GeV center-of-mass, c.m.s. energy - there was no QGP. At 200 GeV, the presence of QGP was clear. What BES aimed to do is to gradually reduce the c.m.s. energy, first to 62, then 39, then even lower, to see a point where the "onset" of QGP is clear - that will be the energy threshold.

1.1 The Purpose of the Research

This research focuses on the study of high-energy gold-gold (Au+Au) collisions at a center-of-mass energy of $\sqrt{s_{NN}} = 200$ GeV, conducted at the RHIC at Brookhaven National Laboratory (BNL). These collisions create an environment of extremely high energy density and low net baryon number at mid-rapidity, resembling the early universe microseconds after the Big Bang. Under such extreme conditions, it is possible to form a QGP—a state of deconfined quarks and gluons—which allows for detailed exploration of QCD in the non-perturbative regime.

The primary aim of this work is to investigate the production of neutral pions (π^0) and direct photons in central Au+Au collisions. Also, I addressed the centrality dependency of direct photon and π^0 generation. Neutral pions serve as an important probe of final-state effects, particularly jet quenching, which arises

from parton energy loss in the dense medium. Direct photons, on the other hand, interact only electromagnetically, making them largely immune to the strong interaction and allowing them to escape the collision zone without significant modification. As a result, direct photons provide a clean signal of the early-time dynamics and initial temperature of the medium [13].

Using high-statistics data from the 2014 RHIC Run, this study examines the transverse momentum (p_T) spectra of both π^0 and direct photons at mid-rapidity. Unlike previous works that relied heavily on next-to-leading order perturbative QCD (NLO pQCD) calculations, this analysis is grounded in experimentally measured baselines, allowing for a more direct assessment of medium effects.

The suppression of high-p_T π^0 mesons in central Au+Au collisions—as compared to binary-scaled p+p collisions—provides strong evidence for partonic energy loss in the QGP. In contrast, direct photons exhibit no such suppression, consistent with their early production and weak final-state interactions. By comparing the values of π^0 and direct photons, this study offers a quantitative evaluation of the medium's influence on high-energy partons, contributing to a better understanding of QGP opacity, energy density, and transport properties.

In addition to the high-p_T region, this research also explores the production of low-p_T direct photons. Although experimentally challenging due to large background contributions from hadronic decays, the detection of thermal photons at low p_T is particularly valuable. These photons are expected to originate from a thermalized medium and can thus provide evidence for the system reaching local equilibrium. Successfully isolating a thermal photon signal would yield key insights into the thermodynamic evolution of the QGP.

This thesis also draws a broader conceptual connection between photon production in high-energy nuclear collisions and in astrophysical phenomena such as solar flares and coronal mass ejections (CMEs). While these two research areas differ fundamentally in scale and environment—one taking place in controlled laboratory settings on Earth, the other occurring naturally in space—they both rely on high-energy photons as critical messengers of extreme physical conditions. In heavy-ion collisions, direct photons emerge during the earliest moments of the reaction, providing insight into the formation and properties of the quark-gluon plasma (QGP). Similarly, solar flares and CMEs accelerate particles to high energies and generate electromagnetic radiation across a broad spectrum, including X-rays and gamma rays. These photons offer vital clues about particle acceleration mechanisms, magnetic field dynamics, and energy release processes in the solar corona.

The study of such solar events has gained significant attention due to their profound impact on space weather and modern technology. Solar energetic particle (SEP) events, driven by CMEs and flares, can disrupt satellite operations, communication systems, and power grids. Therefore, understanding the physical conditions under which photons are produced in these cosmic environments is essential for improving predictive models and developing mitigation strategies for technological vulnerabilities [14].

By exploring the mechanisms that govern photon production in both nuclear and astrophysical contexts, this work emphasizes the universal role of high-energy

photons as probes of early-time dynamics in extreme environments. This cross-disciplinary perspective highlights how insights from nuclear experiments can inform space science, and vice versa, reinforcing the central importance of photons in advancing our broader understanding of energetic matter throughout the universe.

1.2 Dissertation Structure

The organization regarding the topics goes as the follows:

Chapter 1: Introduces the PHENIX experiment and the main objectives of the study, focusing on the quark-gluon plasma and core principles of QCD. Additionally, the chapter draws a conceptual link to high-energy solar phenomena, highlighting the shared role of photons as probes of extreme environments. It also presents the theoretical background and the use of high-p_T neutral pions and direct photons to probe the medium formed in heavy-ion collisions.

Chapter 2: In this section, we go into the details of the RHIC-PHENIX Experiment. Given that our investigation mainly relies on the EMCal detector, we will thoroughly examine its properties, also this section provides a detailed explanation of the beam condition, luminosity, and trigger circumstances that were present during the 2014 Au+Au runs.

Regarding The findings outlined in my dissertation will be structured into four key points.

Chapter 3: Data preprocessing. The data for Au+Au collisions in Run14 in PHENIX has been processed and organized. Initially, the concept of multiplicity is examined as a means of verifying the accuracy and reliability of the data. Additionally, a methodical examination of tower indexing in EMCal is conducted to facilitate the identification of non-functional or overheated towers, time calibration, and particle identification cuts. The transformations between various indexing standards have been presented in a chart. Furthermore, a comprehensive dead/hot map has been created for both datasets using energy selection. Subsequently, the time of flight (Tof) has been adjusted on a run-by-run basis to guarantee accurate timing for clusters and maintain the quality of the study. Finally, the study of Tof cuts to investigate the impact of overlapping occurrences and the use of PID cuts to remove hadron contamination has been completed. All the work mentioned above has been documented as an analytical note inside the PHENIX system. BigData2025, DHM2024, ToF2024 represent the publication for this section.

Chapter 4: This chapter presents a comprehensive study of neutral pion (π^0) and direct photon production in Au+Au collisions at $\sqrt{s_{NN}}$ = 200 GeV. It covers the extraction of raw π^0 yields through invariant mass reconstruction and

the application of corrections for detector acceptance, efficiency, and smearing via detailed simulations and response matrix unfolding. The analysis further investigates the centrality dependence of the γ/π^0 ratio, highlighting its relation to particle production at forward rapidity and medium formation in more central collisions. Direct photon invariant yields are studied after subtraction of decay photon backgrounds, focusing on high transverse momentum regions. These results are based on PHENIX Run14 data, with final validation and extended studies ongoing. Pi0PhotonAN1505, dAuCentrality2025 represent the publication for this section.

Chapter 5: Conclusion of the Au+Au collision analysis and outlook on future research directions

Chapter 6: The examination of high-energy solar particle events (SEPs), flares, and coronal mass ejections (CMEs) during Solar Cycle 25, exploring their sources, mechanisms, and impacts on space weather. It highlights correlations between these phenomena and the need for improved predictive models. SolarCycle25 represent the publication for this section.

1.3 Quantum Chromodynamics (QCD)

The Standard Model provides detailed descriptions of three out of all four basic interactions; namely the electromagnetic, strong, and weak forces. These interactions govern the behavior of fundamental particles that constitute everything that exists. A profound comprehension of the gluons and quarks, the most fundamental particles explained within the Standard Model, make up nuclei, which are formed of protons and neutrons [15].

Quark flavors that have been detected are listed in Table 1.1.

Flavor	Q	I	J	Iz	B	S	C	B*	T
up	$\frac{2}{3}$	$\frac{1}{2}$	$\frac{1}{2}$	$\frac{1}{2}$	$\frac{1}{3}$	0	0	0	0
down	$-\frac{1}{3}$	$\frac{1}{2}$	$\frac{1}{2}$	$-\frac{1}{2}$	$\frac{1}{3}$	0	0	0	0
strange	$-\frac{1}{3}$	$\frac{1}{2}$	0	0	$\frac{1}{3}$	-1	0	0	0
charm	$\frac{2}{3}$	$\frac{1}{2}$	0	0	$\frac{1}{3}$	0	1	0	0
bottom	$-\frac{1}{3}$	$\frac{1}{2}$	0	0	$\frac{1}{3}$	0	0	-1	0
top	$\frac{2}{3}$	$\frac{1}{2}$	0	0	$\frac{1}{3}$	0	0	0	1

Table 1.1: The properties of quarks include electric charge (Q), spin (J), isospin (I), the third component of isospin projection (Iz), baryon number (B), strangeness (S), charm (C), bottomness (B*), and topness (T) [16].

QCD is the fundamental theory of fields that discusses the strong nuclear interaction. Quarks, that are particles with a spin of $\frac{1}{2}$, carry one of three color charges. The charges had three names: blue, green, and red. Anti colors are carried by antiquarks. Eight linearly independent combinations of color and anticolor charge can be present in gluons, bosons that behave just like the carrier

of the strong force [17]. The dynamics of color charges is governed via the Lagrangian of QCD:

$$\mathcal{L}_{\text{QCD}} = \sum_{a,q} \bar{\psi}_{q,a} \left(i\gamma^{\mu}\partial_{\mu}\delta_{ab} - 4\pi\alpha_s \gamma^{\mu} t^{C}_{ab} A^{C}_{\mu} - m_q \delta_{ab} \right) \psi_{q,b} - \frac{1}{4} F^{A}_{\mu\nu} F^{A\mu\nu} \tag{1.1}$$

The strength of the strong interaction is represented by the component α_s in Eq. 1.1. The term "strong force" comes from it's magnitude, which stands around 1, meaning it's significantly larger to the coupling constants for the remaining three forces (gravity, electromagnetic, and weak).

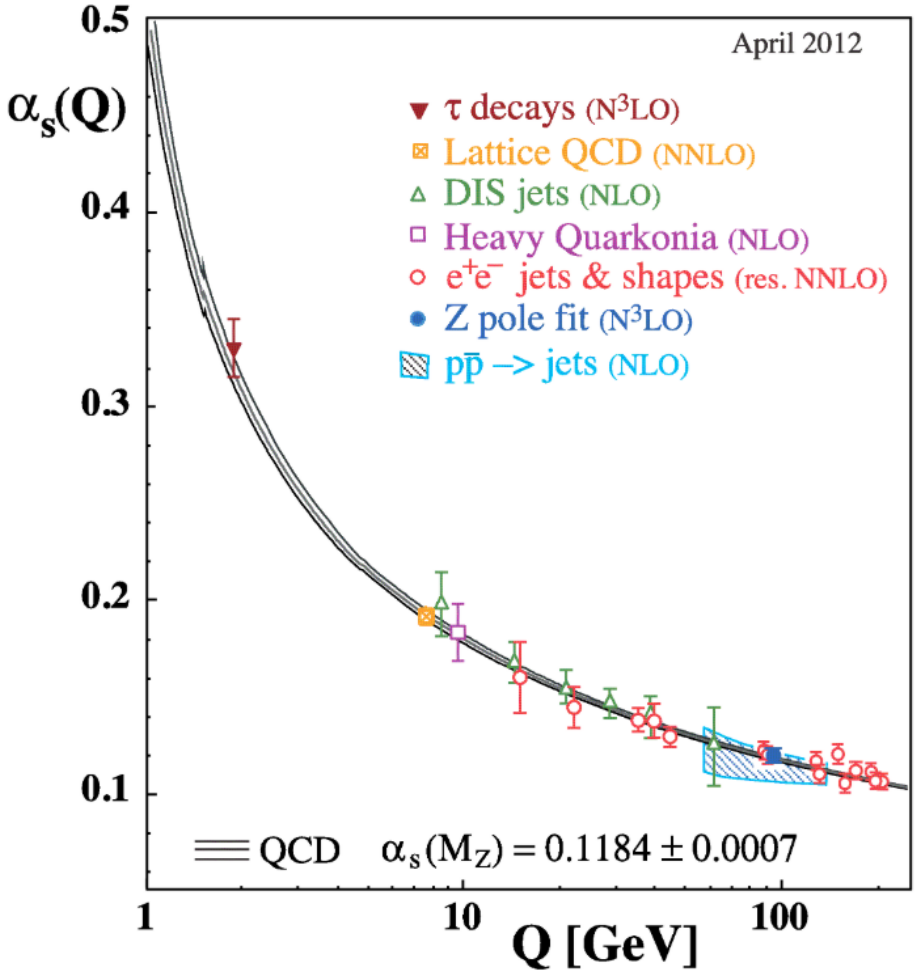

Figure 1.2: The relationship between the strong coupling constant α_s and the energy scale Q [18].

Depending on the amount of interaction energy or distance, α_s fluctuations in value. Fig. 1.2 illustrates the coupling constant's dependency on the energy scale, which has been measured in numerous studies. An interaction is weak at short distances and becomes stronger as the distance goes up. The energy of an operation can be defined as the inversely related of the length of time across where

the activity occurs. A term such as "asymptotic freedom" refers to this unique characteristic [19].

Here, (Fig. 1.2) a represents the color charge index, while q represents the quark flavor index [18]. QCD is a local SU(3) gauge theory that describes the relation between quarks and gluons. It is widely recognized that there is a valid hypothesis explaining the "strong force". Color confinement is a fundamental idea in QCD where quarks and gluons are restricted to exist only in hadrons as color singlet states. This means that although quarks and gluons have some freedom in their color properties, they are confined within hadrons [17].

An interesting fact that points to the possibility of the discovery of a new quark (c) is the discovery of bound states produced by heavy quark-antiquark pairings, such as J/ψ ($c\bar{c}$) and Υ ($b\bar{b}$). Up until now, we had only the light quark family, u, d, and s; J/Psi initiated the discovery of the heavy quark family (c, b, t). It also meant that, while the color SU(3) persisted, the taste SU(3) was no longer viable.

Using Stanford Positron Electron Asymmetric Rings (SPEAR), a e^+e^- collider at Stanford Linear Accelerator Center (SLAC), the massive $c\bar{c}$ meson state known as J/ψ was discovered in 1970s e^+e^- collisions [16].

This state was also observed in collisions of 28 GeV protons with a beryllium (Be) target using the Alternating Gradient Synchrotron (AGS) located at Brookhaven National Laboratory (BNL) [20].

The aspects that define nuclear matter at extreme densities and temperatures were of great significance even before the discovery of J/ψ [21], [22], [23]. It was suggested that a change in the vacuum's structure might correspond to the appearance of an unusual form of nuclear matter. The quark confinement phenomena arise from the non-perturbative structure of the vacuum. At elevated temperatures and/or densities, the arrangement of the vacuum undergoes alterations, resulting in the liberation of quarks and gluons from confinement. During the initial phases of QCD development, the concept of quark deconfinement was introduced.

Asymptotic freedom, which refers to a reduction in the strength of the interaction between particles at short distances, suggests that quarks and gluons would exist in a state of deconfinement and form an extremely dense nuclear substance at the core of neutron stars [24].

It was E.V. Shuryak [25] the first to conduct a comprehensive investigation of the high temperature state and coined the term QGP for this deconfined phase.

1.4 The Relativistic Heavy-Ion Collider (RHIC)

The purpose of the investigations is examining a series associated with QGP with their subsequent transition into hadronic matter by the collision of high-energy heavy ions. During these collisions, energy gathers in the area where the two nuclei collide, known as the overlapping zone. This energy can subsequently be utilized to generate quark-antiquark pairs and gluons. These particles have the potential of producing a QGP.

Prior research carried out at the BNL Alternating Gradient Synchrotron (AGS)

between 1987 and 1995, as well as at the CERN Super Proton Synchrotron (SPS) from 1987 onward, did not yield definitive proof of the presence of QGP. Indeed, science seems inherently focused on advancement, isn't it? The advent of the RHIC greatly expedited the progress of the program for heavy-ion research. The facility was originally purpose-built to carry out research on nuclear collisions at ultra-high speeds [26].

The RHIC, along with its four primary experiments, commenced successfully in the summer of 2000, as documented [27] [28] [29] [30]. Subsequently, they have been examining data obtained from Au+Au collisions at three distinct energy levels: The energy per nucleon pair is 62.4 GeV, 130 GeV, and 200 GeV, specifically indicated as $\sqrt{s\_NN}$ = 62.4, 130, and 200 GeV. In addition, they investigated p+p collisions at the same energy levels, as well as d+Au collisions with an energy of $\sqrt{s\_NN}$ = 200 GeV/c.

CERN and BNL have undertaken numerous experiments. A brief summary is shown in Table 1.2 [31].

Accelerator	Laboratory	Species	Particle Energy $\sqrt{s_{NN}}$ (GeV)	Year
SPS	CERN	^{16} O, ^{32} S	19.4	1986
SPS	CERN	^{208} Pb	17.4	1994
AGS	BNL	^{16} O, ^{28} Si	5.4	1986
AGS	BNL	^{197} Au	4.8	1992
RHIC	BNL	^{197} Au	130	2000
RHIC	BNL	^{197} Au	200	2001
RHIC	BNL	d+^{197} Au	200	2003
RHIC	BNL	^{197} Au	200, 62.4	2004
RHIC	BNL	^{63} Cu	200, 62.4	2005
RHIC	BNL	^{197} Au	200	2007
RHIC	BNL	d+^{197} Au	200	2008
RHIC	BNL	^{197} Au	200, 62.4, 39	2010
RHIC	BNL	^{197} Au	200, 27, 19.6	2011
RHIC	BNL	^{238} U	192	2012
RHIC	BNL	^{63} Cu+^{197} Au	200	2012
RHIC	BNL	^{197} Au	200, 14.6	2014
RHIC	BNL	^{3} He+^{197} Au	200	2014
LHC	CERN	^{208} Pb	2760	2010
LHC	CERN	p+^{208} Pb	5020	2012

Table 1.2: A comprehensive list of research on a high-energy heavy ion collisions [31].

Strong forces happening during the collision cause the nuclei to become extremely compressed and take on a flattened, pancake-like appearance at high speeds. It is interesting because it brings numerous particles into close proximity. When collisions occur, quarks and gluons, also known as partons, are released, resulting in the formation of a high temperature and compact substance termed QGP. Occasionally, the particles collide forcefully and rapidly veer off in a lateral direction. These entities provide us with information regarding the QGP.

While the collision was occurring, the QGP undergoes expansion and drops in the temperature, resulting in its transformation into a gas composed of hadrons. Partons undergo a transformation into hadrons and then move towards the detectors. During movement, larger objects can potentially decay into smaller fragments. The detectors notice these Partons displaying collective behavior, suggesting their origin from an area of high temperature. Figure 1.3 displays an image that represents all these steps.

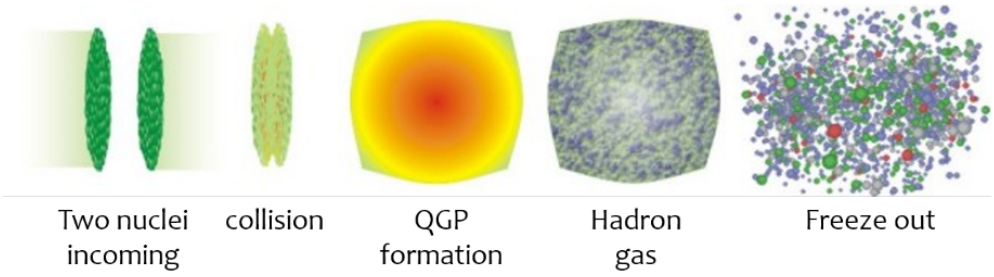

Figure 1.3: A diagram showing various phases of collisions between heavy ions within the framework of evolution. excerpts taken from several sources that are open to the public [31].

Additionally, they experience hadronization, which leads to the creation of jets—streams (It is important to note that all particles, not just jets, start from partons) of partons traveling collectively with the same energy as the original collision. The jets in basic proton-proton collisions have significant distinguishable. Nevertheless, what occurs when there are massive collisions involving heavy ions? The jets are hidden among several other particles.

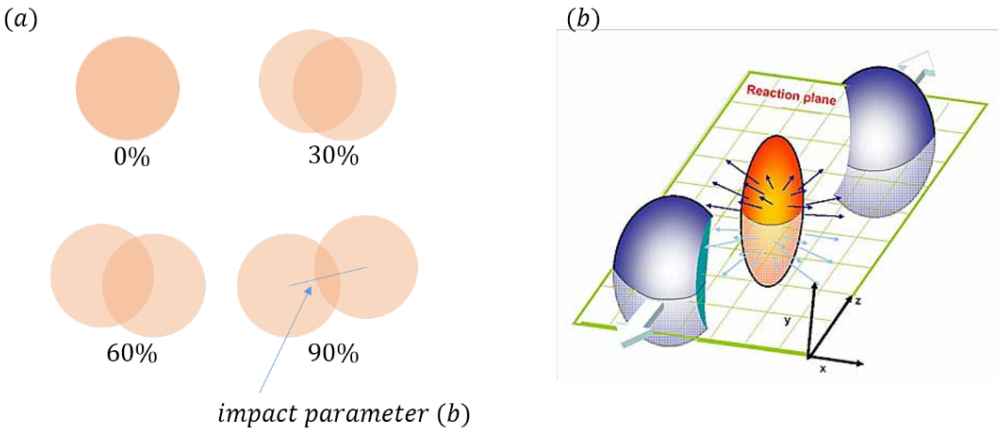

Figure 1.4: A picture displaying a reaction plane (b) and the notion for centrality (a). Selections taken from multiple publicly accessible scripts, such as [32].

When analyzing processes such as jet suppression, the jets themselves are of no use in determining the number of collisions (Ncoll) and the number of participating nucleons (Npart). Instead, these factors are often calculated using models such as the Glauber model, which study the collision based on the geometry of

nuclear overlap. Once Ncoll and Npart have been estimated, analyze the impact on jets, such as their suppression or modification, caused by interactions inside the quark-gluon plasma (QGP) that is created during the collision.

With regard to the size of the QGP, these quantities offer significant details and the abundance of particles within it. We utilize a metric known as centrality to quantify these factors. A 0% value indicates a collision when the objects collide directly with one another, while a 100% value indicates no collision whatsoever. Typically, this overlap appears in the shape of an almond. The orientation of this form is determined by the trajectory of the beam and the point at which the nuclei intersect (known as the impact parameter b) Fig. 1.4.

1.5 π^0 Production

Critical insights into the physics of the QGP can be gained from studying the formation of neutral pion (π^0) at high energy in heavy ion collisions. Measuring how neutral pions (π^0) are distributed in heavy-ion collisions involves reconstructing photons from their decay and analyzing their invariant mass to identify π^0 particles in the middle of other particles in the collision. In such experiments, indirect indicators like J/π^0 suppression, chiral symmetry restoration, strangeness amplification, and thermal radiation are key evidences supporting the existence of QGP [33].

In heavy-ion collisions, analyzing high p_T hadrons from hard scattering, hard scattering is distinguished by its momentum exchange taking place at a minute scale of $\frac{1}{p_T} \leq 0.1\,\text{fm}$, provides insights into the nuclear modification factor R_{AA}. This factor compares the yield of high p_T particles in heavy-ion collisions to that in proton-proton collisions, normalized by the number of binary collisions. If R_{AA} is less than unity, it indicates suppression of high p_T hadrons due to energy loss in the dense medium created during these collisions, revealing the quenching of parton energy as they traverse the QGP [34].

Approximately 99% of detected neutral pions (π^0)) decay into photon pairs, making them the primary source of inclusive photon signals. Given their prolific production following collisions, estimates based on π^0 already encompass the majority of decay photons, with eta (η) mesons making the next significant contribution [18]. Utilizing high-energy direct photons from these collisions can effectively verify scaling relationships dependent on the number of collisions.

1.5.1 Jet Quenching

When particles have high transverse momentum(p_T), they usually form in processes of hard parton-parton scattering. In the QCD vacuum, these distributed partons then split as jets in the QCD vacuum. When heavy nuclei collide [35].

Jets can help us look at the matter that gets involved in such collisions. Scientists believed that, as some research had suggested, there would be a significant loss of energy within this colorful environment. The back-to-back pattern of particle jets should be disrupted by this energy loss, leading to a phenomenon known

as jet quenching, as you can see in Figure 1.5.

That's actually one of the first hints scientists thought could point to a quark-gluon plasma. So, there are various ways (experimentally) to measure how much energy is lost. One way is to look at the suppression of particles with high transverse momentum (highp_T). Another way is by checking out changes in the shape of the jet itself. You can do this either through single jet measurements or by examining hadron-hadron correlations at high-p_T [36] [3] [37].

Compared to binary-scaled p+p collisions, the π^0 yield with Au+Au collisions at $\sqrt{s_{NN}}$ = 200 GeV strongly suppressed [38].

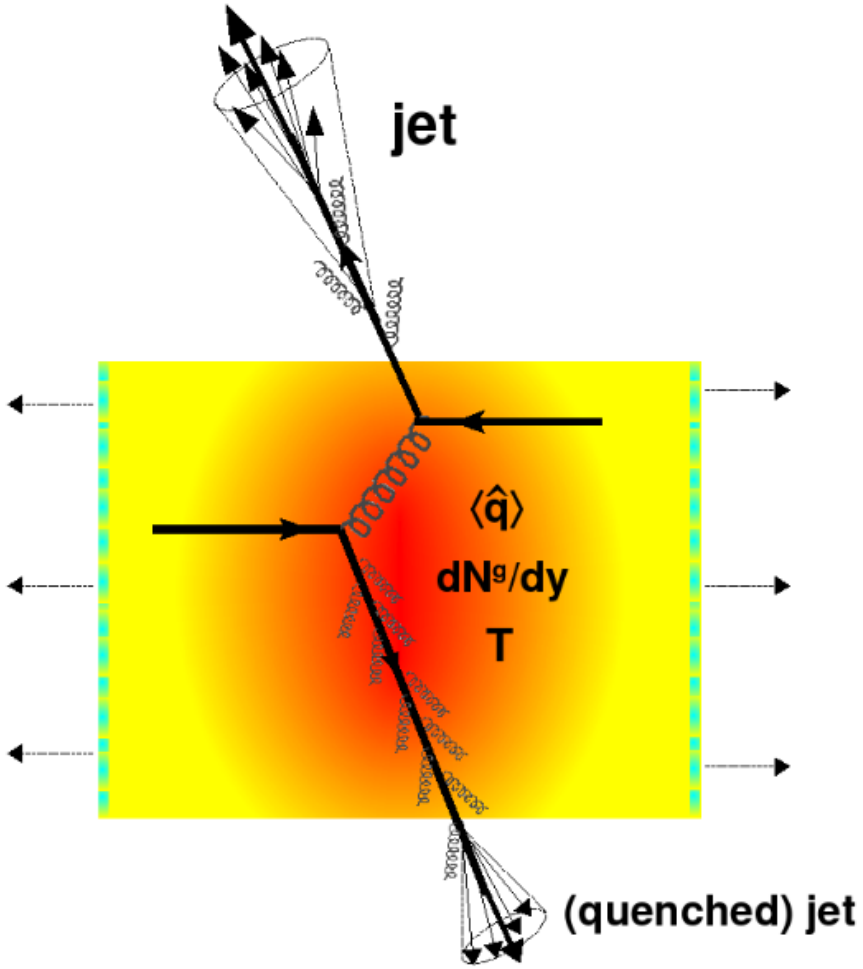

Figure 1.5: Diagram describing how energy is lost in a quark-gluon plasma (QGP) [36].

In comparison to p+p collisions, the yield π^0 in Au + Au collision is higher with low p_T [39].

Significant understanding of the characteristics of the quark-gluon plasma created in high-energy heavy-ion collisions at RHIC is gained from these measurements. Important indicators of the strongly interacting medium are the enhancement of low-p_T π^0 yields and the suppression of high-p_T π^0 yields.

1.5.2 Medium Alterations of Jets

Measuring particle correlations helps us to see more clearly how the medium affects jet energy. In this study, highly energetic hadron, leading hadron, marks the jet direction. For this particle, we check the differences in azimuthal angles of other highly energetic hadrons during the same event.

Collisions of both p+p and d+Au, two peaks pop up at 0° and 180°, as shown in Figure 1.6. These peaks are due to partons scattered back-to-back (due to momentum conservation) in hard collisions forming back-to-back correlations.

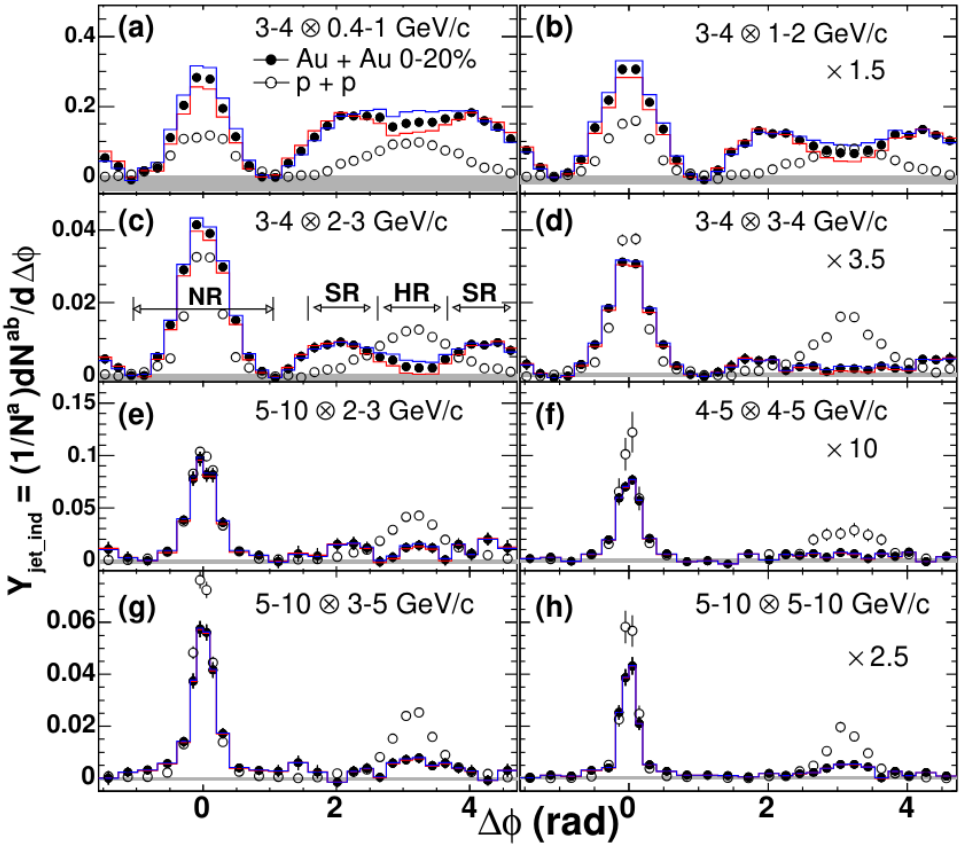

Figure 1.6: For different p_T-intervals, the PHENIX experiment examined the azimuthal correlation for charge hadrons for p+p as well as center Au+Au collisions [40]. Each panel has the pair of p_T and trigger p_T ranges supplied in the upper right corner.

Currently, in Au + Au collisions, the variation of the p_T range of associated hadrons shows a complex structure. At low p_T, the backside peak at $\phi = 180°$ spreads out significantly more than in p+p collisions. However, at higher p_T, that back peak dips in the middle. This dip can be a sign of the medium's reaction to the first parton's energy loss. Remarkably, that peak resurfaces at the highest connected p_T! This is often interpreted as the parton piercing through the medium [41, 42] [40].

1.6 Principles of Photon Production

Photons originate from four primary sources: the initial hard scattering among partons, the thermal generation within the hot medium, the interactions between hard partons and the medium, and the decay of hadrons such as π^0 and η into $\gamma\gamma$. Direct photons are defined as photons that do not originate from the decay of hadrons. Empirically observed photons represent the collective sum of all photons, making it difficult to discern their origins [43].

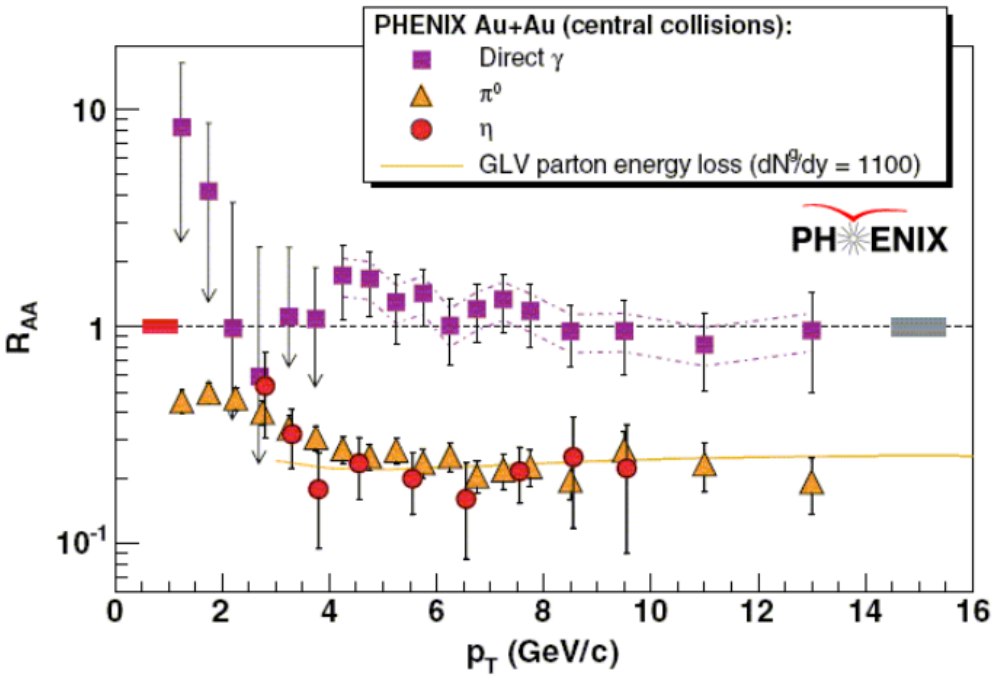

Figure 1.7: Photon nuclear modification factor for central Au+Au collisions as a function of p_T [44].

Because of their minimal coupling to the medium, photons make a good probe of the environment. Without interacting with the medium any further, the produced photons can exit it [13].

The diameter of the plasma created is $d_{\mathrm{QGP}} \approx 14\,\mathrm{fm}$ [45], whereas the mean free path of the photons is approximately $\lambda_{\mathrm{mfp}} \approx 100\,\mathrm{fm}$ [46].

There are several categories into which direct photons from nucleus-nucleus collisions can be set: Prompt photons can be produced in a variety of ways. They are caused by the initial collision and include parton hard interactions, quark-antiquark annihilation ($q + \bar{q} \rightarrow g + \gamma$), Bremsstrahlung emissions from quarks going through hard scattering ($q+q \rightarrow q+q+\gamma$), quark-gluon Compton scattering ($q + g \rightarrow q + \gamma$), and gluon fusion ($g + g \rightarrow \gamma$).

Thermal photons are released from the matter in high-energy heavy-ion collisions because the collision process creates a highly heated medium with free charges. Analyzing the medium's evolution is crucial. Thermal photons are classified as follows: those originating from partons scattering in the QGP phase (e.g.,

$q + \bar{q} \rightarrow g + \gamma$); and those originating from hadrons scattering in the hadron phase of gas (e.g., $\pi^+ + \pi^- \rightarrow rho + \gamma$) [47].

Additionally, there is a source of photons produced by the medium's interaction with hard particles. These photons are anticipated to yield data on jet energy loss within the medium. As expected, the photons found in the following picture should not exhibit any high p_T suppression at all. Until recently, PHENIX data revealed that this was the case, as the figure 1.7.

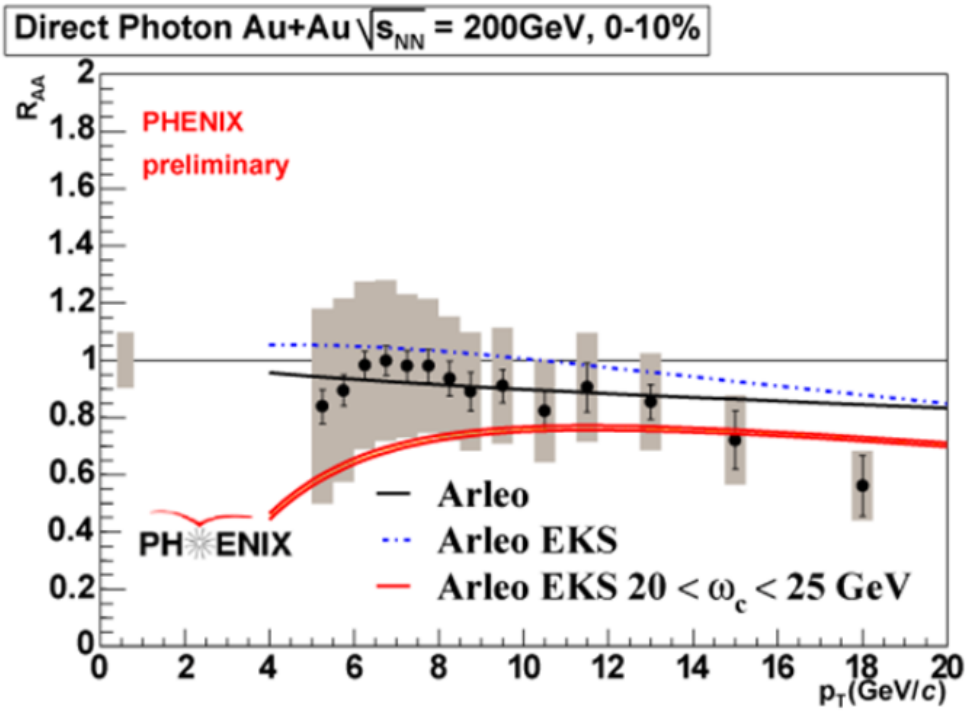

Figure 1.8: The BDMPS model of energy loss was used to compare the preliminary findings regarding the nuclear modification factor R_{AA} with photons to be a function of p_T with central Au+Au collisions with the assumption we made [48].

It would seem reasonable to expect the photon sample's bremsstrahlung component to show the same suppression seen in hadronic spectra as no isolation condition is applied to this data. There is evidence from more recent preliminary data, as seen in figure 1.8, indicating $R_{AA} < 1$; however, this effect is only meaningful at the highest p_T data level. In addition, an assumed prediction that accounts for energy loss is presented, derived using the BDMPS framework [49].

The model accurately describes every aspect of the data, although its explanation of the shape is only partially satisfactory. It is not surprising that there may be new sources for photons in nuclear collisions that were not considered in this particular model, even if we disregard the uncertainties in the energy-loss calculations.

1.7 Earlier achievements

Direct photon observations in p+p collisions have been carried out by several experiments, including UA6 [50, 51], WA70 [52], NA24 at CERN-SPS [53], R110 [54], R806 at CERN-ISR [55], and E706 at FNAL-Tevatron [56]. UA6 at CERN-SPS [50, 51], UA1 [57]and UA2 [58] at CERN-Sp$\bar{p}$S, and CDF [59] and D0 [60]at FNAL-Tevatron conducted measurements of direct photons within p+$\bar{p}$ collisions. Multiple articles provide a comprehensive analysis of direct-photon data [61, 62] [63].

It is challenging to quantify direct photons in relativistic heavy ion collisions due to significant interference from neutral meson decays, namely π^0 and η. The estimated signal-to-noise ratio at RHIC energy levels is about 10% in the p_T range of 2-4 GeV/c, while thermal photons are considered the dominant contributor.

The endeavor to quantify direct photons in heavy-ion collisions commenced during the CERN-SPS era. HELIOS / NA34, WA80 and CERES / NA45 experiments examined the generation of photons directly from p, O, and S beams with an energy of 200 AGeV ($\sqrt{s_{NN}}$ = 19 GeV) on targets C, Pt, Au, and W [64, 65] [66]. The direct photon spectra for O+Au collisions were constrained by setting upper bounds at a 90% confidence level (C.L.).

The WA98 experiment, which originated from WA80, conducted a further investigation by quantifying photons, π^0s, and ηs in fixed target ^{208}Pb+^{208}Pb collisions at 160 AGeV/c ($\sqrt{s_{NN}}$ = 17 GeV) using a high granularity lead glass calorimeter. An abundance of direct-photon signals was detected within the 2.0 < p_T < 3.5 GeV/c range [67].

Theoretical simulations, derived from photon measurements, provide evidence for the appearance of a high temperature ranging from 200 to 330 MeV at SPS energy [68, 69] [70, 71]. Srivastava and Sinha found that the data was accurately described by a brief initial thermalization time of τ_0 = 0.2 fm/c for the first Quark-Gluon Plasma (QGP) stage with a proportionally increased temperature that was 335 MeV [72].

Nevertheless, the validity of the thermalization time is uncertain due to the fact that the crossing times of Pb+Pb collisions are around 1.6 fm/c, which contradicts the estimated thermalization time. Comprehending the dynamics of the hadron gas is essential to comprehend the increased yield at low transverse momentum (p_T) [73, 74] [75].

CHAPTER 2

EXPERIMENT CONFIGURATION

An outline of the RHIC [76] is given in this section. The US Brookhaven National Laboratory (BNL) constructed the RHIC, which was first suggested in 1983. Launched at RHIC in early summer 2000, the PHENIX experiment is named after the pioneering study of high-energy nuclear interactions. Its aim is to investigate possible signatures of quarks and gluons in collisions with heavy ions.

2.1 RHIC Installation

RHIC located at BNL, It is an advanced investigation center designed especially to study nuclear material in exceedingly challenging circumstances. RHIC is a particle accelerator that can accelerate heavy ions up to 100 GeV per nucleon and protons up to 250 GeV.

Table 2.1: RHIC Heavy Ion Run Parameters and Performance

Parameter	**Value**
Injection Energy	γ = 10.25 (p = 9.5 GeV/c per nucleon)
Energy Storage	γ = 107.4 (p = 100.0 GeV/c per nucleon)
Number of Particles per bunch	1.0×10^9 Au ions per bunch
Number of Bunches	56 filled
Transverse Emittance	15π μm (normalized, 95%)
Longitudinal Emittance	0.3 eVs per nucleon per bunch
Interaction Diamond Length (r.m.s.)	20 cm
Nominal (Max) Crossing Angle	0 (up to 1.7) mrad
Bunch Length	15 cm
Bunch Radius	0.2 mm (β^* = 1)
Luminosity Lifetime	3 hours

One of its distinctive features is the capacity to accelerate polarized protons for the purpose of studying proton spin. The yellow and blue rings, which make up

the RHIC, are two rings that accelerates particle traveling in opposite directions toward one another.

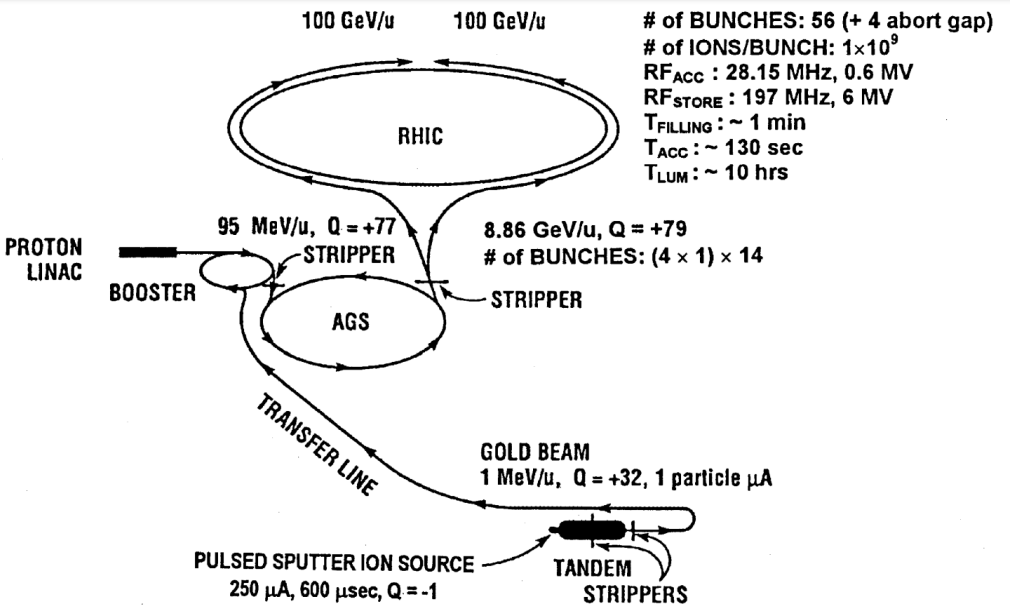

Figure 2.1: View of the RHIC accelerator system from above [77].

The source generates heavy ions, which are subsequently directed through the Alternating Gradient Synchrotron (AGS), booster accelerator, and Tandem Van-de-Graaff before entering the RHIC ring (See Figure 2.1). They reach velocities of 99.95% of the speed of light in the RHIC ring. Numerous collision systems, including Au + Au, p + p, d + Au, Cu + Cu, U + U, and Cu + Au, have been the subject of research conducted by RHIC. Attempting to achieve a luminosity of 2×10^{26} cm^{-2}s^{-1} for heavy ions and 2×10^{32} cm^{-2}s^{-1} for polarized protons, the collider has a ring whose length is 3.8 km and can hold up to 120 bunches. The table 2.1 provides a summary of the parameters achieved for the RHIC heavy-ion run [78].

2.2 PHENIX

The PHENIX (Pioneering High Energy Nuclear Interaction eXperiment) detector is located at one of the six intersection points of the RHIC at BNL [79].

PHENIX aims to investigate the properties of QGP, a form of matter believed to have emerged in the early stages of the universe, by analyzing collisions between high-energy heavy ions. The PHENIX detector is capable of measuring a wide range of particles and electromagnetic phenomena that result from these collisions.

Its capabilities include the precise measurement of hadrons, leptons, and photons over a large solid angle, which is essential for comprehensive studies of the QGP. Figure 2.2 shows the PHENIX spectrometer setup viewed both from the beam direction and the side.

Subsystem	Rapidity Coverage	$\delta\phi$	Purpose and Features
Beam Beam Counters	$3.1 < \|\eta\| < 3.9$	2π	Minimum bias trigger Vertex Reaction plane determination Start timing
Zero Degree Calorimeter (ZDC)	± 2 mrad ($\|\eta\| \geq 6$)	2π	Minimum bias trigger
Central Magnet	$\|\eta\| < 0.35$	2π	Up to 1.15 T·m
South Muon Magnet	$-2.2 < \eta < -1.1$	2π	
North Muon Magnet	$1.1 < \eta < 2.4$	2π	
Drift Chamber(DC)	$\|\eta\| < 0.35$	$\pi/2 \times 2$	Momentum measurement $\delta m/m = 0.4\%$ at $m = 1$ GeV
Pad Chamber(PC)	$\|\eta\| < 0.35$	$\pi/2 \times 2$	Track matching
Time Expansion Chamber(TEC)	$\|\eta\| < 0.35$	$\pi/2$	Track matching
Ring Imaging Cherenkov Detector(RICH)	$\|\eta\| < 0.35$	$\pi/2 \times 2$	Electron ID
Aerogel Detector(AGEL)	$0 < \eta < 0.35$	$\pi/4$	High-p_T hadron ID
Time Of Flight (TOF)	$\|\eta\| < 0.35$	$\pi/4$	Hadron ID $\sigma < 100$ psec
Electromagnetic Calorimeter	$\|\eta\| < 0.35$	$\pi/2 + \pi/4$	Energy measurement
Lead-Scintillate	$\|\eta\| < 0.35$	$\pi/2 + \pi/4$	Fine granularity
Lead-Glass	$\|\eta\| < 0.35$	$\pi/4$	
Muon Tracker(MuTr)	$-2.25 < \eta < -1.1$ $1.15 < \eta < 2.44$	2π 2π	Momentum measurement
Muon Identifier(MuID)	$-2.25 < \eta < -1.15$ $1.15 < \eta < 2.44$	2π 2π	Muon ID

Table 2.2: A brief description of the PHENIX environment.

The z-axis aligns with the beam axis, with angle θ used for pseudorapidity. Two central spectrometers are nearly back-to-back in azimuthal angle ϕ, improving coverage by avoiding blind spots. Central spectrometers cover ± 0.35 pseudorapidity; beam detectors and muon spectrometers cover $\pm(1.2 - 2.4)$. See Table 2.2 for subsystem details.

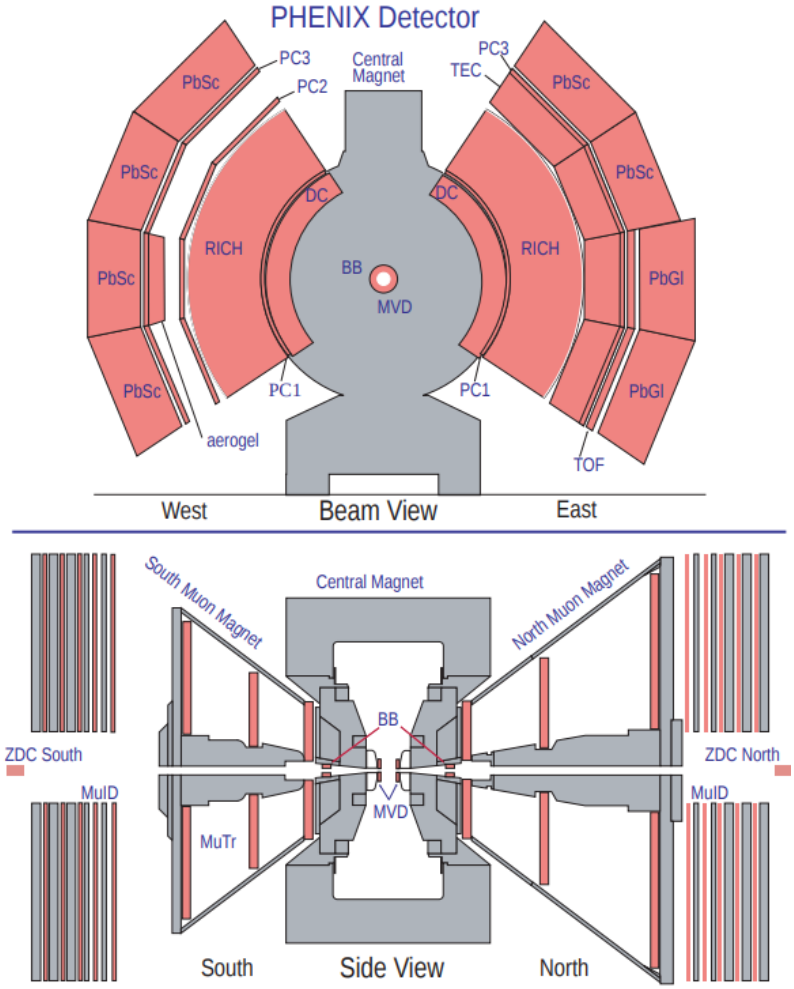

Figure 3.2: The PHENIX setup during the fourth RHIC beam period.

Figure 2.2: Setting up the PHENIX detector.

Tracking

Tracking begins at the Drift Chamber (DC) near the magnetic field boundary, measuring charged particle deflection with about 150 µm precision in the r-ϕ plane. The momentum resolution for $\pi^{\pm}$ is given by:

$$\frac{\delta p}{p} = 0.7\% \oplus 1.0\% \times p\,(\mathrm{GeV}/c).$$

The DC provides tracking data used for pattern recognition in other central arm detectors such as Pad Chambers (PC) and Time Expansion Chambers (TEC). PCs are multiwire proportional chambers positioned at various angles relative to the beam [80]. Further technical details are summarized in [81].

Particle Identification

PHENIX excels in electron detection, especially at high-p_T, primarily using the Ring Imaging Cherenkov (RICH) detector, which contains 40 m^3 of CO_2 gas with

refractive index $n - 1 = 4.1 \times 10^{-4}$. Charged particles faster than light in the medium emit Cherenkov radiation, forming rings focused onto photomultipliers. Pions below 4.65 GeV/c do not produce Cherenkov light [82].

The Time Of Flight (TOF) spectrometer, with ~100 ps timing resolution, distinguishes protons and kaons up to 4 GeV/c and pions and kaons up to 2.4 GeV/c. Located before the lead-glass calorimeter, the TOF measures particle flight time for charged particle identification.

Calorimetry

The central tracking system ends with lead-scintillator (PbSc) and lead-glass (PbGl) calorimeters, providing high-resolution energy and position measurements with fine segmentation ($\Delta\eta \times \Delta\phi \approx 0.01 \times 0.01$).

2.3 EMCal

The Electromagnetic Calorimeter (EMCal) [83] detects photons from neutral decays and is vital for this analysis. It consists of eight sectors: six lead-scintillator (PbSc) sampling calorimeters and two lead-glass (PbGl) Cherenkov calorimeters. PbSc offers excellent linearity, timing, and hadron response, while PbGl provides superior granularity and energy resolution.

Designed for energies from hundreds of MeV to 80 GeV, EMCal achieves 2% precision for single photons and 10% for π^0 cross sections. Its fine segmentation ($\Delta\eta \times \Delta\phi \approx 0.01 \times 0.01$) maintains low occupancy in central Au+Au collisions. Combining PbSc and PbGl enables high-quality measurements and systematic cross-checks.

	PbSc	**PbGl**
Type	Scintillator+Lead	Cherenkov
Radiation length (X0) [mm]	21	29
Moliere radius [mm]	30	37
Cross section of a channel [mm^2]	52.5 × 52.5	40 × 40
Depth [mm (X0)]	375 (18)	400 (14)
$\Delta\eta$ of a channel	0.011	0.008
$\Delta\phi$ of a channel	0.011	0.008
Number of channels in a super-module	144 (12 × 12)	24 (4 × 6)
Number of super-modules in a sector	18 (3 × 6)	192 (12 × 16)
Number of total sectors	6	2
Number of total channels	15552	9216

Table 2.3: EMCal subsystem.

2.3.1 PbSc

For the PHENIX experiment, a PbSc electromagnetic calorimeter was used [84]. It is a shashlik-type detector with 15,552 individual towers spanning an area of around 48 m^2. PHENIX is divided into two sectors in the east arm and four sectors in the west central arm. By gathering scintillation light produced at different depths within the detector, PbSc is mainly used to calculate the energy deposited by a particle.

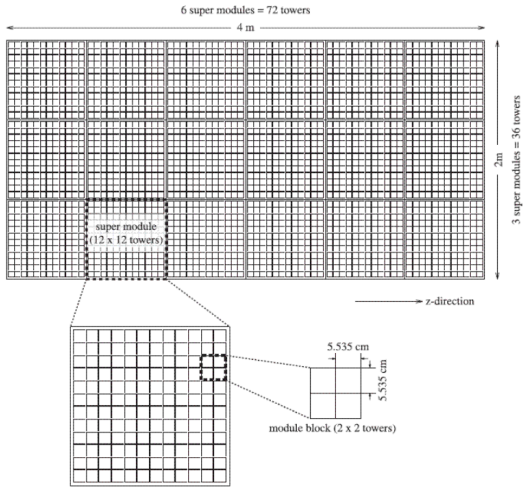

(a) The graphic shows the top-down perspective for a 6x3 super module-based PbSc sector. Towers stacked in a 12 x 12 pattern make up a super module.

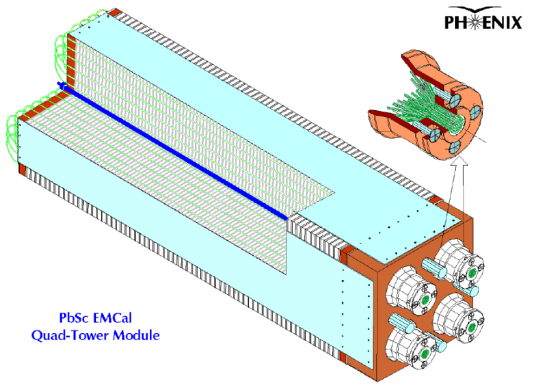

(b) A PbSc calorimeter module, consisting of four towers, is depicted in the figure. A photomultiplier tube (PMT) is connected to wavelength-shifting fibers that have been introduced through layers of lead and scintillator tiles.

Parameter	**Value**
Lateral segmentation	5.535 × 5.535 cm^2
Active-sampling cells	66
Scinti-llator	Poly-styrene (1.5% PT/0.01% POPOP), 0.4 cm
Absorber-	Pb, 0.15 cm
Cell-thickness	0.56 cm (0.277 X_0)
Active-depth	37.5 cm
Radiation-length	18 X_0
Nuclear-interaction-length	0.85
WLS-fiber	BCF-99-29a, 0.1 cm
WLS-fibers per-tower	36
PMT-type	FEU115M, MELS, Russia, 3.0 cm
Photo-cathode	Sb-K-Na-Cs
Luminous-sensitivity	> 80 μa/lm
Rise-time (20-80%)	6.5 ns

Table 2.4: The Pb-scintillator calorimeter's individual tower parameters.

As shown in Fig. 2.3b, a PbSc module consists of four optically isolated towers, each with a 5.54 cm × 5.54 cm area. Eighteen supermodules (6 × 3) form a

sector (Fig. 2.3a), with six × six building blocks per supermodule. These are fixed together with stainless steel skins for rigidity.

Each tower has 66 lead and scintillator sampling cells, edge-plated with aluminum and connected by 36 wavelength-shifting fibers. Scintillation light is detected by 30 mm FEU115M phototubes. The organic scintillator includes POPOP and PT additives.

Beam tests at U70, AGS, and SPS showed an energy resolution of:

$$\sigma(E)/E = \frac{8.1\%}{\sqrt{E/\mathrm{GeV}}} \oplus 2.1\%$$

Constant term effects arise from shower depth variations, fiber hot spots, and tower boundaries.

2.3.2 PbGl

Quantity	**Value**
Geometry	384 Super Modules
Number of SM per sector	192 (16 wide by 12 high)
Number of modules per SM	24 (6 wide by 4 high)
Total number of modules	9216
Module front surface	4 cm × 4 cm
Module length	40 cm ($14.4X_0$)
Mylar foil thickness	12 µm
Shrink tube thickness	150 µm
Super module front surface	24.6 ± 0.02 cm × 24.6 ± 0.02 cm
Pb glass type	TF1
Pb oxide content	51%
Density	$3.85 g/cm^3$
Weight per module	2.46 kg
Index of refraction	1.648
Total internal reflection angle	36°
Radiation length X_0	2.8 cm
Moliere radius	3.68 cm
Interaction length	38.0 cm
Critical energy	16 MeV

Table 2.5: PbGl features.

The PbGl calorimeter, first used in the WA98 experiment at CERN [85] to measure direct photons, was later installed in PHENIX's east central arm as two sectors. Each sector contains 192 supermodules (SM), each with 24 PbGl modules arranged in a 6×4 array (see Fig. 2.4). Modules are wrapped in carbon fiber and epoxy, with integrated phototubes and LED gain monitoring.

Energy resolution is parametrized as $\sigma(E)/E = (5.9 \pm 0.1)\%/\sqrt{E/\text{GeV}} \oplus (0.8 \pm 0.1)\%$, and position resolution as $\sigma_x(E) = (0.2 \pm 0.1)\,\text{mm} \oplus (8.4 \pm 0.3)\,\text{mm}/\sqrt{E/\text{GeV}}$, with negligible angular dependence [83].

Table 2.5 summarizes physical properties. Performance was validated through beam tests at AGS (BNL) and SPS (CERN) [86].

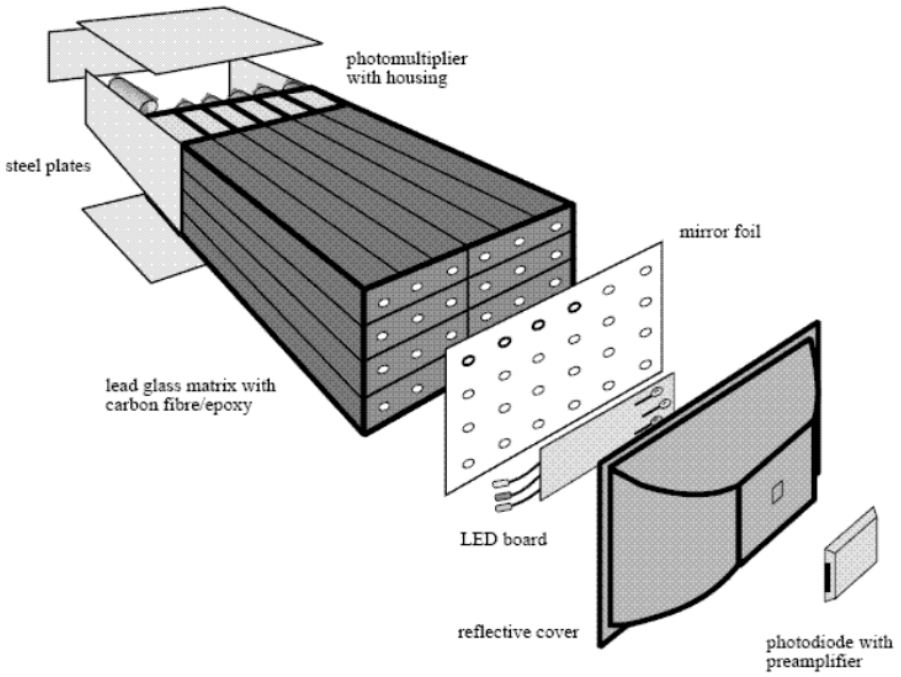

Figure 2.4: Diagram of a PbGl supermodule (SM).

2.4 Taxi Job Applications

The term "taxi job" refers to a specific type of automated task designed to fetch and process data in the context of large-scale data analysis, it is involves the following steps:

1. Data Retrieval: Automatically accessing data stored in databases.

2. Data Processing: Running predefined scripts or algorithms to analyze the data, such as generating dead hot map (3.2, we will present a concise explanation of the DHM (Dead Hot Map). This process entails extracting the required data to remove a bad run number (see the list 2).

3. Job Management: Submitting and managing these tasks on a computing cluster, ensuring efficient use of computational resources.

4. Output Generation: Producing results in the form of processed data can be used for further analysis as an input file (listed in 1).

2.5 Preparation and Implementation of Triggers

The PHENIX data acquisition system has a restriction on its capacity. We utilize the scaled-down or prescale method to selectively filter out physically significant collisions, events. In this analysis, I specifically concentrate on the important triggers (MB, ERT).

2.5.1 MB Trigger

The BBCLL1 trigger in PHENIX utilizes the Beam-Beam Counter (BBC) that provide us with valuable information on the centrality of the event, positioned at a symmetrical distance of 144 cm within the pseudorapidity range of $3.0 < |\eta| < 3.9$. The BBC is crucial for event selection and vertex determination [87].

For BBCLL1 to be considered valid, it requires a coincident signal in both the North and South BBC detectors, then we can have the vertex cut of $|z| < 30cm$. BBCLL1 variants such as BBCLL1(> 0tubes) novertex and BBCLL1(> 0 tubes) narrowvtx modify the criteria for the vertex, whereas BBCLL1(> 1 tubes) central narrowvtx and BBCLL1(> 1 tubes) central novertex modify the conditions for the number of hits and the vertex. BBCLL1 N(> 1 tubes) specifies numerous hit conditions without any extra restrictions on the vertex.

BBC > 0 (Minimum Bias) triggers are activated when there is at least one detection in both BBC detectors, selecting just 93% of all inelastic collisions. For the vertex position to be valid, the absolute value of z must be less than 20 cm. Like BBCLL1, BBC > 0 without a vertex and BBC > 0 with a narrow vertex can be used to loosen or define alternative vertex conditions.

These triggers play a crucial role in the selection of events that are of interest and are often used in PHENIX analysis.

2.5.2 ERT Trigger

The EMCal RICH Trigger (ERT) is a trigger that combines triggers. One ring is reported by RICH and one cluster is reported by EMCal. The ERTLL1: EMCal RICH Trigger is specifically developed to detect and record high transverse momentum (pT) occurrences. We selected 2x2 or 4x4 tiles to examine if the energy deposit would be added up to surpass a certain threshold or not.

Table 2.6: Threshold values for triggers in Au+Au collisions during Run14 were determined using DAC values for PbSc and PbGl detectors.

Trigger	Condition
ERT4×4a & BBC less than 0	31/30
ERT4×4b	32/31
ERT4×4c& BBCless than 0 (narrow)	30/29

Three thresholds are selected for the tiles 4×4: ERT LL1 $4\times4a$, ERT LL1 $4\times4b$, and ERT LL1 $4\times4c$. Typically, in PHENIX, a 4×4 ERTLL1 trigger is frequently used in conjunction with the BBCLL1 trigger. A tile calculation 2×2 is commonly used

as a requirement for an ERT LL1 E trigger for electrons. The energy thresholds for the Run14AuAu experiment are presented in table 2.6. ERT4 $\times$ 4 is activated when the energy deposited in a tile (a4 $\times$ 4tower array) surpasses a certain limit.

CHAPTER 3

DATA CALIBRATION

In advance of establishing any significant visualizations of physics, it is essential to calibrate and enhance the data. This analysis of Run14 gold-gold collision data involves an extensive amount of data that has not been addressed in previous years.

Therefore, it is essential to identify the "defective" towers and just use the "efficient" towers for our research. The towers considered "defective" are identified as the Dead Hot Map (DHM) in this statement. This DHM principally includes two groups of malfunctions as suggested by its name. When the tower fails to responds or just partially responses, it becomes known as the Dead Tower. In calorimeter-based investigations, a “Hot” tower describes a detector channel that displays an unusually elevated signal rate. This may result from electronic noise, hardware failures, or radiation damage; in summary, they produce signals without an energy deposit. Such towers can affect energy measurements and negatively impact the precision of direct photon studies. Consequently, recognizing and rectifying hot towers is crucial for preserving data integrity.

A precise time calibration is necessary to differentiate between a hadron traveling the calorimeter and generating a signal, and a photon, since hadrons show slower velocities. With an accurate timing calibration, I can effectively discriminate between a photon cluster and a hadron cluster. In my work with π^0, I consistently utilize two clusters; however, when dealing with a direct photon, there were only one cluster used. Therefore, it is necessary to confirm that the detected signal is indeed a photon and not a hadron that gives a photon-like cluster. Within a quark-gluon plasma, the prevalence of hadrons results in numerous false clusters in the calorimeter, similar to those produced by π^0. Consequently, it is essential to eliminate these false signals, and one effective method for limiting the hadronic background is through timing calibration (time-of-flight cut).

3.1 DHM Calibration

A technical note for Run 14 Au+Au (Check out the details here. [88]) explains in detail the procedures for the Dead Hot Map (DHM) calibration, which is the initial step in gathering data for the analysis. It applies quality cuts and processing data for every run.

3.1.1 THMulf

The THmulf class was developed to create a DHM by combining compact distribution shapes with projection capabilities based on selection criteria. Before ROOT's THnSparse, sparse histograms like THmulf were essential for high-dimensional data analysis [89].

3.1.2 Identifying and Managing Malfunctioning Towers

The EMCal comprises 8 sectors: six (0–5) made of lead-scintillator (PbSc) with 36×72 towers each, and two (6–7) made of lead-glass (PbGl) with 48×96 towers each.

No detector is perfect, and malfunctioning towers can significantly impact analysis. Identifying "defective" towers—referred to as DHM—is essential. Identification relies on statistical analysis assuming uniform particle distribution across towers over many collisions, adjusted slightly for pseudorapidity effects. Significant deviations in hit counts (too low or too high) indicate problematic towers. Establishing thresholds is difficult because of steep energy spectra and intrinsic low-energy noise, which, if randomly removed, could reduce detection efficiency and measurement quality.

Our methodology examines many parameter configurations to assess outcomes instead of establishing strict thresholds in advance. This strategy is based on an assumption that physical quantities (e.g., π^0 or direct photon yields) exhibit smooth variation. If the narrowing of the DHM results in the exclusion of more towers while maintaining similar spectral shapes and ratios, such exclusions are unjustified, signifying an unnecessary loss of acceptance.

3.1.3 Generate DHM

The first step in our statistical preparation is to extracts DHM statistics for each run. Merging these results yields integrated histograms covering all runs. Section 3.2 provides a brief overview of the macro's workflow.

1. Multiple parameters are used for quality assessment. A "run" is a continuous data collection period, typically about one hour, with run numbers increased automatically by the run control software. Not all runs are "physics runs" (actual collision data); some are calibration or subsystem test ("junk") runs. Fig. 3.1(a) shows run numbers versus event counts. Runs with fewer than 1 million events often indicate sub-detector issues and are excluded

from DHM generation. Fig. 3.1(b) plots existing runs; bins with entries correspond to existing runs, empty bins indicate missing runs.

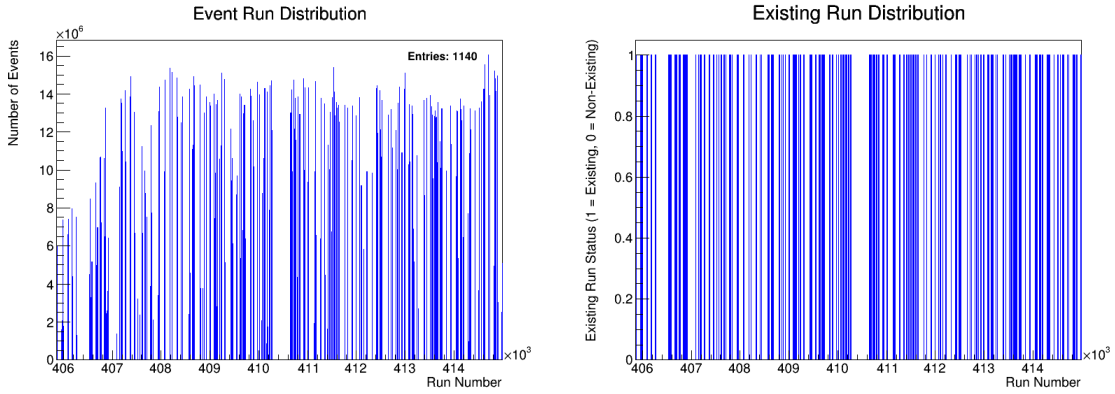

(a) Event statistics per physics run **(b)** Available physics run numbers

Figure 3.1: (a) Explanation on the quantity of events for every "physics run". (b) Available physics run numbers, irrespective of data quantity.

2. Quality cut: runs with fewer than 20 clusters per event in any sector are marked as "fail quality Low Hit Per Event Run" with a value of 1. Multiple sector failures show significant sector non-functionality. The ideal segmentation of 20 clusters per event is determined from the cluster distributions shown in Fig. 3.2(a) for PbSc and Fig. 3.2(b) for PbGl, indicate an average of around 30 clusters per event. This consistent average results from independently counting clusters every event for both PbSc and PbGl detectors.

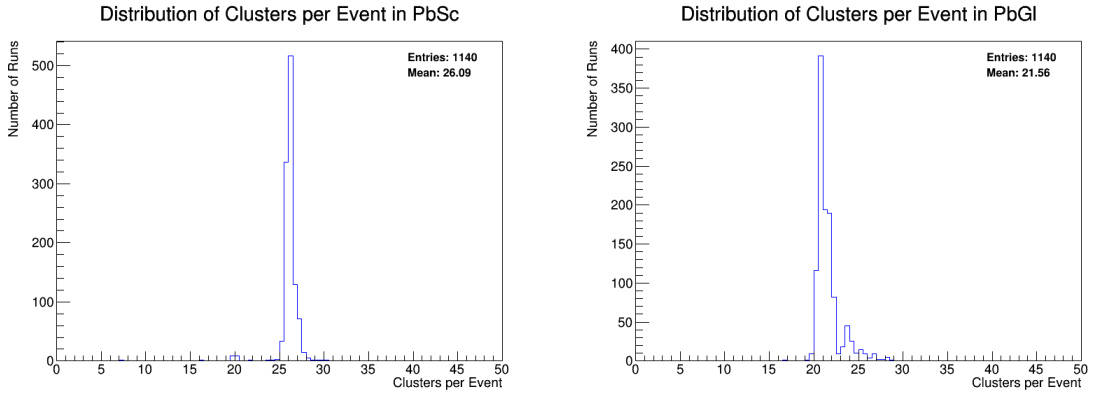

(a) Cluster distribution per event in PbSc **(b)** Cluster distribution per event in PbGl

Figure 3.2: Per-event cluster distributions for (a) PbSc and (b) PbGl detectors.

3.1.4 DHM Arrangement

This stage uses the `individualDHM.C` macro, which analyzes `preCheck.C` results to identify dead, hot, and extra hot towers. It then determines their operational status. See Section 3.2 for details.

1. The Hit Map, generated from the THMulf tower data, records hit frequencies in 2D histograms per iteration and segment. Figs. 3.3(a) show Raw Hit Maps for sectors 0, with tower rows and columns on the axes and hit counts vertically. Raw Hit Distributions Figs. 3.3(b) summarize hits per tower.

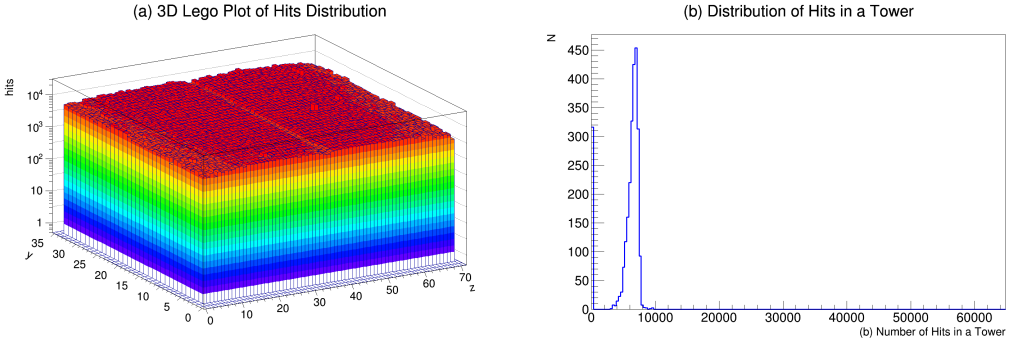

Figure 3.3: Raw Hit Map and Hit Distribution for sector 0, an energy range of 0.2-0.3 GeV, lowP=10.

2. The detector, although functional, is problematic. The cylindrical configuration interferes with the capture of complete photon cluster readouts along the beam direction (z), particularly at the edges, where the tower's coverage of solid angles decreases. We analyze the impact of pseudorapidity (η)—the angle between a particle and the beam axis—on hit counts. At $\eta = 0$, particles travel perpendicular to the beam; positive or negative η signifies angles relative to the beam. The effect of η on hits is seen in figure 3.4(a), which presents a linear viewpoint that emphasizes the detector's curved, non-projective geometry, leading to edge towers with diminished solid angles. Some towers exhibit abnormally high hits (red), but others indicate none (purple), often attributable to readout problems. The first phase entails the removal of extraneous hits and the reinstatement of cylindrical symmetry, as seen in Fig. 3.4(b).

3. Using the correction from Section 3.1.3, towers with misleading hits were removed to reveal the true η effect. We calculated the Mean and Standard Deviation (σ) of the Raw Hit Map, excluding towers beyond Mean + 10σ or below 1% of the Mean. The η normalization factor was obtained by projecting along the z-axis and normalizing by the mean. Figures 3.5(a) and (b) show the Raw Hit Map, corrected Hit Map, normalization factor, and η-corrected Hit Map for sectors 0 and 7. Although the η correction is theoretically valid, low-energy bins—particularly in PbGl—occasionally indicate excessive edge corrections.

   Despite η correction, many "defective" towers remain. To analyze hit distributions, data are divided into energy bins. Low energies show frequent hits per tower due to the steep energy spectrum, while high energies have few hits across sectors. Three distributions model the hits based on mean counts: Gaussian (> 50), Poisson (1–50), and Binomial (< 1). Appropriate fits are applied accordingly.

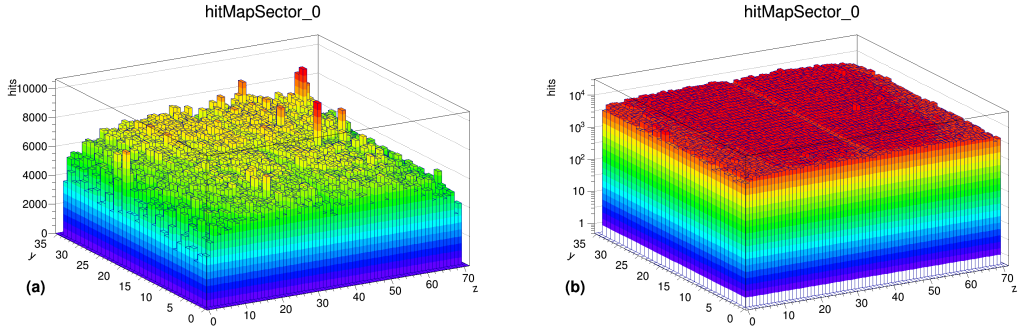

Figure 3.4: Sector 0 Raw Hit Maps: Linear and Logarithmic Scales (a) Linear scale Raw Hit Map showing sector 0 tower hit distribution. The x and y axes show each tower's location and color intensity reflects hits. (b) Logarithmic scale Raw Hit Map shows towers with lesser hit counts, clarifying sector 0 distribution. This scale helps detect tower malfunctions.The linear and logarithmic Raw Hit Map for sector 0 with energy 0.2-0.3 GeV.

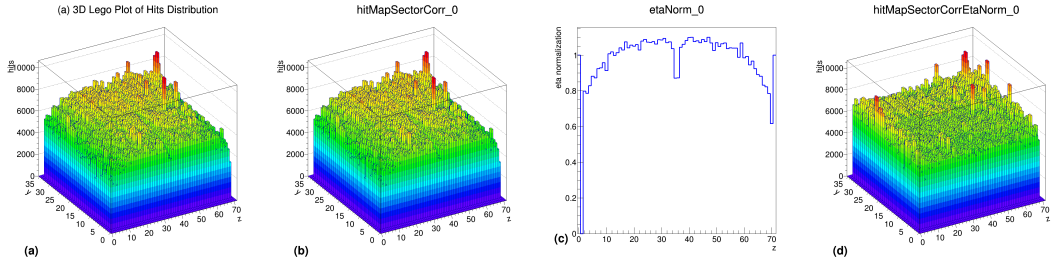

(a) Sector 0: Raw Hit Map, Corrected Hit Map, η normalization factor, and η-corrected Hit Map.

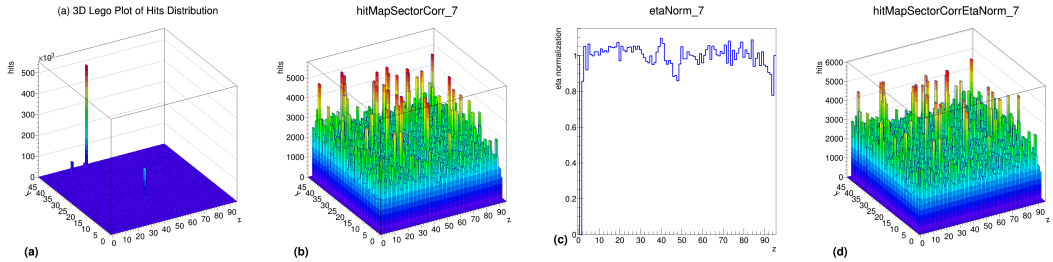

(b) Sector 7: Raw Hit Map, Corrected Hit Map, η normalization factor, and η-corrected Hit Map.

Figure 3.5: Hit maps and η corrections for sectors 0 and 7 with energy range 0.2–0.3 GeV and run number 408582.

4. Hit distributions are analyzed across energy ranges using three statistical models:

   - **Gaussian distribution** (low energies > 50): The fit defines dead thresholds at 10%, 20%, 30% of the mean and hot thresholds at mean plus 4, 5, and 6 standard deviations (Fig. 3.6(a)).
   - **Poisson distribution** (intermediate energies 1–50): Applied where hit counts are between 1 and 50, hot thresholds are set from the mean, no

dead thresholds are needed (Fig. 3.6(b)).

- **Binomial distribution** (high energies < 1): For low hit counts (< 1), a logarithmic scale and linear fit determine hot thresholds; no dead threshold is set (Fig. 3.6(c)).

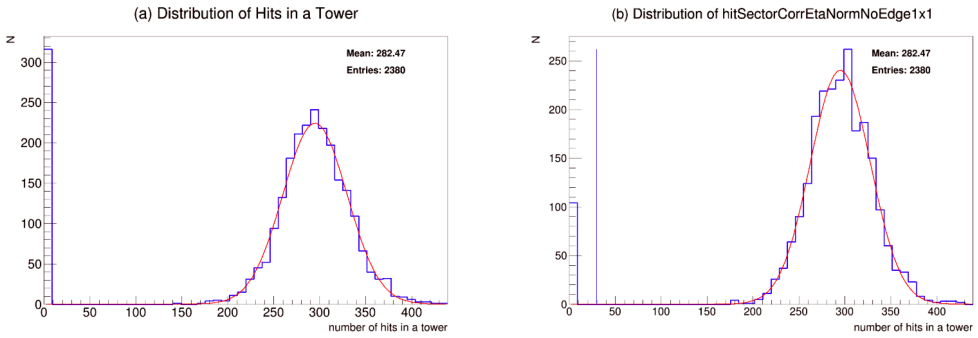

(a) Gaussian (low energy, 0.2-0.3 GeV)

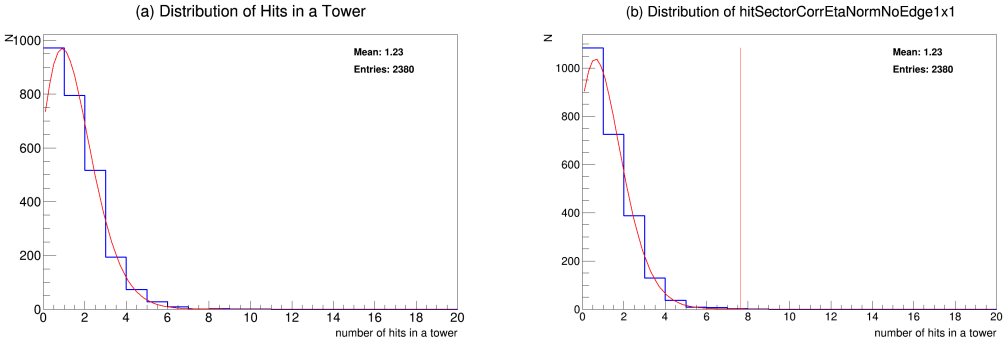

(b) Poisson (intermediate energy, 0.9-1.3 GeV)

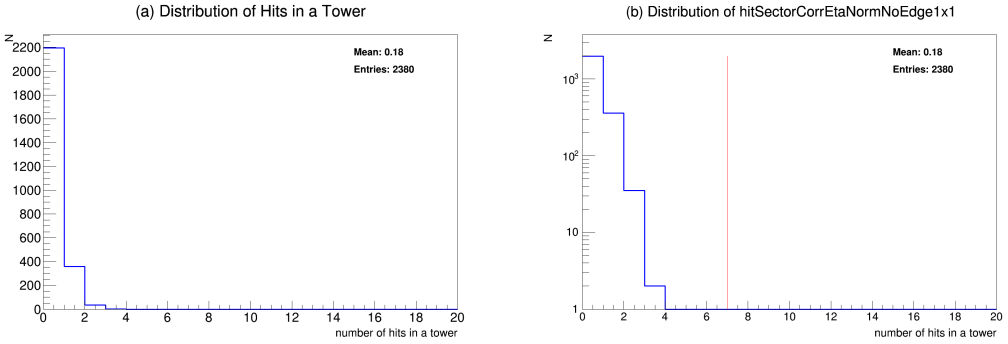

(c) Binomial (high energy, 0.9-1.4 GeV)

Figure 3.6: Raw and η-corrected hit distributions in sector 0 across energy ranges, modeled by Gaussian, Poisson, and Binomial fits. Dead and hot thresholds are marked.

3.1.5 Build a Fundamental DHM

The (dead, hot, extra hot) raw maps are generated by the `DHM.C` macro (Section 3.2), organizing data by energy bins across Run14. The main question is whether to exclude runs with many bad towers or mark towers as dead after repeated

poor performance, aiming to keep maximum data by monitoring tower status. DHM colors show tower status (Fig. 3.7)(Purple: Problematic in some runs, red: Malfunctioned in all runs, white: Always functional)

Runs fail if any sector has > 100 dead towers, < 20 clusters/event, or < 1 million events. DHM combined with GEANT3 adjusts for tower issues, keeping acceptance loss under 10%. Towers dead/hot in < 5% of runs (grass level) are still accepted for analysis.

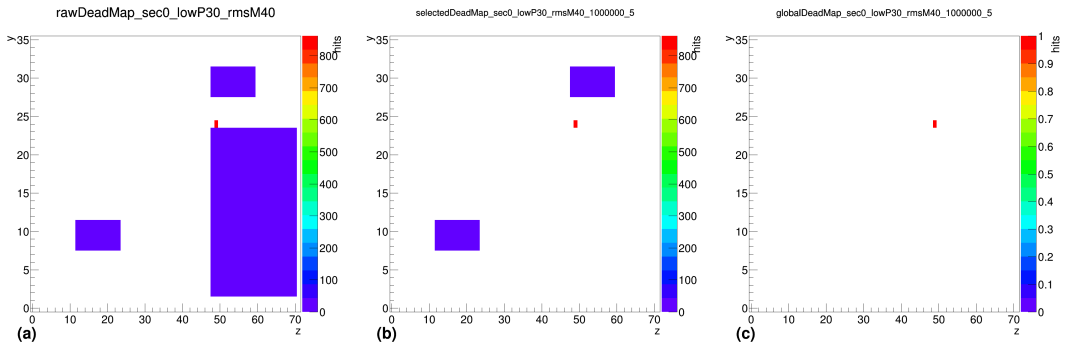

(a) Global Dead Map in Sector 0

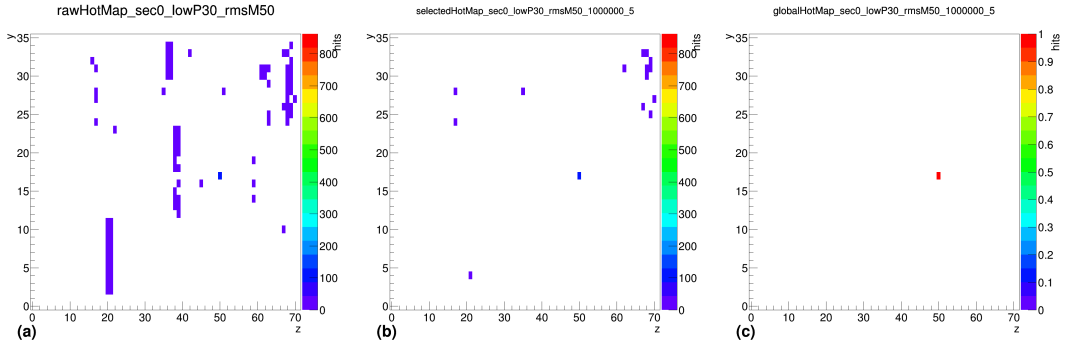

(b) Global Hot Map in Sector 0

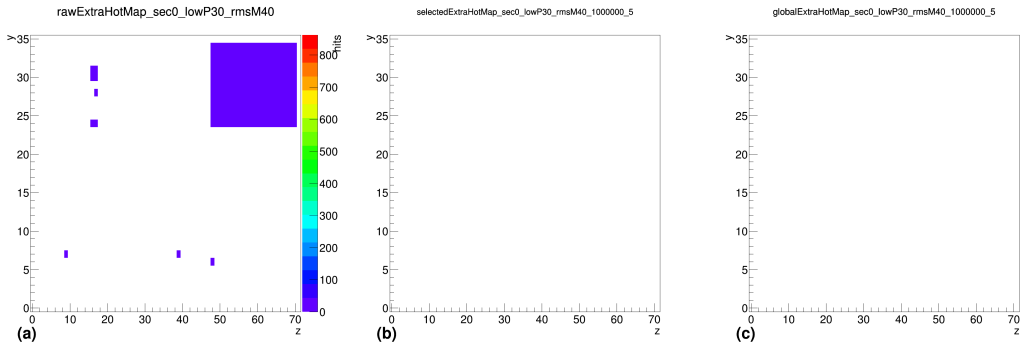

(c) Global Extra Hot Map in Sector 0

Figure 3.7: Combined maps from the Run14 dataset showing (a) Dead towers, (b) Hot towers, and (c) Extra Hot towers. Maps are created using raw, selected, and global data.

3.1.6 The DHMs generated at different energies

Using the `unionE.C` macro 3.2, we combine DHMs across all energy bins (0–39 GeV) for all QC-selected runs. Hot towers vary by sector; for example, in Fig. 3.8, most hot towers in sector 1 cluster at low energies (0–100 MeV), indicating acceptable errors within 100 MeV.

New parameters control tower status across energy bins: dead limit (lD = 0, 5, 10), hot limit (lH = 0, 1, 2, 5), extra hot limit (lEH = 0, none present), grass level (GL = 0–9), and minimum events (ME = 1,000,000). Runs with fewer than 1 million events were excluded to ensure statistical reliability.

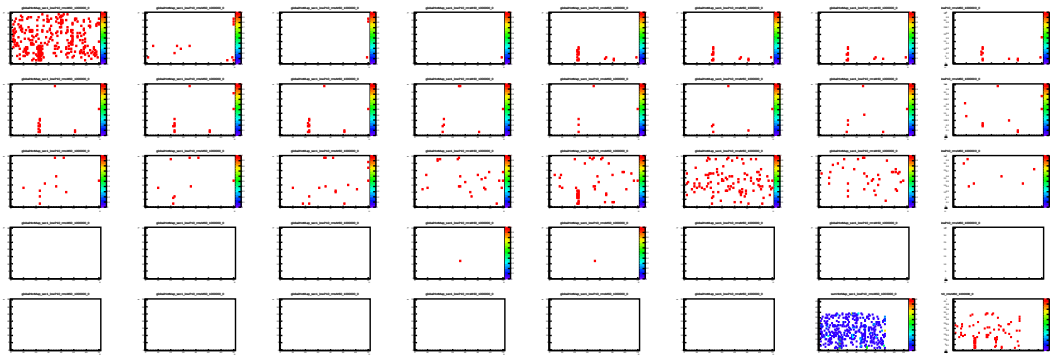

Figure 3.8: The Hot Map is generated for each energy bin individually and then combined at the end. In section 1, the parameters are as follows: lowP=0, rmsMσ=6, energy range (0-39), ME=1000000, Gl %=4, lD=0, lH=1, lEH=0.

3.1.7 The Grass Level Percentage

In order to determine the most effective parameters for the Cluster Energy Distribution, we examine how varying Grass Level Percent Numbers affect the final DHM. By recording the data points in a two-dimensional histogram, we generate Figure 3.9a, where the horizontal and vertical axes show Grass Level Percent ranging from 0% to 9%, and the height of each bar represents the corresponding fitted parameter values. In order to highlight the substantial difference between 0% and 1%, as well as the comparatively lesser changes between other percentages, we focus our attention on the range of 1.5% to 7.5% in Figure 3.9b. The optimal choice to run 14 AuAu is 5%, as it shows the minimal fluctuation between straight results. For more details, see the section 3.2.

3.1.8 Limiting the Dead and Hot Parameters

Upon choosing a GL of 5%, we proceeded to evaluate the limit dead (LD) and limit hot (LH) parameters. Modifications in LD are negligible (less than 0.01%), as shown in Figure 3.10a. Therefore, LD=0 can be employed. Regarding LH, we see a negligible effect (less than 1%) on the energy spectra, as shown in Figure 3.10b. Through performing LH analyzing with values of 0, 1, 2, and 5, we determined

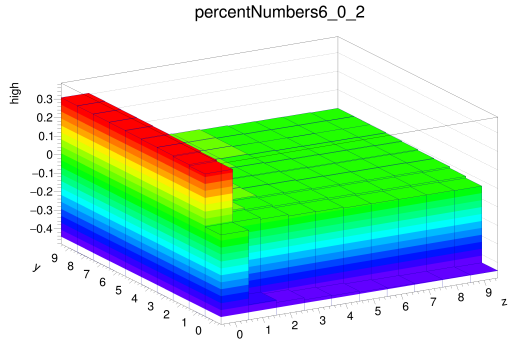

(a) The grass level in sector 6 varies from 0% to 9%. The z-axis represents the fitted values for the normalized difference of spectra.

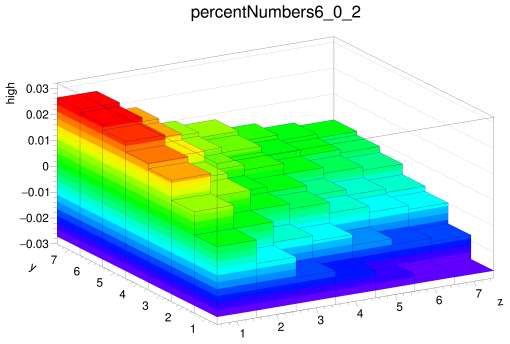

(b) The grass level fluctuates between 0% and 9% in sector 6 while zooming in at magnifications ranging from 1 to 7.

that these values corresponded to 0, 1, 2, and 3 on the y and z axes, respectively. Therefore, we choose LH=0 as the value for the final DHM.

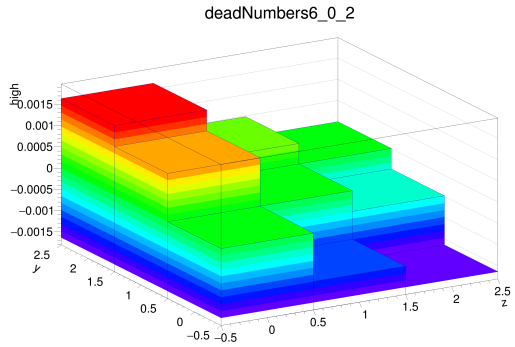

(a) Limit the Dead parameters Variations in sector 6 from 0 to 2.

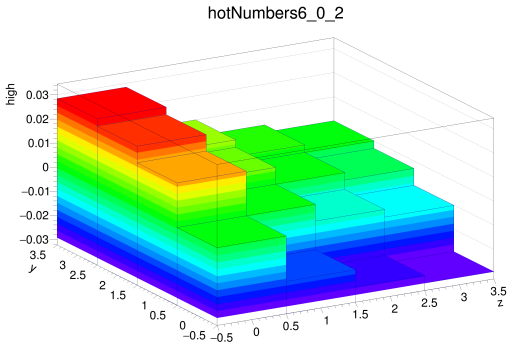

(b) Limiting the Hot parameters Changes in sector 6 between 0 and 2.

3.1.9 The Final DHM

As a result, what came next have been employed on the raw hit map (the colors represent the bad towers, the wite represent the good towers)(Fig.3.11 to identify the final DHM in Fig.3.12(the red color represent the dead, hot or extra hot towers, the wite represent the good towers).

- Exclude the short runs (less than 1 millionevents).
- Apply the quality cut procedure, excluding any run with an average cluster per event of less than 20.
- After the z-projection of the hit map normalization and pseudorapidity correction are applied.
- We have four types of towers: Normal, Dead, Hot, and Extra Hot, depending on the hit distributions. At low, medium, and high tower energies, fitting

the hit distribution yields binomial, Poisson, and Gaussian distributions, respectively. Hot towers are defined as those with hits exceeding (3, 4, 5, 6)σ above mean; dead towers are defined as those with hits below 10%, 20%, or 30% of mean.

- Then, we apply these limits to the union of the hit maps produced for various energy bins.
- The percentage of grass cut, which indicates that we only consider towers that were dead in less than 5% of all runs to be good towers.

Here is the final list of cuts/conditions to identify the final DHM in Fig.3.12:

1. PbSc 0.05, PbGl 0.3, low cluster per event
2. Each sector has a maximum of 100 dead towers.
3. 1 million events is the minimum number of events.
4. Dead condition(low p) is 10%. Hot condition is 6σ. Extra-hot condition is 100σ.
5. Grass level is 5%. The union's dead limit is 0, hot limit is 0, extra hot is 0.

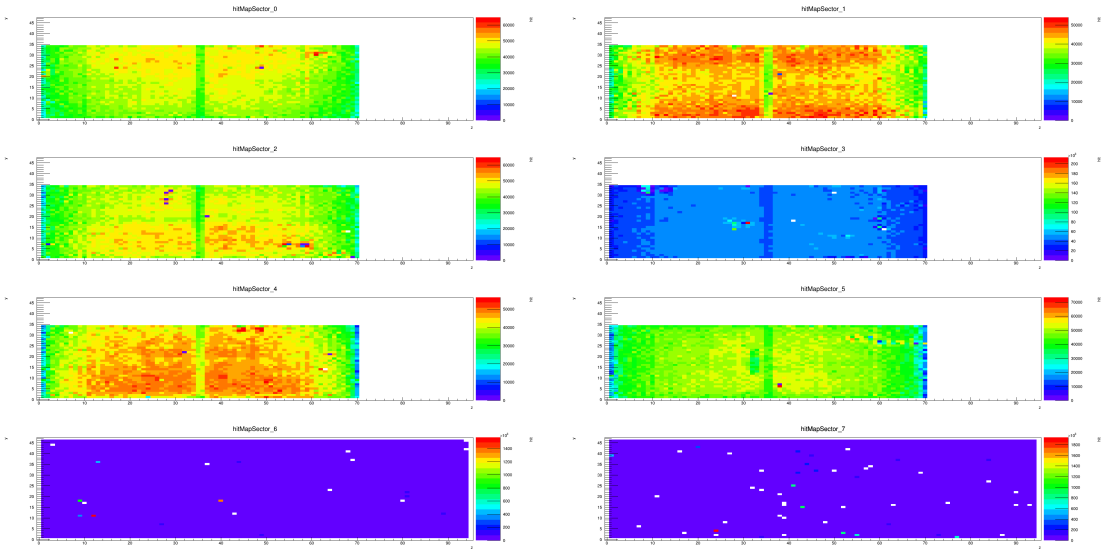

Figure 3.11: Raw hit map before applying our conditions.

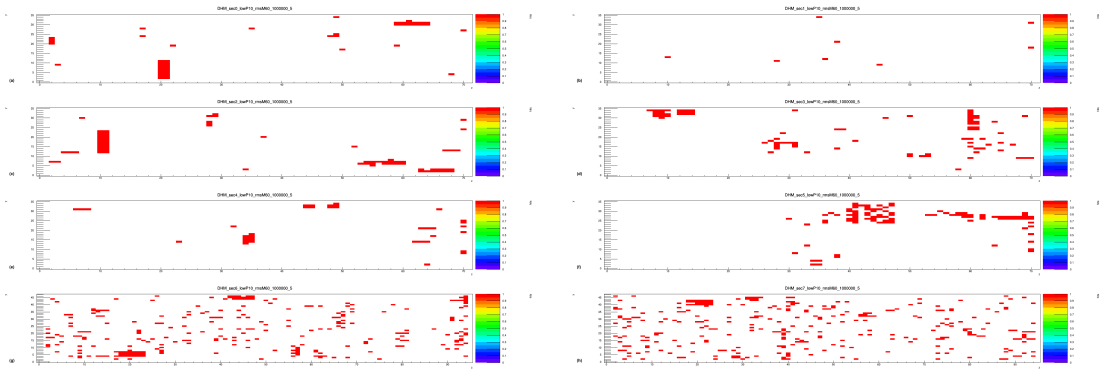

Figure 3.12: Final Dead Hot Map for each sector in *Au* + *Au* collisions (LD=0, LH=0, LEH=0, ME=1000000, GL%=5%).

3.2 Timing Calibration & Corrections

The goal of timing calibration in the PHENIX experiment is to convert the Time-to-Digital Converter (TDC) counts of towers in the electromagnetic calorimeter (EMCal) into the physical time of flight of particles, measured in nanoseconds. This process aligns the time measured from the actual collision, as indicated by the Beam-Beam Counters (BBC), relative to the collider's "beam clock," which runs every 110 ns. The BBC time marks the collision event, and the EMCal time marks the arrival of particles. To convert TDC counts to physical time, the procedure follows these steps (I have detailed our study's comparison with previous PHINEX research in my technical note [88]):

- Charged particles hitting the BBC start a counter until the next beam clock ("common stop" mode).
- A particle hitting the EMCal starts a counter until the next beam clock ("common stop").
- Both BBC and EMCal counts are converted into nanoseconds.
- Due to the "common stop" mode, earlier hits result in higher counts, which is corrected during conversion.
- The difference between EMCal time and collision time approximates the time of flight from the collision point to the EMCal.

In 3.13, A three-parameter model versus run number is used to fit timing data that is obtained at various energy interval. This model is not able to correct the arriving time of high-energy clusters.

A crucial correction to this timing is the *slewing correction*. PMTs in the Front-End Electronics (FEE) fire when the input signal crosses a threshold, causing larger signals to appear earlier. This effect, called slewing, must be corrected for accurate physical arrival times. Slewing correction uses photons, as they always travel at speed c.

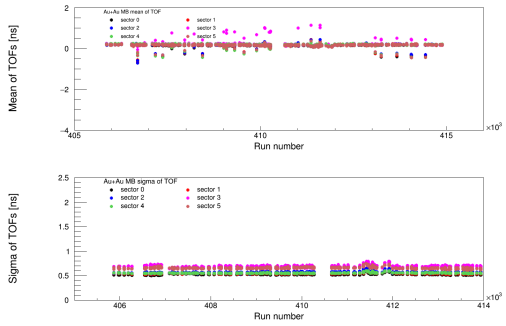

(a) MB trigger at 0-0.5 GeV

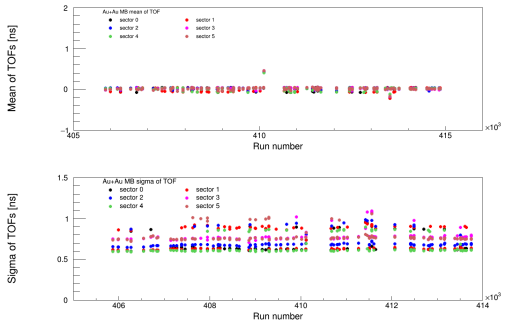

(b) MB trigger 0.5-1 GeV

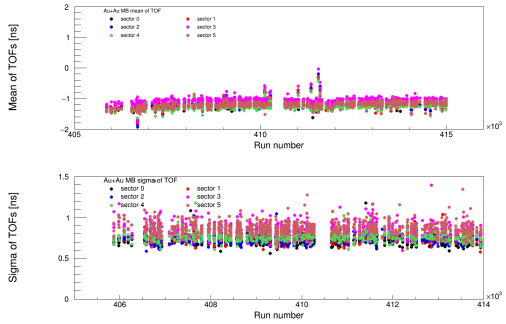

(c) MB trigger 2-3 GeV

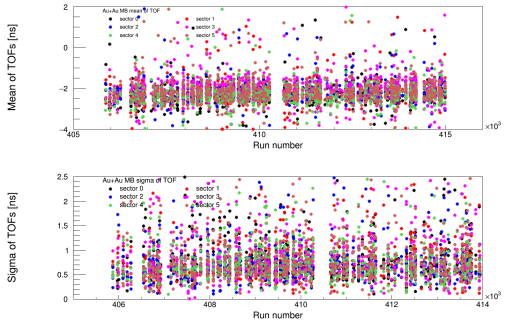

(d) MB Trigger 4-5 GeV

Figure 3.13: Arriving time using 3 parameter fit for the different runs and cluster energy interval

In addition to slewing correction, five other variables are considered for calibration:

$$\text{arrival time} = LC(4095 - TDC) - \text{walk} - t_0^{\text{offset}} - \text{sec}^{\text{offset}} - t^{\text{flash}}$$

where LC is a conversion factor from TDC counts to nanoseconds, $4095 - TDC$ accounts for the "common stop" mode, t_0^{offset} is the zero time offset of the BBC, $\text{sec}^{\text{offset}}$ is the sector-specific offset, and t^{flash} is the arrival time to EMCal, calculated as the distance from the vertex to the cluster's central tower divided by the speed of light.

For the walk correction, a three-parameter fit was previously used:

$$y = f(x; p_0, p_1, p_2) = \frac{p_0}{x^{p_1}} + p_2$$

This fitting approach, detailed in the Technical Note [90], was limited to ADC values from 0 to 2500. While this range covered lower energies well, it did not adequately address high-energy hits. To validate the fit, timing distributions for different run numbers and sectors were analyzed, applying sector-specific corrections alongside the three parameters from the fit.

Upon examination, it became evident that while the three-parameter fit adequately captured timing trends for low-energy clusters, it led to a systematic, negative shift in timing for higher energy hits (3.13, lower right lot for 4-5 GeV

clusters). In other words, the three-parameter fit fails to properly describe the asymptotic (high energy) behavior of slewing.

I have worked out a calibration method to solve it. From the Run14 MB data set 1% of the single clusters (KCluster) and the pairs (Combination) were saved into ntuples.

There were also saved all of the clusters with high p_T (p_T >5 GeV to fit the high p_T timing distributions for every tower.

3.2.1 Arrival Time Estimation Binning

Arrival time is computed as follows:

$$(4095 - \mathrm{TDC}) \cdot \mathrm{LC} - t_0^{\mathrm{BBC}} - t^{\mathrm{flashtime}} \tag{3.1}$$

In the subsequent plots, one tower example per sector is shown. Initially, a broad range for arrival time is used to identify deviations from the expected arrival time, even at 300 ns. The time when the timing threshold is crossed depends on the total PMT signal, causing arrival times to increase with lower ADC values. We utilized the scripts `estimateBinning.C` and `estimateBinning.sh`, discussed in Section 3.3.

Arrival time is a broad range calculation that emphasizes the need for timing adjustments by highlighting values that deviate from expectations. Arrival times are dependent on ADC values; lower ADC values are correlated with higher arrival times.

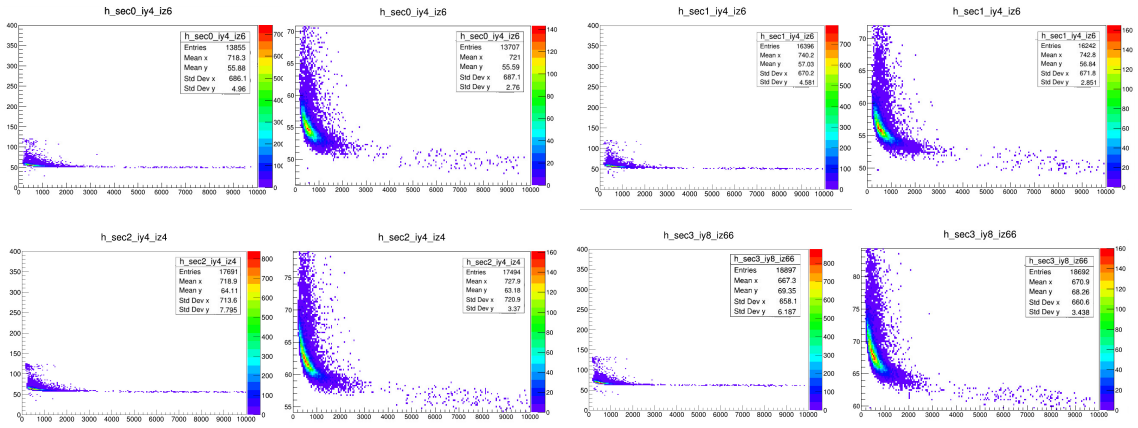

Figure 3.14: Rows 1–4: Sectors 0, 1, 2, and 3, each with wide range (left) and zoomed-in (right) panels.

For the leftmost data points, successful fitting becomes difficult by non-normal distributions in the cases shown in Figures 3.16, 3.17. One problem is finding an appropriate fit for the leftmost data points. The histogram's mean y value is used as input for the rebinning, we utilize a method predicated on the mean y value of the histogram. The script rebin.C is adapted to rebin and refill the histogram from the ntuple data. The normal range for rebinning typically covers mean y ±10 to ±15 ns respectively. Broader ranges, like -25 to +55 ns, are necessary for some

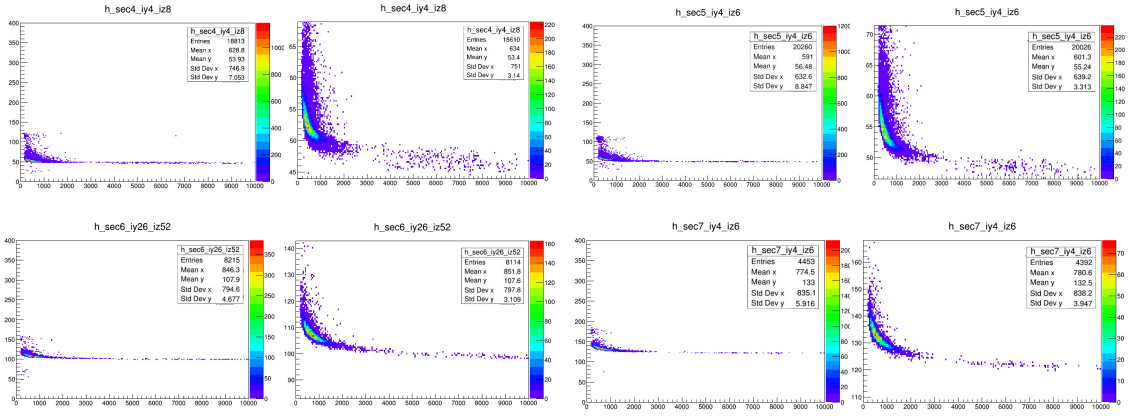

Figure 3.15: Rows 1–4: Sectors 4, 5, 6, and 7, each showing wide range (left) and zoomed-in (right) panels.

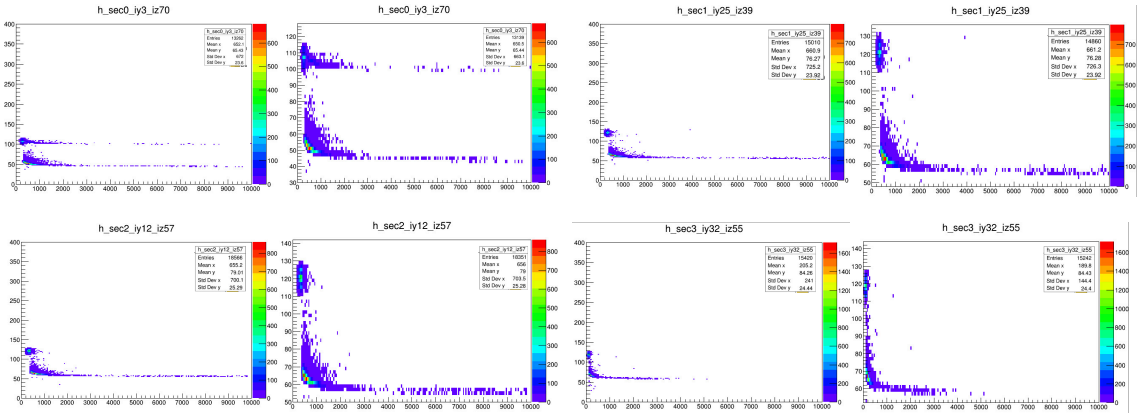

Figure 3.16: Four rows showing Sectors 0 to 3, each with wide range (left) and zoomed-in (right) panels.

towers, as this range proved to be insufficient. The preRebin.C and preRebin.sh macros are specifically designed to identify towers that need alternate binning (See 3.3).

3.2.2 Three Factors Fitting, First Fit for Sector Offset Correction

In Section 3.3, we utilize a three-parameter fitting model in the `fit.C` code:

$$y = f(x; p_0, p_1, p_2) = \frac{[0]}{x^{[1]}} + [2] \tag{3.2}$$

Direct fitting in ROOT is difficult for a 2D histograms, which include 200 bins along the raw ADC axis and 100 bins along the arrival time axis. We slice the 2D histograms along the y-axis saved it in a temporary histogram and calculate its mean and sigma, these describes this tower arrival time at the specified raw ADC.

A new TGraphError is created using these extracted values (mean and sigma), and it is displayed in tn the 2nd and 4th colums in 3.18, 3.19. We can extract and save the three parameters for every towers by fitting this histogram.

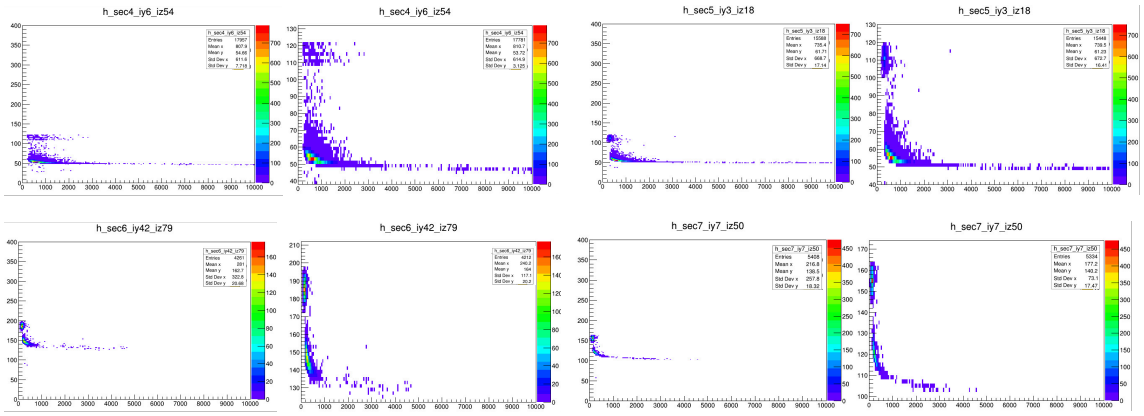

Figure 3.17: Four rows of panels: each row shows Sector 4 to 7 with a wide range (left) and zoomed-in view (right).

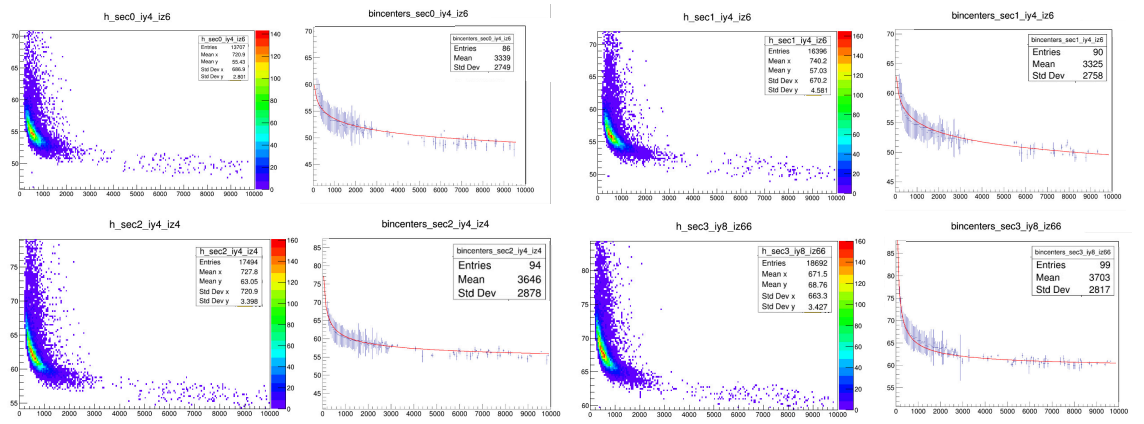

Figure 3.18: Correction of arrival time vs. raw ADC histograms for sectors 0–3. Left: 2D histograms (200 ADC bins × 100 arrival time bins). Right: fitted 1D histograms with extracted parameters.

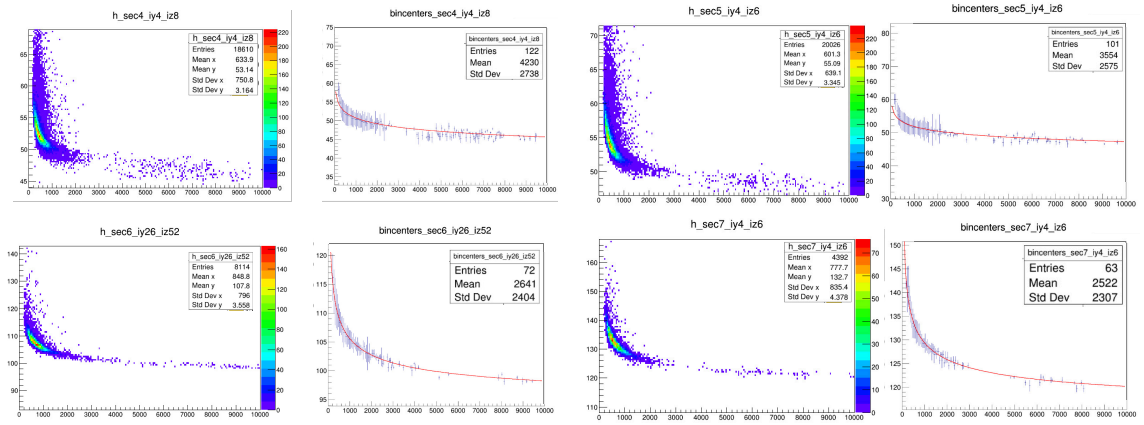

Figure 3.19: Sector-by-sector (4–7) correction of arrival time versus raw ADC histograms. Left: 2D histograms with 200 ADC bins and 100 arrival time bins. Right: fitted 1D histograms extracting three key parameters.

3.2.3 Tower Sector-Run Offset

Individual towers can take offsets from run to run at the level of a sector. By correcting the arrival time with the simple three parameters fit (describes the timing correctly for the dominant low energy hits of the tower), the corrected arriving time for all of the towers in the given sector can be seen in Figure: 3.20, 3.21 the means for all sector and runs are shown in Figure: 3.22

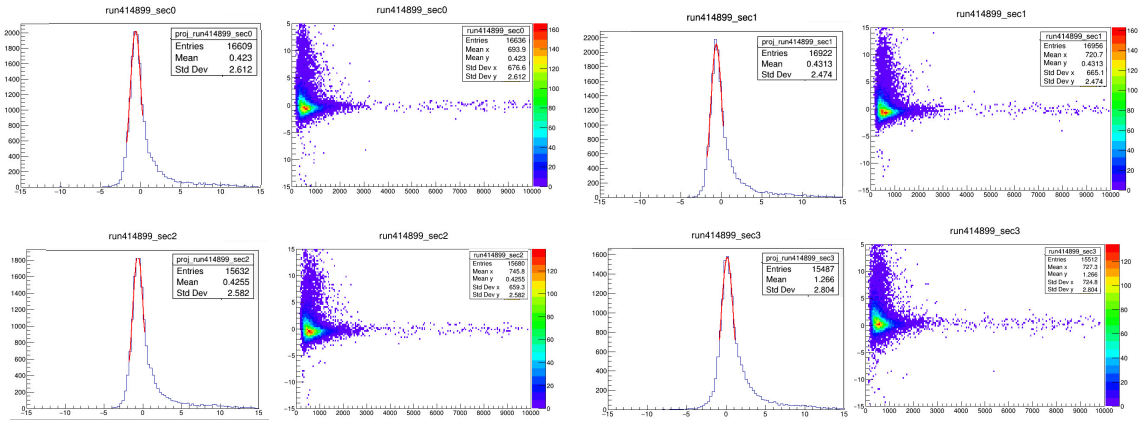

Figure 3.20: Corrected tof vs. ADC and Gaussian projection (Sectors 0–3).

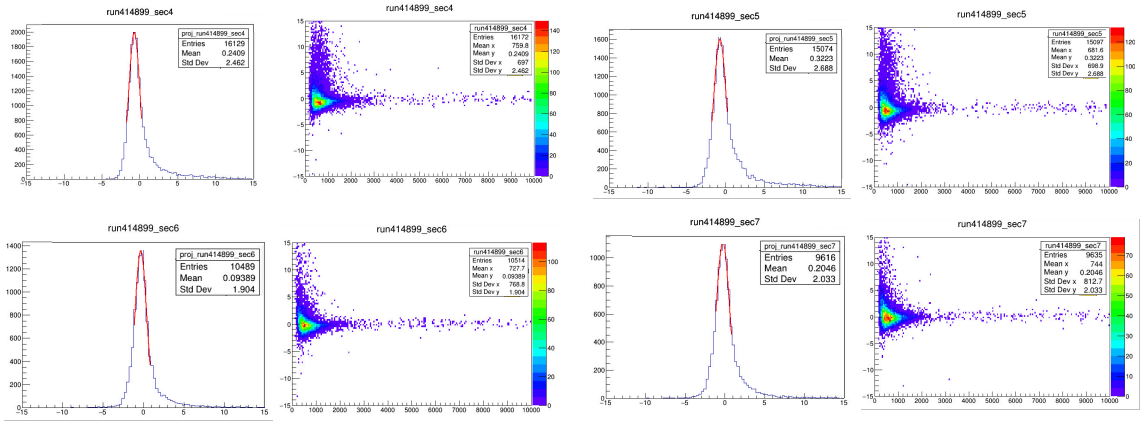

Figure 3.21: Corrected ToF vs. ADC and Gaussian projection (Sectors 5–7).

It is significant to note that each run within a given sector may have a different mean value, which represents a collective offset unique to that run and sector. Tower timing must be adjusted by subtracting this amount. This procedure is fully implemented in the secbysec.C code (see 3.3).

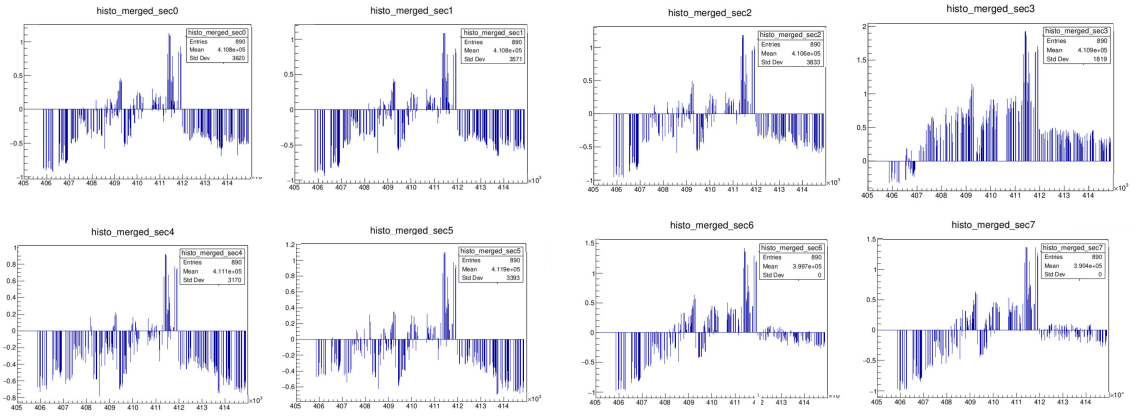

Figure 3.22: Sector offsets vs. run number.

3.2.4 Applying A Second Re-binning

The calculation of the arrival time is improved using sector-by-sector and run-by-run offsets. The equation is represented as follows:

$$arrivaltime = LC \cdot (4095 - TDC) - walk - t_0^{offset} - sec^{offset} - t^{flashtime} \quad (3.3)$$

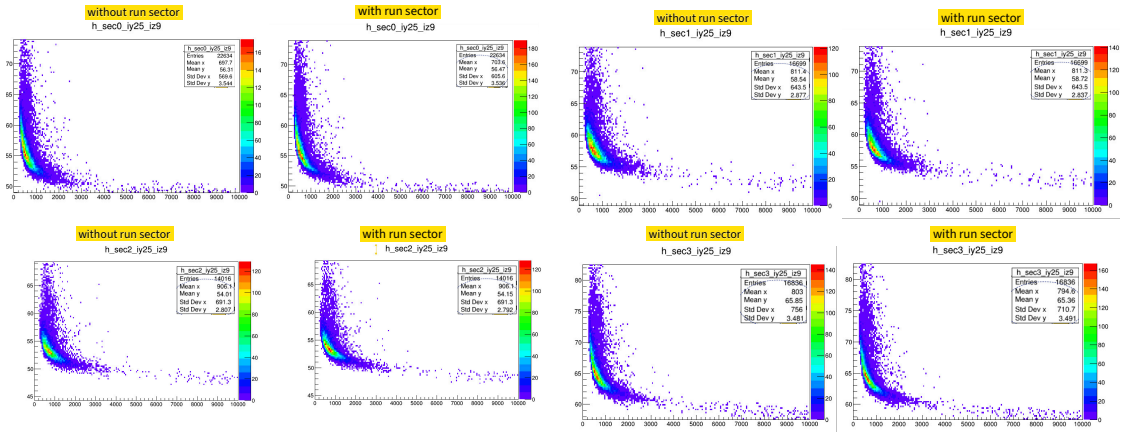

Figure 3.23: ToF-ADC before and after sec-by-sec correction for a tower for each sector(0, 1, 2, 3)

Figures: 3.23, 3.24 show the process of correction, in which the time is modified by applying the determined offset value, the meanY changes shows the impact of the correction. The code "rebinwithrunsec.C" (refer to Code 3.3) was used for this purpose.

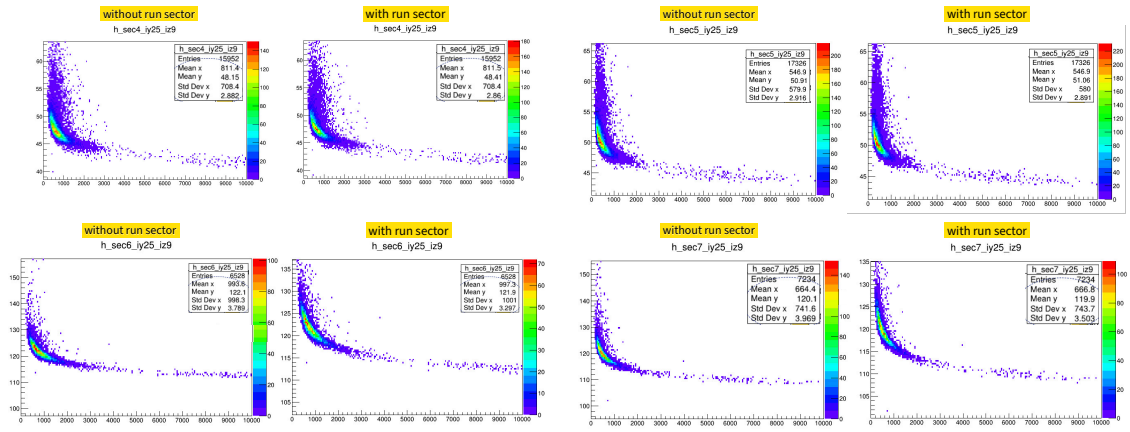

Figure 3.24: ToF-ADC before and after sec-by-sec correction for a tower for each sector(4, 5, 6, 7)

3.2.5 Refitting Following Sector-by-Sector Correction

On the 2D histogram, corrected with secor-run offset, we perform a five-parameter fitting process using the fitwithrunsec.C code (Check 3.3). First, we fit a constant to the interval where rawADC > 4500, the saturation part of the arriving time. Next, we fit a three-parameter function to the interval where rawADC < 1500, the typical low energy fit. Lastly, we used a five-parameter method to fit the full histogram. = $\frac{[0]}{x^{[1]}} + [2] + \frac{[3]}{x^{[4]}}$ We use parameters from the second fit as starting parameters and the constant fit result from the first fit as a fixed parameter for the final fit. Although fitting with five free parameters is not always easy, using fixed or dependable beginning values almost always results in good fits, as Figures 3.25, 3.26 illustrates.

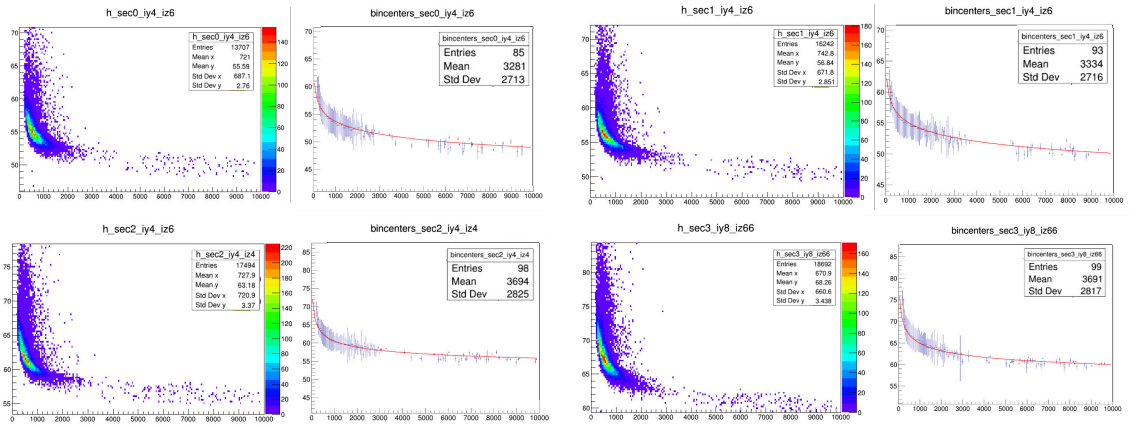

Figure 3.25: Five parameters fit in sec 0, 1, 2, 3 after sector-run corrections.

3.2.6 Photon Pair Timing Distribution

Precise timing information from the EMCal is essential for proper event identification and the elimination of overlapping events. We are primarily concerned with analyzing the temporal distribution of photon pairs. As an illustration, we

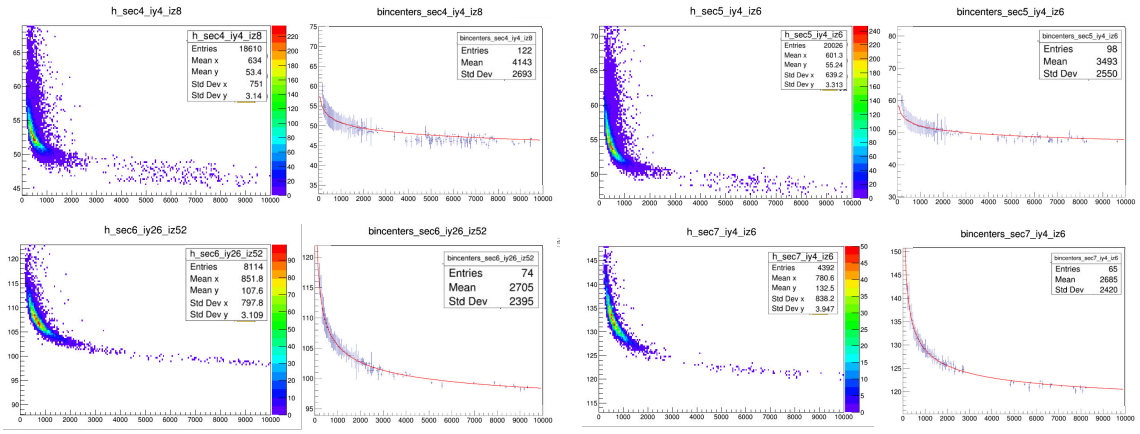

Figure 3.26: Five parameters fit in sec 4, 5, 6, 7 after sector-run correction.

graphed the adjusted Time-of-Flight (ToF) of pairs of clusters within ToF boundaries of -100 ns and +100 ns. In Figure: 3.27, the clusters are primarily concentrated around $0ns$, suggesting successful adjustments. However, there are several clearly identifiable zones, one reaching its maximum at roughly +60 ns and the other at around -20 ns. These variations justify a more thorough analysis of the association between the groups in these places. These entries are presumably the result of two collisions occurring in the same bunch-crossing, or collisions in the peripheral regions of the bunches known as "satellite peaks". It is important to acknowledge that, although clearly visible on a logarithmic scale, the quantity of these collisions represents less than one percent of the entire number.

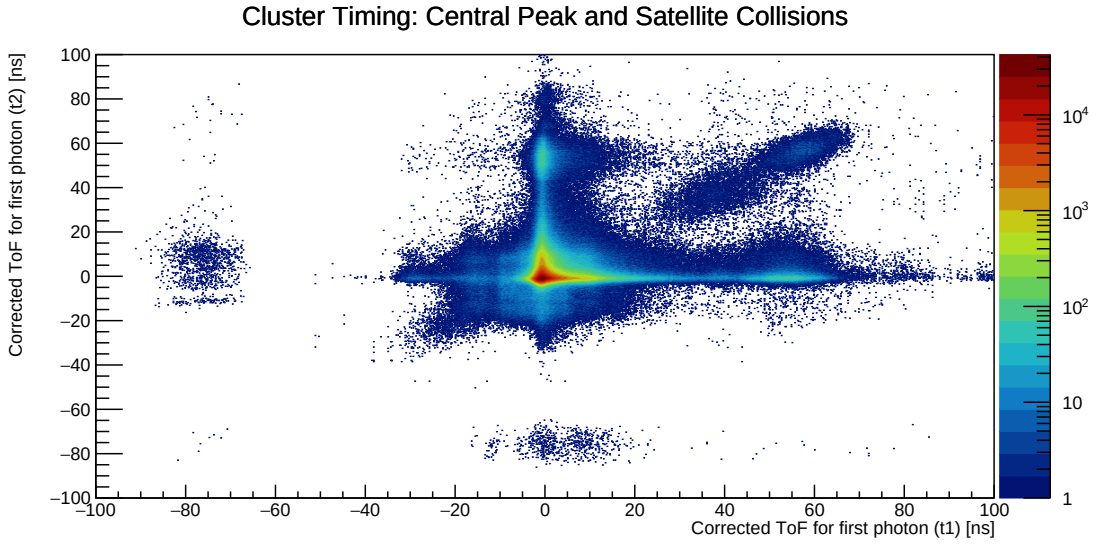

Figure 3.27: Cluster timing deviations are concentrated about 0 ns, with small increases between +60 ns and -20 ns, potentially related to multiple collisions or satellite peaks. These are fewer than 1% of the total events.

3.2.7 Five-parameter Mean & Sigma

We applied five parameters fit for slewing, as previously described, to enhance our analysis and provide new versions of the plot 3.13 for both MB and ERT. The slewing parameters are obtained from the MB (1% of all, and every cluster $p_T > 5$ GeV), but are also valid for the ERT. The objective of this strategy was to enhance the precision of the timing for high energy events, therefore providing a more accurate calibration of our data (as shown in the figures below (3.28), the mean are always around 0, no offsets at higher energy:

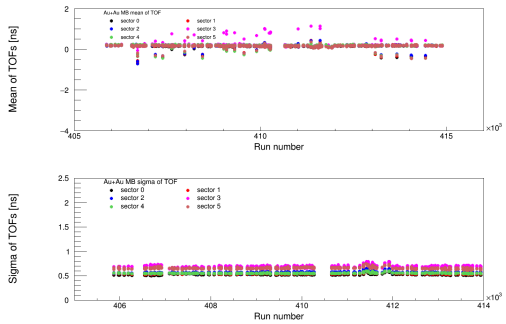

(a) MB Trigger 0-0.5 GeV

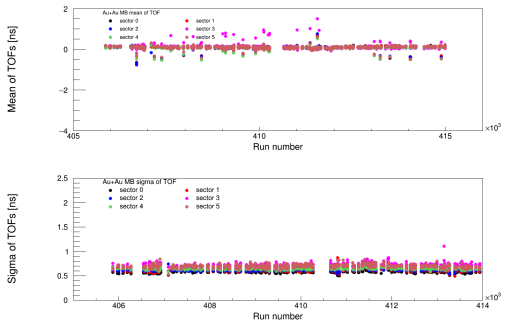

(b) ERT Trigger at 0-0.5 GeV

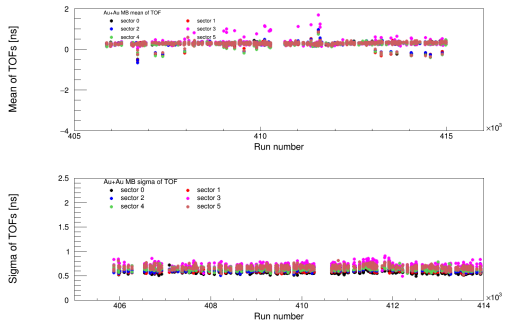

(c) MB Trigger at 2-3 GeV

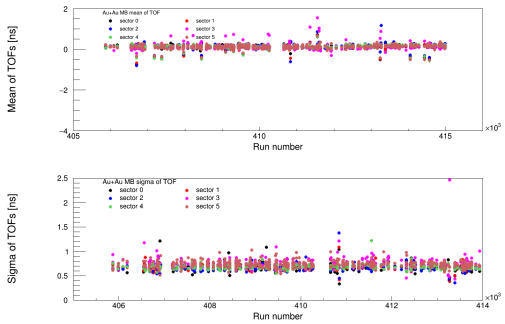

(d) ERT Trigger at 2-3 GeV

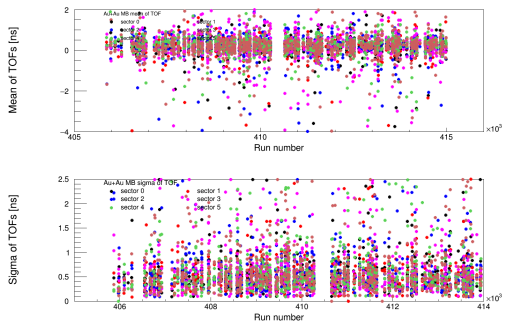

(e) MB Trigger at 5-6 GeV

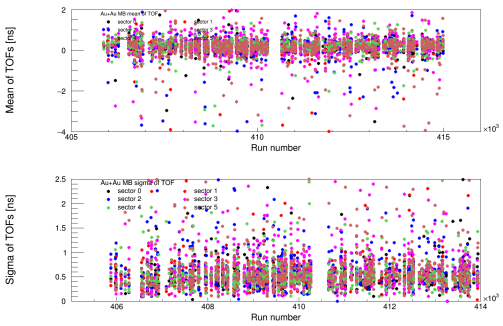

(f) ERT Trigger at 5-6 GeV

Figure 3.28: Mean and sigma values calculated for MB_Trigger (left panels) and ERT_Trigger (right panels) at different energy thresholds.

CHAPTER 4

ANALYSIS OF π^0S & DIRECT γ PRODUCTION

4.1 Introduction

This chapter provides a thorough examination of direct photons and raw π^0s seen in heavy ion collisions at PHENIX. It begins by outlining the fundamental steps of the extraction and the simulation and data processing, including detector acceptance, efficiency corrections, and the unfolding procedures applied to extract the true physical yields from the measured data.

The chapter details the derivation of the observed invariant yields for direct photons and π^0 process. Systematic uncertainties related to each measurement are carefully examined and analyzed to clarify the precision and limitations of the results.

A thorough comparison is conducted between the unfolded invariant yields and previously published data, emphasizing both consistency and reported errors. This validation phase enhances the dependability of the present study and explains it within the larger framework of heavy ion collision physics.

4.2 π^0 Extraction and Background Subtraction

In the EMCal, we primarily observe photons from the decay $\pi^0 \rightarrow \gamma\gamma$. The invariant mass of these decay photons is calculated as:

$$M_{\gamma\gamma} = \sqrt{2E_1E_2(1 - \cos\varphi)}$$

where E_1 and E_2 are the photon energies, and φ is the opening angle between them. We analyze data from the Minimum Bias and ERT trigger using advanced background subtraction techniques for the extraction of π^0 (using the Pi0Extraction Example.C code 3.4).

4.2.1 Mixed Background Subtraction

For low transverse momentum (p_T), we use mixed event techniques (4.1):

1. **Event Pairing**: Photon pairs from lead scintillator (PbSc) and lead glass (PbGl) were reconstructed within the same sector to calculate the invariant mass and transverse momentum.

2. **Mixed Event Generation**: Combine photons from different events to create a combinatorial background. Normalize this background to fit the real event background.

3. **Residual Background Fit**: Subtract the mixed event background from the real data and fit any residuals with a 2nd order polynomial to isolate the π^0 peak.

4.2.2 Average Count Subtraction

For high p_T, where mixed event statistics are sparse (4.1):

1. **Background Estimation**: Estimate the combinatorial background using the average bin content outside the π^0 peak in the real distribution.

2. **Peak Extraction**: Subtract the estimated background to isolate the π^0 peak.

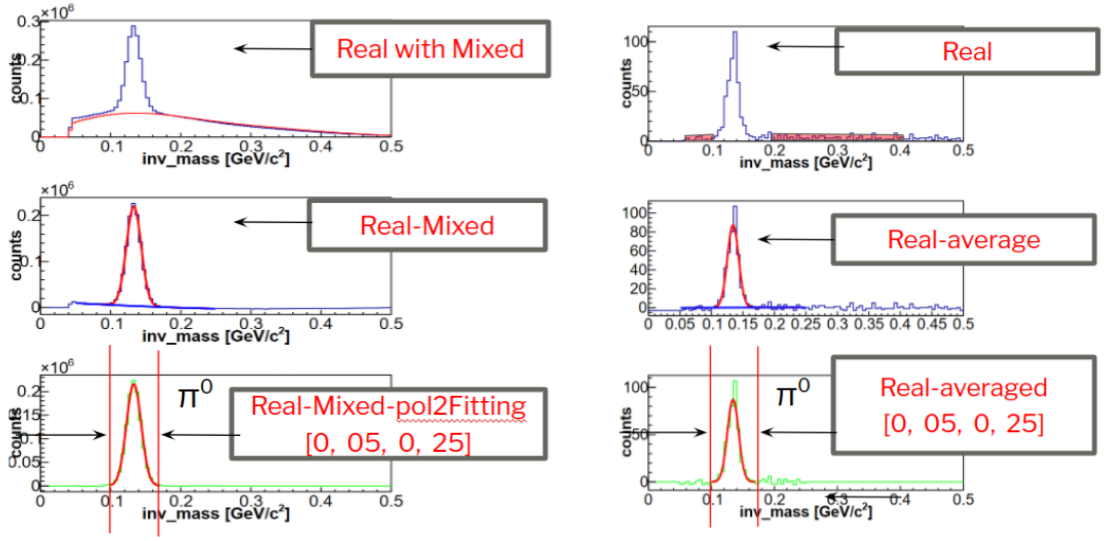

Figure 4.1: π^0 background subtraction: Left panels show the mixed event background method, right panels the average background method. The first row presents the real and scaled mixed event invariant mass. The second row displays peak extraction with mixed events, and the third row shows residual background subtraction using a second-order polynomial fit.

This methodology improves π^0 peak extraction by integrating mixed background subtraction. These improvements lead to more accurate and reliable results across different p_T ranges.

4.2.3 Extracting π^0 Under Various Conditions

To analyze π^0 production, we consider various standards:

- **Centrality Classes:** To characterize the collision geometry and study its effect on photon and pion production. These centrality bins correspond to fractions of the total inelastic cross section, ranging from the most central (0%-5%) collisions, representing the highest overlap and particle multiplicity, to peripheral collisions (90%-100%). Additionally, a minimum bias (MB) category encompasses all centralities for an inclusive measurement. The specific bins used are:

  CC=0: 0-5%, CC=1: 5-10%, CC=2: 10-15%, CC=3: 15-20%,
  CC=4: 20-25%, CC=5: 25-30%, CC=6: 30-40%, CC=7: 40-50%,
  CC=8: 50-60%, CC=9: 60-70%, CC=10: 70-80%, CC=11: 80-100%,
  CC=MB: 0-100%.

  Specific cuts are applied to the particle showers for each centrality range and trigger to enhance the purity of the photon sample:

- χ^2 **Cut:** The identification of particles is refined using the shape of the shower, described by:

$$\chi^2 = \sum_i \frac{(E_i^{\text{meas}} - E_i^{\text{pred}})^2}{\sigma_i^2},$$

  where E_i^{pred} is the predicted energy deposit in the i- tower, E_i^{meas} is the measured energy deposit, and σ_i represents the predicted energy fluctuation of electromagnetic showers. This is calculated using parameters from extensive test beam data. We apply a χ^2 cut of $< 2.0, 3.0, 4.0$.

  PID0 cut:
  PID0 is $\chi^2 < 2.0$ is the strictest cut, aiming at maximum signal purity at the expense of efficiency loss.

  PID1 cut:
  PID1 is $\chi^2 < 3.0$, it is a looser cut compared to PID0. It rejects hadrons while retaining most of the true photon signal, balancing efficiency and purity.

  PID2 cut:
  PID2 is $\chi^2 < 4.0$, it is the loosest cut, aimed at maximizing the signal at the expense of purity.

- **Timing Cut:** To minimize hadron contamination, we use a time of flight (ToF) cut for the showers, set at $< 5ns$ for each sector. This cut also helps remove particles from overlapping events.

- **Asymmetry Cut:** For π^0 extraction, only decay photons that meet the energy asymmetry criterion are included in the analysis:

$$\left|\frac{E_1 - E_2}{E_1 + E_2}\right| < 0.7, 0.8, 0.9$$

Here, E_1 and E_2 are the energy of the two decay photons.

ASYM0 cut:
Asymmetry limit = 0.7 is the strictest cut, minimizing the effect of low energy ("noise") clusters.

ASYM1 cut:
Asymmetry limit = 0.8, it is a moderate cut, tightening the range of allowed asymmetry values to reduce the background and improve the purity of the π^0 sample.

ASYM2 cut:
Asymmetry limit = 0.9 is the loosest cut, which makes the sample quite contaminated at low transverse momenta; on the other hand, it enhances the number of reconstructed π^0 at high p_T where low-asymmetry cluster pairs are already merged.

4.2.4 MB Trigger Application

- Three different energy asymmetry cuts:
  Asym=0: Asymmetry limit = 0.7 (see Fig. 4.2), **Asym=1**: Asymmetry limit = 0.8 (See Fig. 4.3), **Asym=2**: Asymmetry limit = 0.9 (See Fig. 4.4).

- Three differing PID conditions were set up:
  PID=0: χ^2 limit = 2.0, **PID=1**: χ^2 limit = 3.0, **PID=2**: χ^2 limit = 4.0.

- Two unique Time-Of-Flight (TOF) settings were applied:
  TofCut=0: No TOF cut (See Fig.4.2), **TofCut=1**: 5 ns cut (See Fig. 4.5).

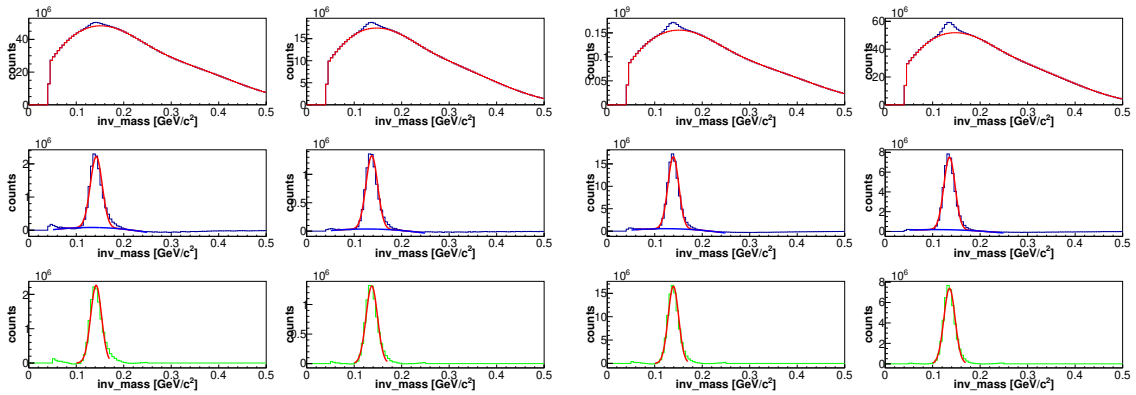

Figure 4.2: The mixed event background, 1.5-2.0 GeV/c Pt: left panels 0-5% cc, while right panels 0-92% cc. All have tof=0, PID=0, asym=0, MB trigger. PbSc (1st, 3rd), PbGl (2nd, 4th). Real and scaled mixed invariant mass; peak extraction; residual background subtraction by 2nd-order polynomial fit.

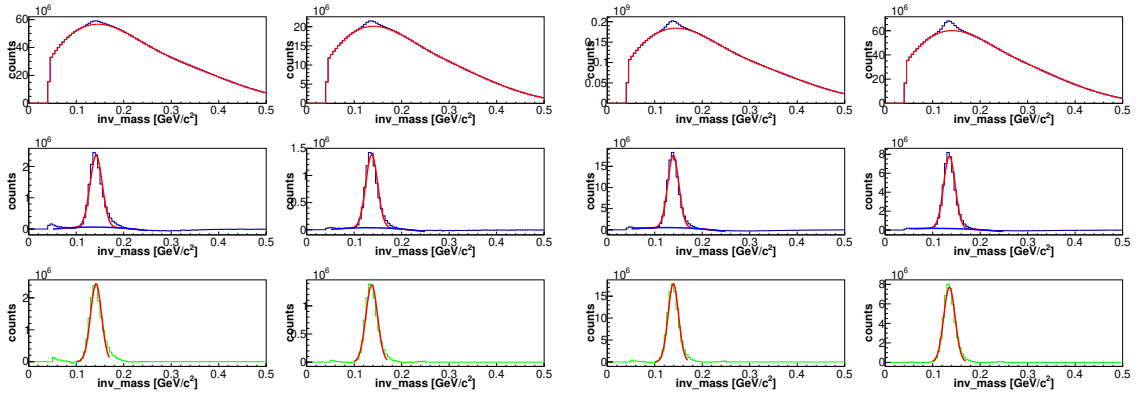

Figure 4.3: Same procedure as Fig.4.2 with asym=1.

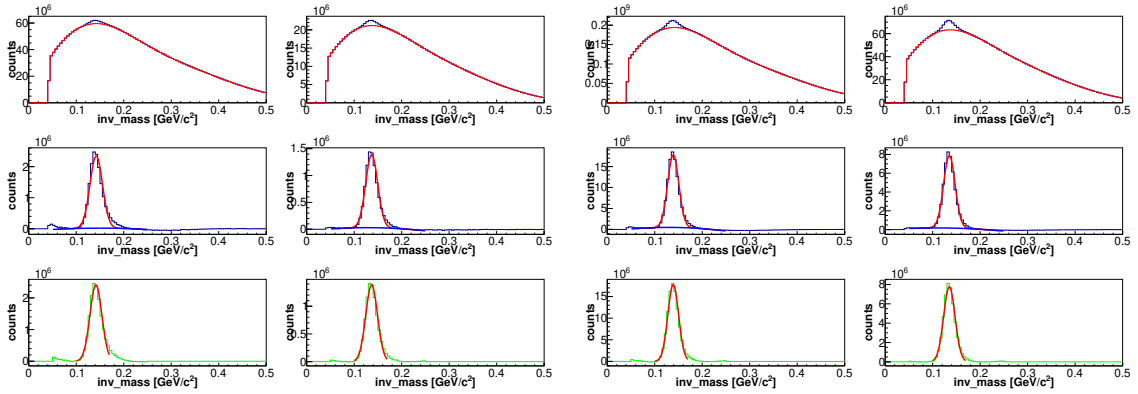

Figure 4.4: Same procedure as Fig.4.2 with asym=2.

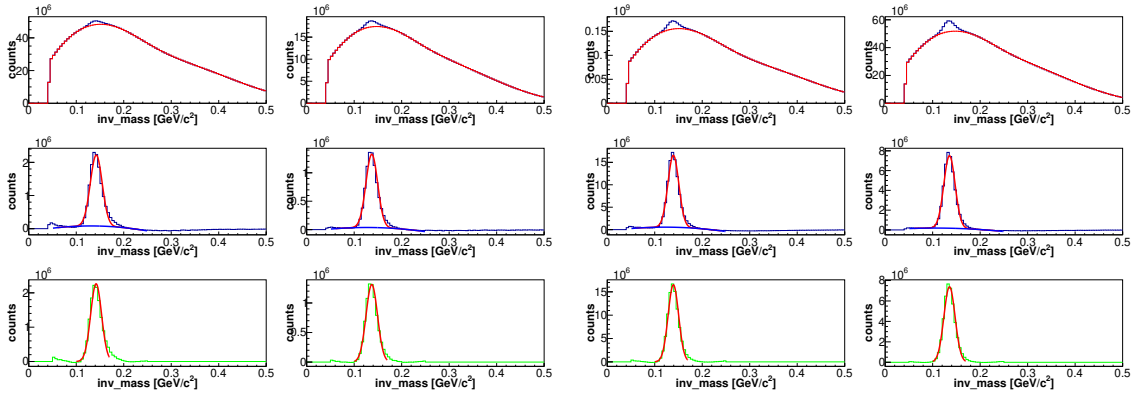

Figure 4.5: Same procedure as Fig.4.2 with TOF=1.

4.2.5 ERT Trigger Application

- There are three separate energy asymmetry cuts:
  Asym=0: Asymmetry limit = 0.7 (see Fig. 4.6), **Asym=1**: Asymmetry limit = 0.8 (see Fig. 4.7), **Asym=2**: Asymmetry limit = 0.9 (see Fig. 4.8).

- Three differing PID conditions were set up:
  PID=0: χ^2 limit = 2.0 (See Fig.4.6), **PID=1**: χ^2 limit = 3.0 (see Fig. 4.9), **PID=2**:

χ^2 limit = 4.0 (see Fig. 4.10).

- Two separate time-of-flight (TOF) settings were tested:
  TofCut=0: No TOF cut (see Fig.4.6), **TofCut=1**: 5 ns cut (see Fig.4.11).

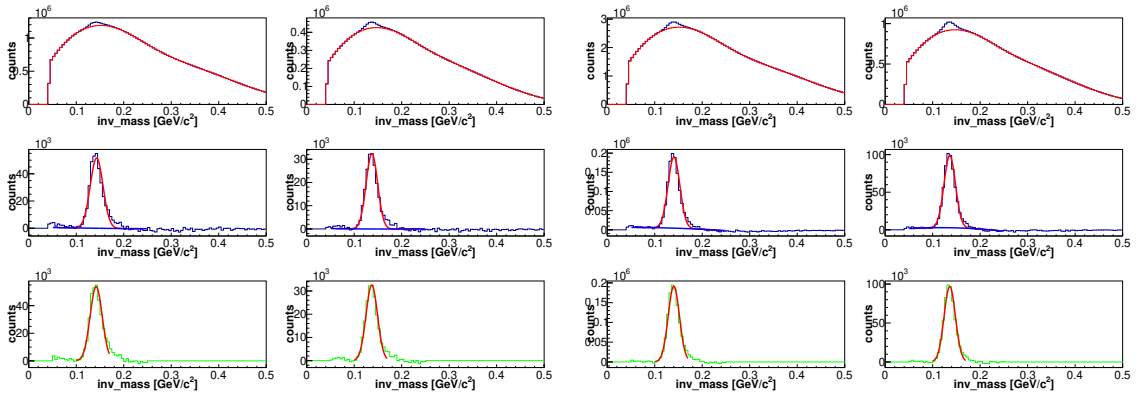

Figure 4.6: Mixed background elimination: 6-panel canvas showing pT=1.5–2.0 GeV/c for 0–5% centrality (left) and 0–92% MB (right) with tof=0, PID=0, asym=0 (ERT). Columns: PbSc (1st, 3rd), PbGl (2nd, 4th). Rows: real and scaled mixed invariant mass, peak extraction, and residual background subtraction via 2nd-order polynomial fit.

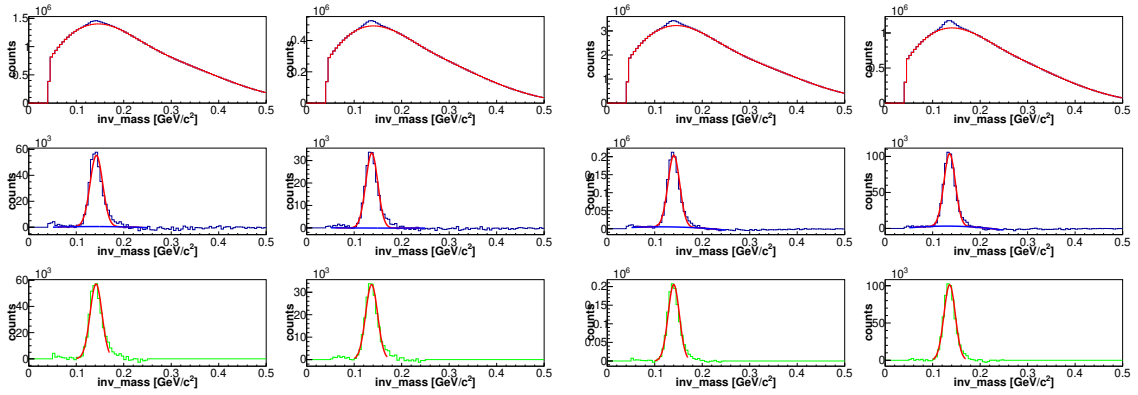

Figure 4.7: Same procedure as Fig.4.6 with asym=1.

4.2.6 Centrality Selection

Figure 4.12 (left) displays the raw yields per event of π^0 for different centrality categories, where 0- 5% are the most central collisions and 70-80% represent the most peripheral collisions. The proportions of each class relative to the minimum bias (MB) centrality are also displayed. The yields, obtained from MB trigger data, are multiplied by powers of 10 to enhance clarity. The data collected on the right side, using the high-energy deposit trigger (ERT), expand the range of (transverse momentum) to 4-6 GeV/c.

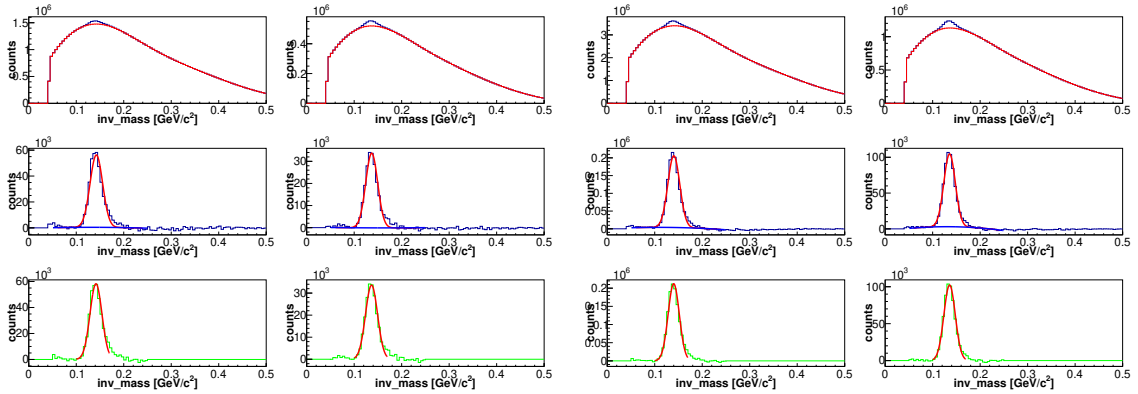

Figure 4.8: Same procedure as Fig.4.6 with asym=2.

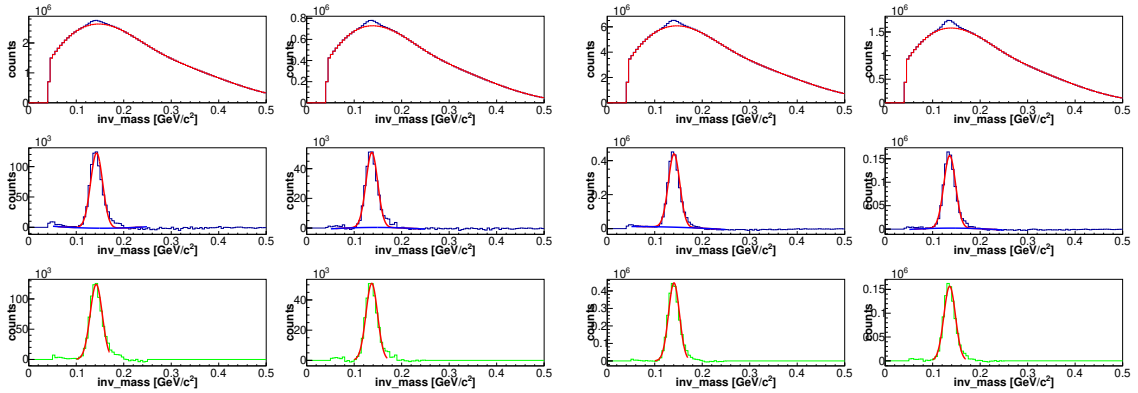

Figure 4.9: Same procedure as Fig.4.6 with PID=1.

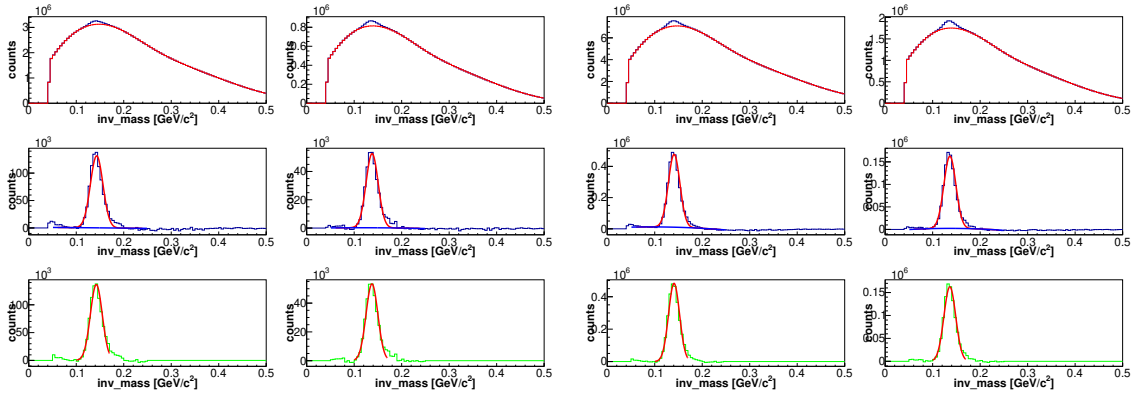

Figure 4.10: Same procedure as Fig.4.6 with PID=2.

4.2.7 MB and ERT Combination

In order to obtain a continuous spectrum of π^0, we merge the raw spectra obtained from the BBCLL1>0 tubes with a narrow vertex and an MB trigger, along with the ERT-triggered data set. Within the range of 5-10 GeV, we determine the ratio between the raw spectra of MB and ERT. By applying a constant ratio, the process of normalizing one dataset to another guarantees that their forms align perfectly, enabling smooth integration of the spectra. A transition point (Pt) is selected to

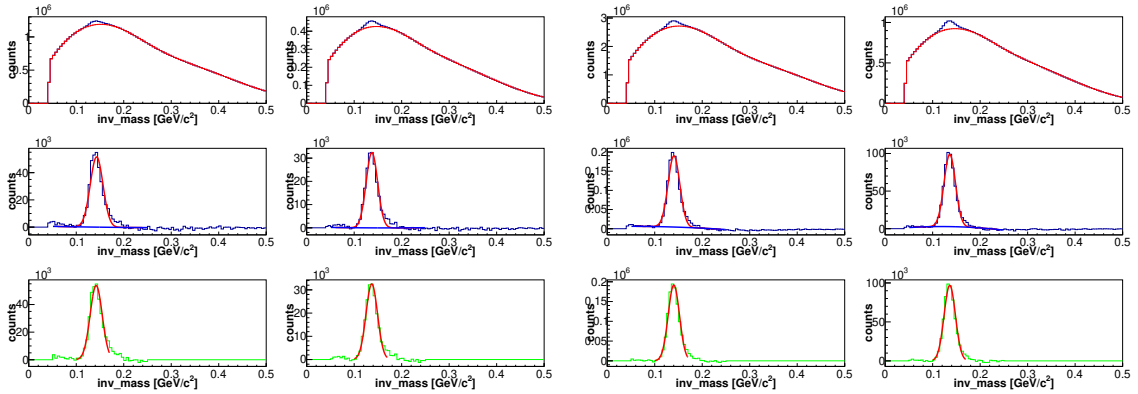

Figure 4.11: Same procedure as Fig.4.6 with TOF=1.

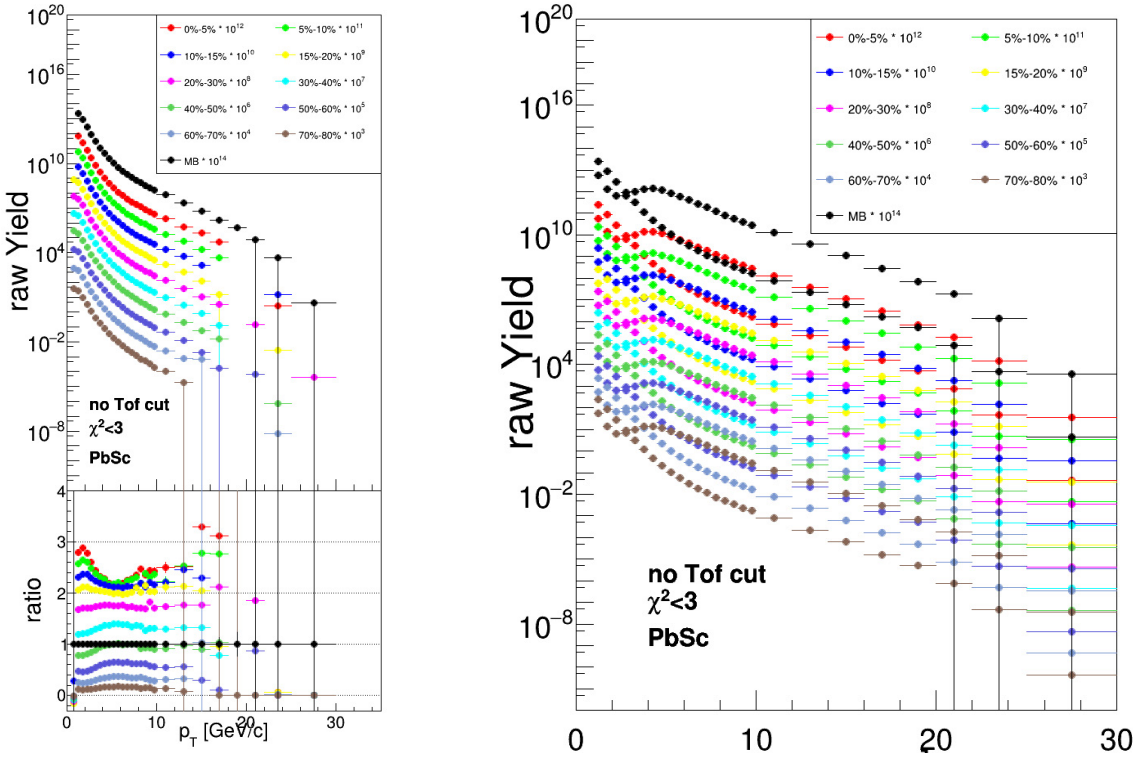

Figure 4.12: The left panel: Raw per event yield of π^0 in centrality classes for MB & ERT trigger.The right panel: Raw per-event yield of π^0 in centrality bins(upper) and the ratios of individual centrality to MB(lower).

delineate the boundary between the usage of the MB dataset below this point and the ERT dataset above it. The Ratio_Norm_ERT_MB.C code implements a method that guarantees a seamless and unified spectrum (see 3.4).

4.3 Different π^0 Windows Examination

The extraction of the raw π^0 count was conducted using a standard method as detailed in 4.2. The fundamental process includes invariant mass reconstruction

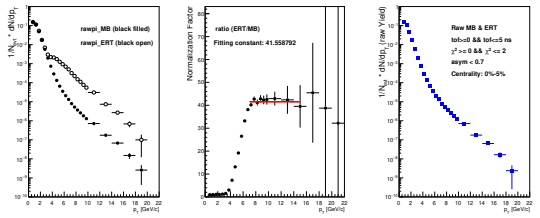

(a) ERT/MB ratio and normalized spectra, cc=0 (PbSc). Cuts: pid=0, tof=0, asym=0.

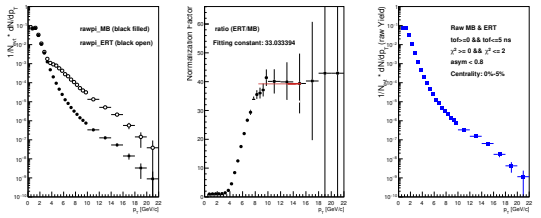

(b) As (4.13a), cc=0 (PbGl). Cuts: pid=0, tof=0, asym=0.

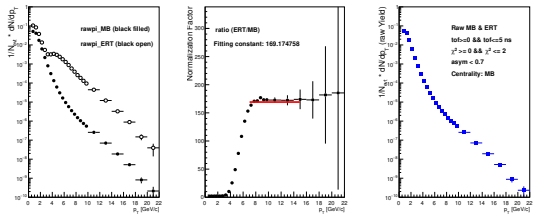

(c) As (4.13a), cc=MB (PbSc). Cuts: pid=0, tof=0, asym=0.

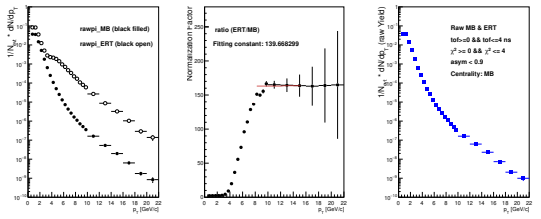

(d) As (4.13a), cc=MB (PbGl). Cuts: pid=0, tof=0, asym=0.

Figure 4.13: ERT/MB ratio and normalized spectra for different centralities and calorimeters. (a) and (b): centrality class 0 (PbSc and PbGl), (c) and (d): centrality class 12 (PbSc and PbGl).

and background elimination to extract the π^0 signal. To examine the impact of differing invariant mass window widths of [0.07 - 0.20] GeV 4.14a, [0.08 - 0.19] GeV 4.14b, and [0.09 - 0.18] GeV 4.14c on the extracted yields. This methodology enabled an in-depth analysis of the sensitivity of the π^0 yield to these parameters, hence assuring the reliability of the extraction technique and enhancing the signal-to-background ratio.

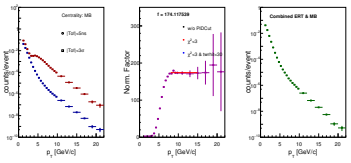

(a) 0.07 - 0.20 GeV

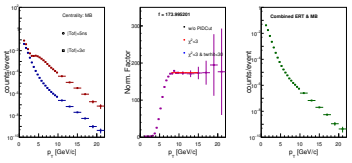

(b) 0.08 - 0.19 GeV

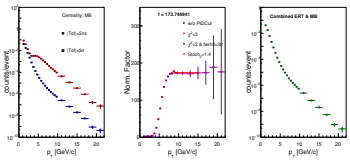

(c) 0.09 - 0.18 GeV

Figure 4.14: Comparison of π^0 yields extracted using three different selections shown in the left panel for CC=MB (0-93%). The middle panel displays the normalization factors. The right panel shows the combined normalized spectra from the ERT and MB triggers, demonstrating the consistency of the results across the different window sizes.

4.4 Raw Inclusive Photons Measurement

In high-energy physics, studying photons is crucial, especially to distinguish them from hadrons and electrons. Using the EMCal and its core cluster method,

we analyze particle energies by examining the shower energy fraction in EMCal towers. Assuming a photon hits the center of a tower perpendicularly, core clusters consist of towers that each contain more than 2% of the total energy. Applying additional cuts, one can reconstruct the core energy, E_{core}, for photon identification.

The towers belonging to a core cluster are defined by:

$$E_{\text{core}} = \sum_{\frac{E_{i,\text{pred}}}{E_{i,\text{meas}}} > 0.02} E_{i,\text{meas}},$$

where $E_{i,\text{pred}}$ and $E_{i,\text{meas}}$ are the predicted and measured energies of the i-th tower and $E_{i,\text{pred}}$ is it's predicted energy deposit by the shower shape profile.

- Energy threshold for Ecore.
- Bad tower rejection.
- Shower shape profile test using χ^2.
- Charged particle rejection.

These stochastic cuts are frequently combined in various ways to optimize the analysis [26].

4.4.1 Raw Inclusive Photons Preparation

Obtaining the inclusive raw photon yield (using Gammaextract_0210.C, 3.4) follows the same processes as for π^0 mesons 4.2. EMCal observes photon spectrums with identical PID cuts, consistent timing cuts, and particle identification for π^0 4.15. The normalization constants derived from separate MB and ERT trigger data provide consistency and direct comparability between photon and π^0 measurements. The normalization constants determined for π^0 and photon were about the same.

4.4.2 Raw Inclusive Photon Normalization

Normalization ensures that MB and ERT spectra are adjusted for event statistics and detector efficiencies before combining. This process scales each dataset and centrality class to a common reference 4.16. Normalization allows meaningful comparison and combination of minimum bias and triggered spectra, ensuring reliable insights into photon production mechanisms across different experimental conditions. By normalizing, we ensure that the combined spectra accurately reflect the true photon production rate, providing a reliable representation of the photon yield in the collision events.

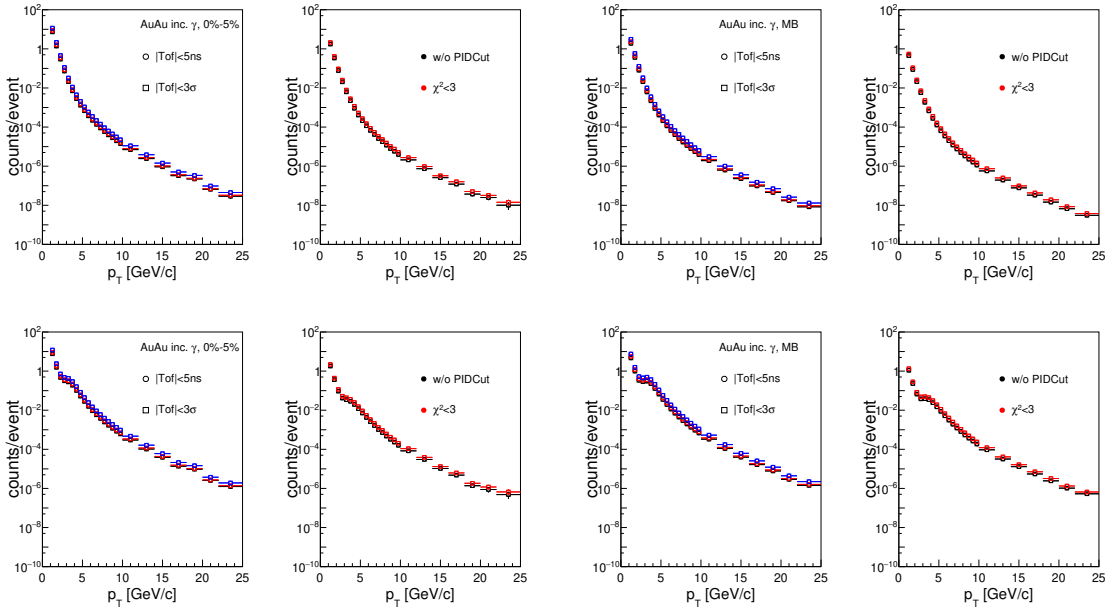

Figure 4.15: The provided data consists of two panels. The upper panel displays the raw inclusive photon spectrum from the MB dataset, while the lower panel shows the same spectrum obtained via ERT. Each panel is further divided into two sub-panels. The right sub-panels correspond to centrality with CC=MB (0-92%), while the left sub-panels represent CC=0 (0-5%).

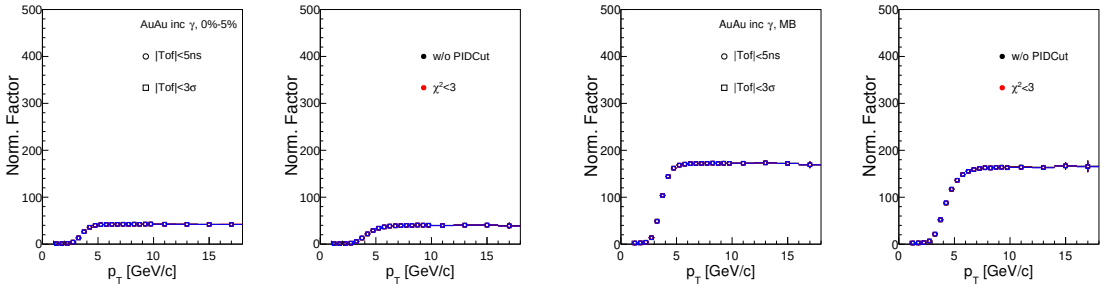

Figure 4.16: The raw inclusive photon is normalized separately for each centrality. In the right two panels, the centrality is CC=MB (0-92%) for PbSc(left) and PbGl(right), while in the left two panels, the centrality is CC=0 (0-5%).

4.4.3 Combining Two Primary Datasets

The merging of separated data sets aims to improve the precision of statistics and expand the possible range of observed spectra. The MB and ERT datasets were combined for this study. They assist in collecting the complete range of photons, including every spectrum, for various centrality categories from datasets triggered by MB (BBCLL1(> 0 tubes) narrowvtx) and ERT. The approach is analogous to those employed for π^0. We shall explain the process:
Within the energy range of 5-10 GeV, we calculate the ratio of raw photon spectra obtained from both the MB and ERT datasets. By use of a constant fit, we standardize one dataset to the other by utilizing this ratio. This ensures that

their shapes are in ideal position and can be easily fitted together. To combine the spectra: Determine the ratio of the raw photon spectra inside the region of overlap. Standardize one dataset to align with the other using this ratio. This ensures that everything runs smoothly at the point of transition (p_T). The MB data provide wide coverage, while the ERT data enhance the high p_T range, allowing for a detailed examination of photon production in both datasets. Graph both the MB and ERT spectra together. Choose a value for p_T at which the transition from MB data yield to ERT data yield occurs smoothly i.e. their ratio is constant. The analysis is conducted for different centrality classes (CC). These classes indicate the percentage of overlap between the colliding nuclei:
CC=MB (0-92%): This course covers almost all collision incidents, and exhibits a wide array of collision categories.
CC=0 (0-5%): This category exclusively comprises the most central collisions characterized by the greatest degree of nuclear overlap. The combination of MB and ERT spectra is performed individually for each centrality class. Figure 4.17 displays the outcomes, showing raw photon spectra comprising various centrality categories.

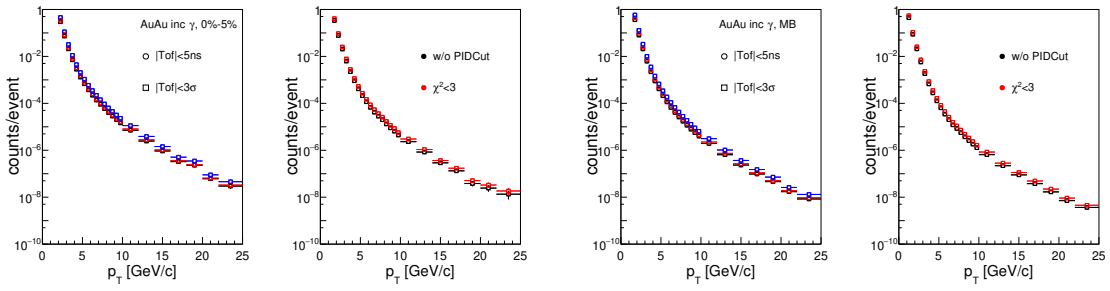

Figure 4.17: Raw inclusive photon spectra. The right panels for CC=MB (0-92%), and the left panels for CC=0 (0-5%). Each panel includes data from both MB and ERT datasets.

4.4.4 Benefits of the combination

As seen in Fig. 4.18, combining the MB & ERT spectra has many useful benefits.
Increased Statistical Precision: Statistical uncertainties decrease as we combine data from both sets, particularly at high p_T.
Wider p_T Range: Here, the ERT dataset excels. It improves measurement possibilities at high p_T, completing the gaps and fitting in smoothly with the MB dataset's entirety.
Uniform Examination Throughout Centrality Classes: The merging technique we employ is the same for all centrality classes. This maintains uniformity throughout and facilitates the comparison of different centralities.

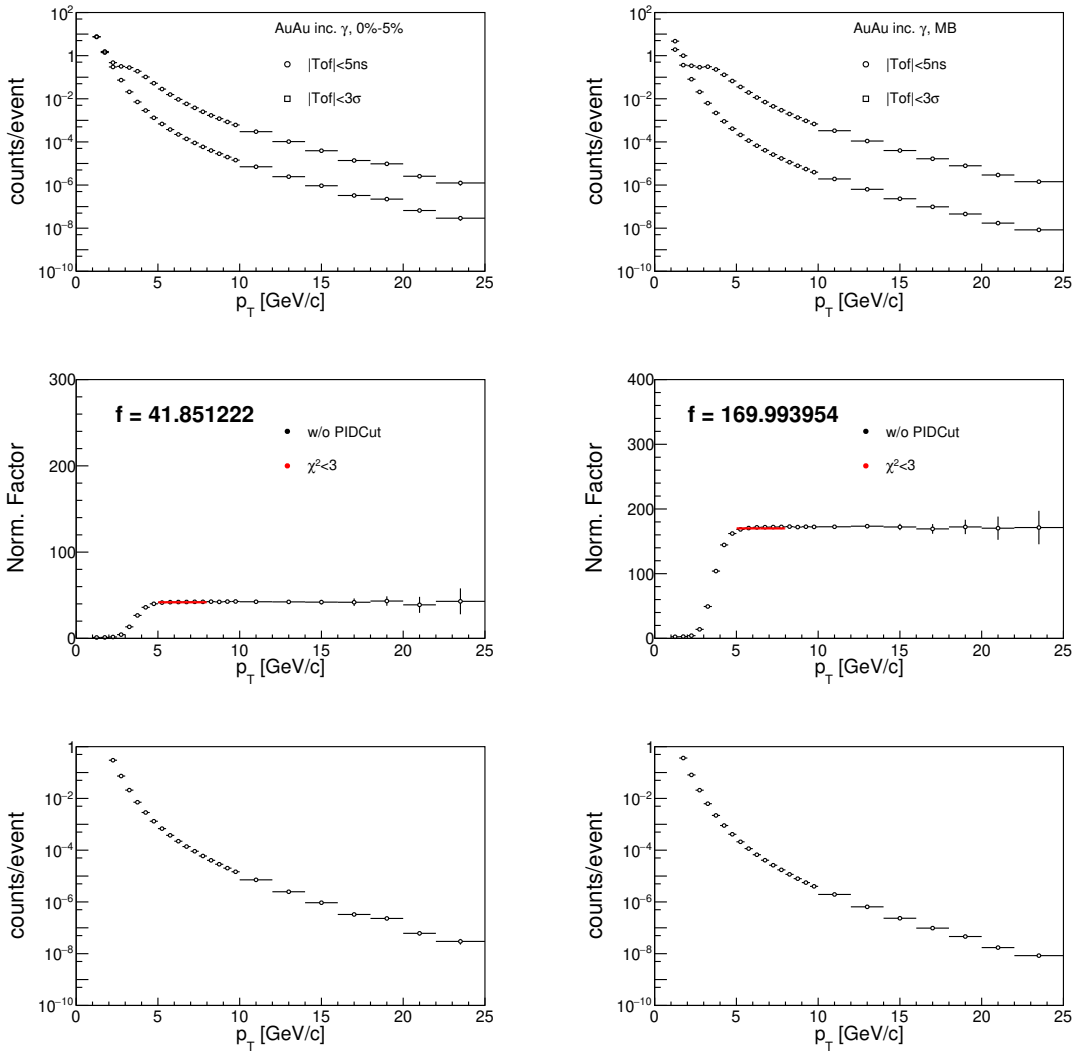

Figure 4.18: The 1st row show the raw inclusive photon spectra for MB % ERT. The left panel show the spectra for CC=0 (0-5%) and the right panel show the spectra for CC=MB (0-92%). 2nd row shows the normalization and the 3rd row shows the Merging MB and ERT spectra.

4.5 Simulation Framework

In this research, we applied simulations to take into account different detector-related effects that affect the accuracy of the reconstruction of π^0 and their decay photons. The main reliance of this study's detector acceptance, efficiency, and smearing effect correction is on simulation. For the next study of each of these components, the π^0 and it's decay photons will act as points of reference. Following is a detailed examination:

- Acceptance of the detector:
  - Rapidity Coverage: Only $\eta = \pm 0.35$ of the created π^0 mesons are detected by the EMCal detector, indicating that a large fraction of them

escape detection. And we only have half the azimuth covered, π instead of 2π.

- Bad Towers: During a run, not every EMCal tower operates as intended. As explained in Section 4, bad towers (dead, warm, and hot) are not included in the study.
- Sector Requirement: Reconstruct only π^0 that have both decay photons in the same sector. This results in a lower acceptance at low pT, but a much better signal-to-background ratio, which facilitates and improves the π^0 yield extraction (better signal/background ratio).

- Efficiency:
  - Photon Identification: Because the EMCal relies on shower shape comparisons, errors in the clustering method and natural fluctuations may cause actual photon showers to be misidentified or excluded (efficiency loss). Also, some hadrons might be mistakenly identified as photons (contamination).
  - Merging: Small opening angles of decay photons lead to reconstruction problems and clusters would merge at high p_T. Multiple reconstructions of photons may also arise from the disintegration of photon clusters.

- Smearing:
  - Momentum Mis-measurement: Because of the detector's limited resolution, photon momentum can be mis-measured, which can have an impact on the π^0 invariant mass and momentum.

4.6 π^0 Simulation

The PHENIX Integrated Simulation Application(PISA) is a simulated PHENIX. Based on a specified distribution, π^0 is created and sent into PISA. They decay very instantly into decay photons. The decay photons propagate in the detectors. Doing a measurement in simulation, we can track back the acc*eff of the detector. Afterwards, one could correct the raw spectrum by this acc*eff. In this study, a 2-Dimensional response matrix is employed for the correction. The simulation and correction of single photons would follow the same logic.

4.6.1 Oscar's Input Generation

PISA receives created input events in Oscar format. The following distributions are used to select events at random for each simulation event:

- Rapidity: produced using a Gaussian distribution with a mean of 0 and a standard deviation of 10 within the range $[-0.5, 0.5]$.

- The values of the transverse momentum (P_t) are uniformly distributed between 0 and 30.
- The azimuthal angle values (Φ) are uniformly distributed between $-\pi$ and π.

Secondary parameters like px, py, pz, and energy are determined using these fundamental parameters and the mass of the π^0. These secondary parameters are recorded (or saved) in together with the positions (x=0, y=0, z=vertex, and t=0).

4.6.2 PISA

PISA processes the single π^0 and handles the decay of the π^0 and the decay photon's interaction with various detector subsystems.
The energy deposited by the decay photons in the EMCal detector and their impact point along with the truth information of the original π^0 is the primary information created and preserved from this step.

4.6.3 Embedding

Many particles are produced in each event and distributed at random throughout the detector. At this point, we simulate single particles (one particle per event), i.e., we simulate a "clean" measurement, and GEANT provides us with the energy deposit from these pi0-photons only that has been correctly smeared. However, in the actual event, a different particle might also contribute to the energy deposits in some of this GEANT cluster's towers. The resulting reconstructed photons would then give a different p_T or, in extreme cases, even push the reconstructed invariant mass beyond the π^0 mass window. The calorimeter would then, of course, measure the SUM of the two energies (true π^0 and "underlying event"), distorting the measured energy (beyond natural smearing). As a result, the reported π^0 yield decreases. To obtain the energy in each tower from the real event, we first "decluster" the real event in the simulation Next, we add the simulated energy to those towers where the simulation also generated energy, and we reclusterize. Using the code PisaEmbed.csh and all_new_result.root 3.4, information is kept regarding whether a tower has energy provided by the simulated event and, if so, attributes of the original simulated particle.

4.6.4 Response Matrix for Raw π^0 Spectrum

The response matrix describes the probability that a true value x is reconstructed at value y, where y belongs to the set of all possibilities. The generated and measured p_T of the π^0 is recorded for every event. The generated p_T is represented by the x-axis, while the measured p_T is represented by the y-axis, in a two-dimensional matrix. This 2D matrix is filled by very high statistics. During this procedure, real analysis cuts are applied, producing a response matrix unique to those cuts (using the code myEmbedPi0NoWeight.C 3.4). Afterwards, the identical approach was used for Run 16, and ratio2dMatrix_Run14and16.C

3.4 was utilized to compute the disparity between them. Upon examining this comparison, I have seen that they are almost identical, with just a little difference in the systematic ratio in the right panel of Fig. 4.19. In theory, the ratio between them should be 1. Therefore, our next objective is to investigate the underlying cause of this systematic disagreement.

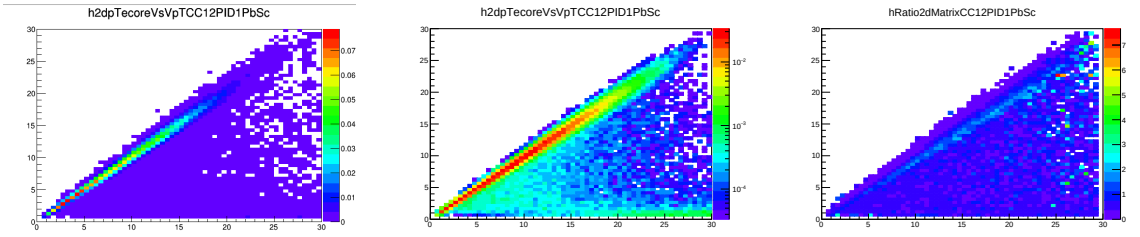

Figure 4.19: Response Matrix of π^0: The generated P_t is represented by the x-axis, while the measured P_t is represented by the y-axis for run 14 on the left, run 16 in the middle and the ratio run 14 over run 16 on the right, with PID=1

4.6.5 Unfolding Raw π^0 Spectrum

It is possible for the measured p_T of the π^0 to deviate from its produced p_T. Any of the causes listed in section 4.5 could cause this. It is necessary to adjust the acquired raw yield spectrum for these impacts. In theory, the matrix should be inverted in order to derive the real spectrum from the observed spectrum. However, the inverse is known for its instability due to tiny, erratic off-diagonal components. We merely (implicitly) assume that the genuine spectrum is a smooth function with a derivative that varies slowly. To get the "measured" spectrum, I used two methods; the first included using several fitting functions to correct the spectra. However, this approach yielded a significant final fractional ratio,4.20, so I used another strategy that started with a "trial function" and use the 2D matrix to calculate the detector's response if the trial function were correct. Next, we contrast this "measured" spectrum with my raw spectra, which are what I actually saw in the data. They are not the same. I now adjust my "trial function" using their ratio and recalculate what I would obtain if I used this adjusted trial function as "measured" using the 2D matrix. This is not closer to the observed raw spectra, but still differs from them. I then repeat the process. Regarding data points, statistical analysis should primarily focus on their point-by-point variations (although significant general distortions, such as those resulting from acceptance that fluctuates substantially with p_T, are permitted). For π^0, the initial trial function (T) is obtained by fitting previously published data (AN590) [91] with Hagedorn function. Obtaining a stable response matrix is a statistically heavy process, and thus about 200 million events with single π^0s were simulated. This is done for all centralities to obtain centrality binned corrected π^0 spectrum.

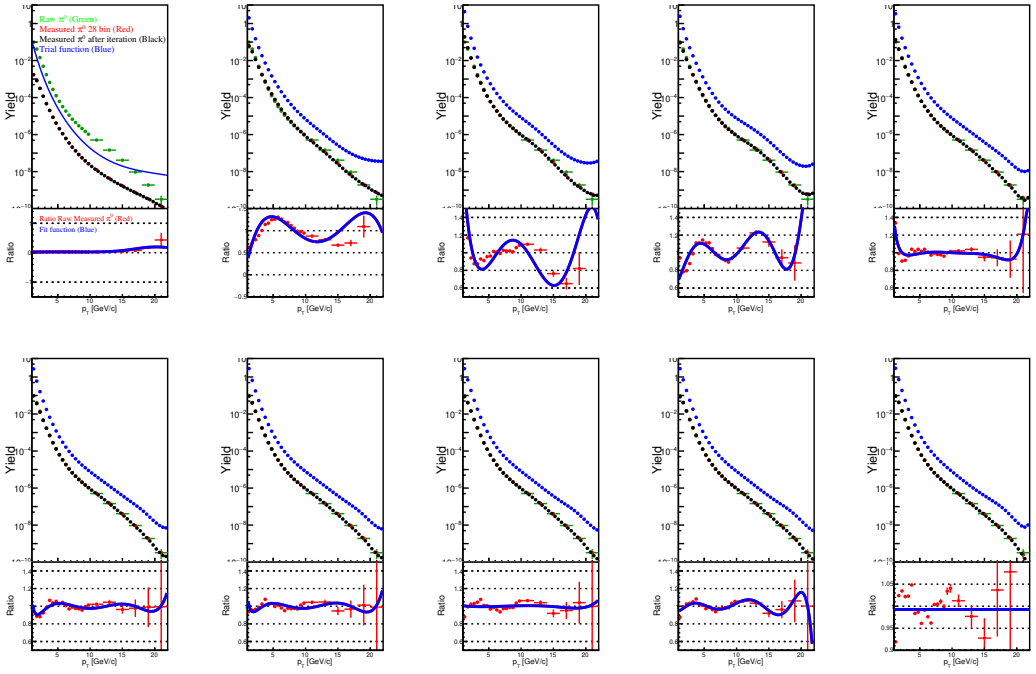

Figure 4.20: Fitting correction for π^0 extraction, performed over 10 iterations, for the PbSc, cc=MB, PID=0, TOF=0, and ASYM=1.

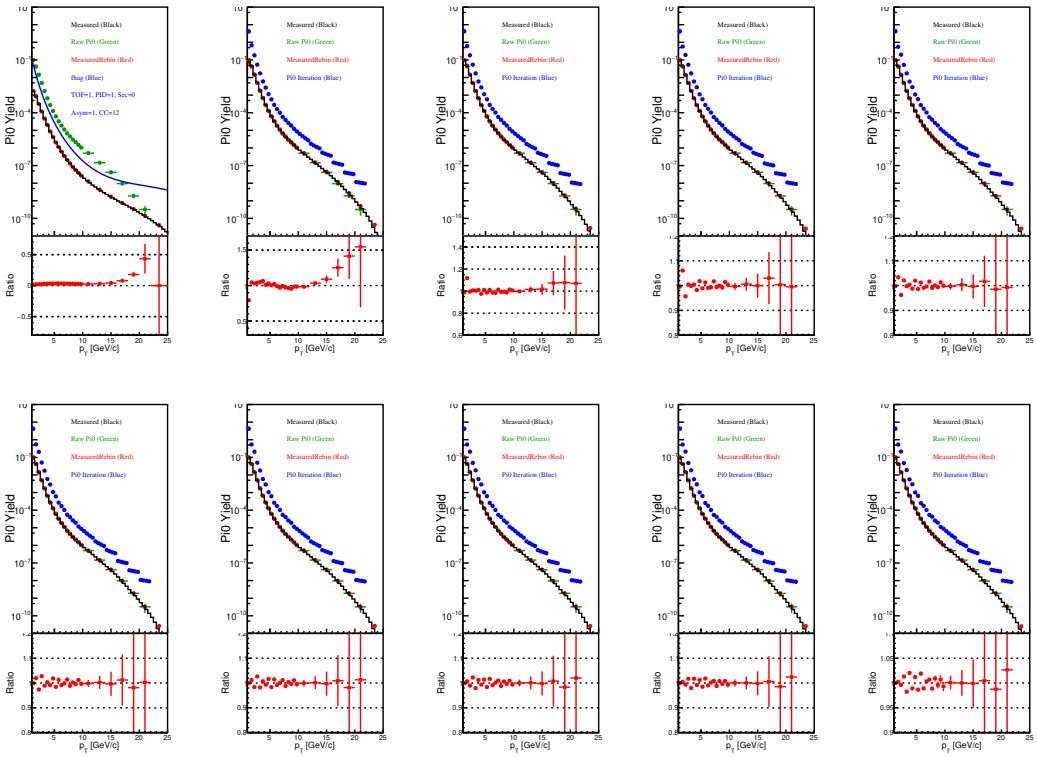

Figure 4.21: Point-by-point correction for π^0 extraction, performed over 10 iterations, for the PbSc, cc=MB, PID=0, TOF=0, ASYM=2.

As evident from the top left plot of Fig. 4.21, there is still a small noise in the corrected spectrum around 6.5GeV. This is due to residual normalization error in the matching MB and ERT triggered data set, and the method of unfolding with response matrix causes mismatch in the neighboring points around the transition region. The process used a 2D response matrix in Fig.4.19 to calculate the detector response to an initial estimation of the true spectrum. By comparing the ratio of the raw data to "measured" the initial estimation, the initial estimate is modified. This correction is repeated for 10 iterations until convergence is reached (by using two method the point by point from the code Pi0_Point_corr.C and fitting by using the code Pi0Correction_last.C3.4).

4.6.6 Unfolding of Different Raw π^0 Windows

The same point-by-point correction method 4.6.5 was applied to raw π^0 yields extracted from different integration windows. This approach ensures consistent unfolding and correction across varied window sizes 4.22, 4.23a, 4.23b allowing for reliable comparison of the resulting spectra.

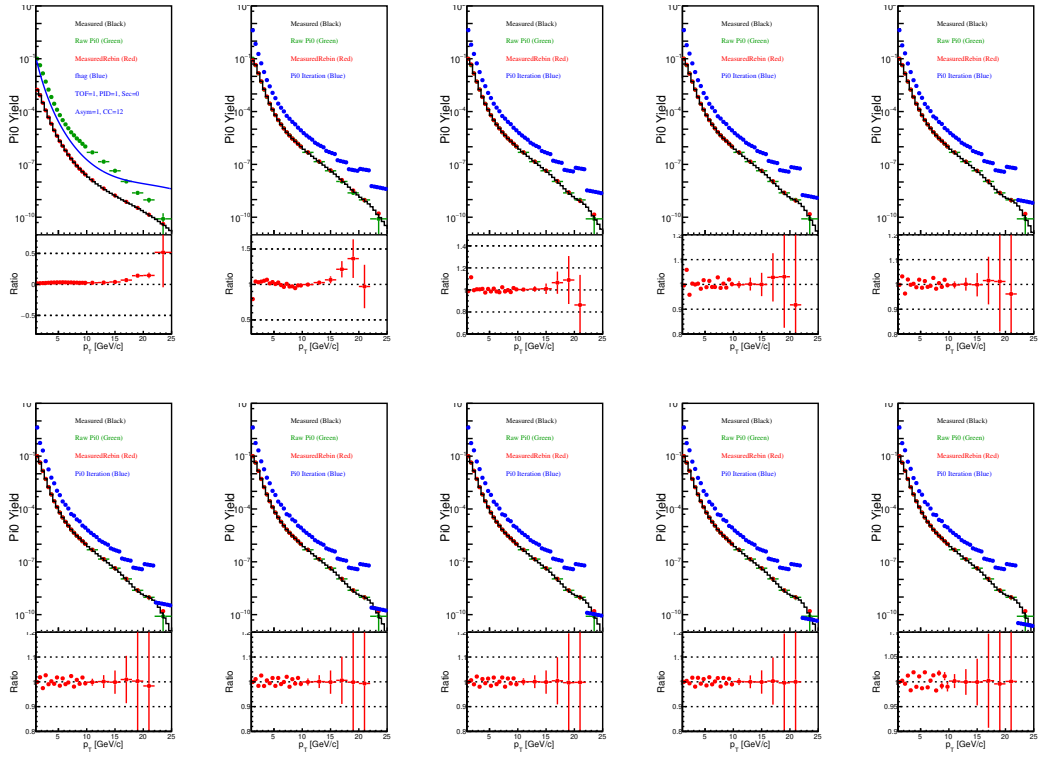

Figure 4.22: Point-by-point correction for π^0 extraction, performed over 10 iterations, window 07-20 Gev.

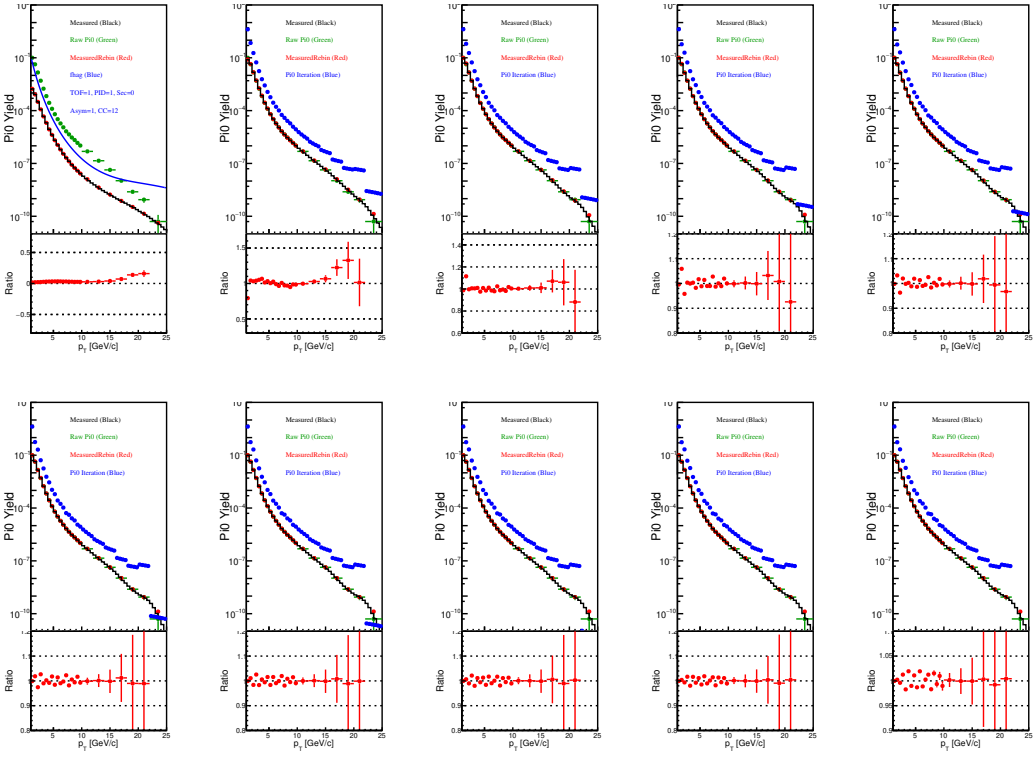

(a) Window 08-19 Gev.

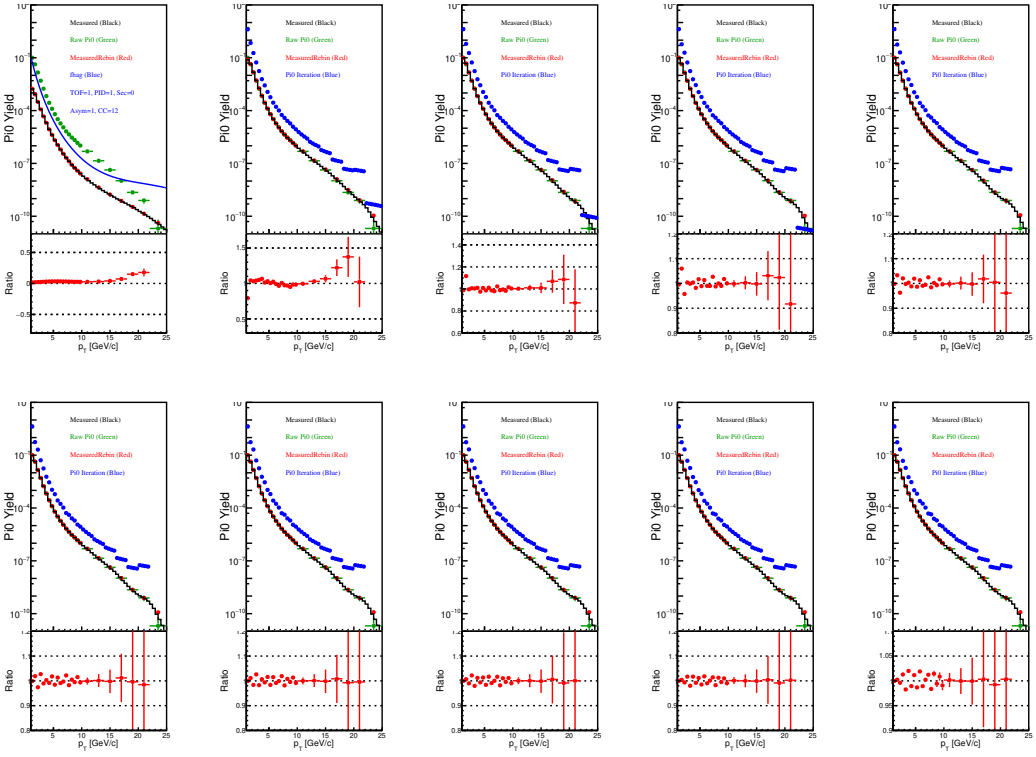

(b) Window 09-18 Gev.

Figure 4.23: Point-by-point correction for π^0 extraction, performed over 10 iterations, window 08-19, 09-18 Gev.

4.6.7 π^0 Invariant Yield

After obtaining the corrected π^0 yield through unfolding and efficiency corrections, the invariant yield is calculated, for different π^0 windows (4.24a, 4.24b, 4.24c, 4.24d), by normalizing the corrected spectra to account for detector acceptance, reconstruction efficiency, and transverse momentum (p_T) bin widths. The invariant yield is given by:

$$\frac{1}{2\pi p_T}\frac{d^2N}{dp_T d\eta}$$

where N represents the corrected number of π^0 mesons per event, p_T is the transverse momentum, and η is the pseudorapidity. This normalized yield enables meaningful comparisons with theoretical models and other experimental results, particularly to study medium effects in Au+Au collisions at $\sqrt{s_{NN}} = 200$ GeV.

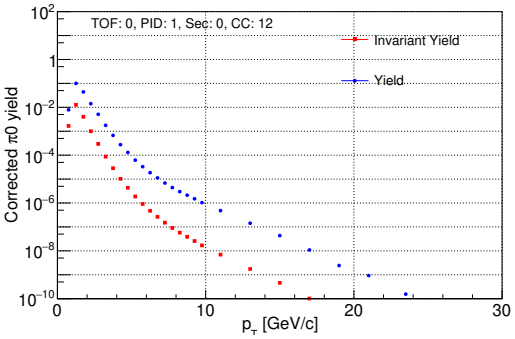

(a) Window 07-20 Gev

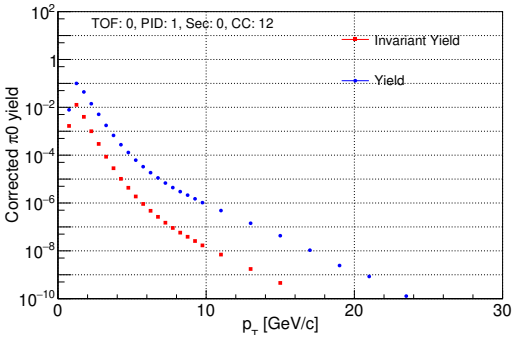

(b) Window 08-19 Gev

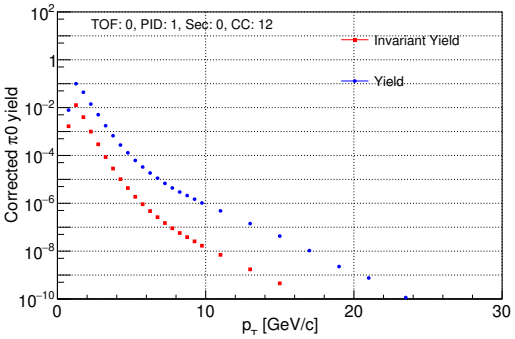

(c) Window 09-18 Gev

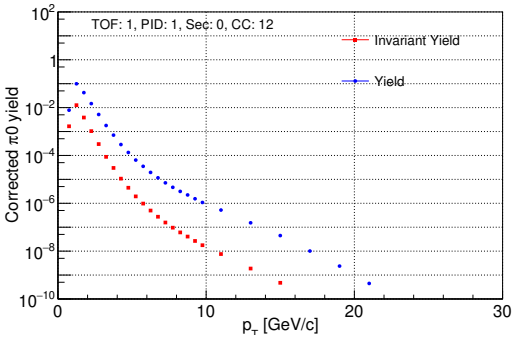

(d) Window 0.10 - 0.17 GeV

Figure 4.24: The invariant yield for corrected π^0 spectrum after 10 iteration for different windows

4.7 Direct photon Simulation

In high-energy nuclear collisions, direct photons are those emitted directly from the hot and dense medium formed in the collision, as opposed to photons from hadron decays. The direct photon spectrum provides valuable information about

the initial stages of the collision and the properties of the quark-gluon plasma (QGP). This document outlines the procedure for extracting the direct photon spectrum. The inclusive photon spectrum (γ_{incl}) includes all photons detected in the experiment. It is obtained through:

1. **Measurement**: Detecting all photons using electromagnetic calorimeters.
2. **Corrections**: Apply corrections for detector acceptance, efficiency, and resolution to obtain the true inclusive photon spectrum.

To obtain the direct-photon spectrum (γ_{direct}):

$$\gamma_{\text{direct}} = \gamma_{\text{incl}} - \gamma_{\text{decay}} \tag{4.1}$$

We compute the distribution of "raw" photons in the detector, which can be attributed exclusively to the raw decay photons. We do this by taking the fully corrected measured π^0 spectrum and process it with the 2D-matrix that represents how many decay photons are captured and identified by the EMCal 4.25a, 4.25b. The raw decay spectrum is then removed (subtracted) from the raw inclusive photon spectrum. After applying the simulated response for single (non-correlated) photons, the raw direct photon spectrum exists (by using the code GammaCorrection_for_new_simu.C 3.4).

4.7.1 Obtaining Decay Gammas from Corrected π^0 Spectrum

The π^0 mostly decays into two photons ($\pi^0 \to \gamma\gamma$). These photons are detected using electromagnetic calorimeters, which measure their energy and position. The invariant mass of the photon pairs is calculated to identify π^0:

$$m_{\gamma\gamma} = \sqrt{2E_1E_2(1 - \cos\theta)}, \tag{4.2}$$

where E_1 and E_2 are the energies of the two photons, and θ is the angle between them. To obtain the spectrum of decay photons from the corrected π^0 spectrum:

1. Each π^0 contributes two photons to the photon spectrum.
2. The energy and momentum distribution of the decay photons are derived from the kinematics of the parent π^0 meson.

The relationship between the π^0 transverse momentum ($p_T^{\pi^0}$) and the photon transverse momenta ($p_T^{\gamma_1}$, $p_T^{\gamma_2}$) is given by the decay kinematics:

$$p_T^{\gamma_1} = \frac{p_T^{\pi^0}}{2}(1 + \cos\theta^*), \tag{4.3}$$

$$p_T^{\gamma_2} = \frac{p_T^{\pi^0}}{2}(1 - \cos\theta^*), \tag{4.4}$$

where θ^* is the angle between one of the photons and the π^0 in the π^0 rest frame.

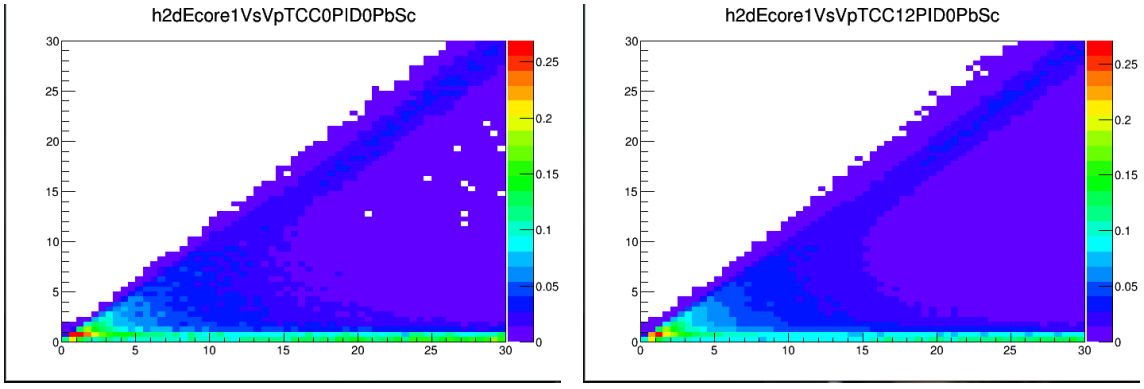

(a) CC0 PID0 PbSc **(b)** CC12 PID0 PbSc

Figure 4.25: 2D Decay Gammas from Corrected π^0 for cc=0 on the left and cc=MB on the right with PID=0 for PbSc).

4.7.2 Unfolding of Direct Photon Spectrum

Following the methodology established for π^0 analysis 4.6.5, we apply a similar iterative unfolding technique to extract the direct photon spectrum from the inclusive photon measurements 4.26b, 4.26a. Direct photons are those emitted promptly from the collision medium, distinct from decay photons primarily originating from π^0 decays.

The unfolding process utilizes a two-dimensional response matrix correlating the generated and measured transverse momentum (p_T) of decay photons, derived from detailed detector simulations embedding π^0 decay photons into real events. By applying this response matrix iteratively, we correct for detector acceptance, efficiency, and resolution effects on the measured inclusive photon yield.

After subtracting the corrected decay photon contribution, the remaining yield corresponds to the direct photons. The unfolded direct photon spectrum provides insight into the early stages of the collision and the properties of the quark-gluon plasma.

4.7.3 Invariant yield of direct photon

Calculate the invariant yield of direct photons:

$$E\frac{d^3N_{\text{direct}}}{dp^3} = \frac{1}{2\pi p_T}\frac{d^2N_{\text{direct}}}{dp_T dy}. \tag{4.5}$$

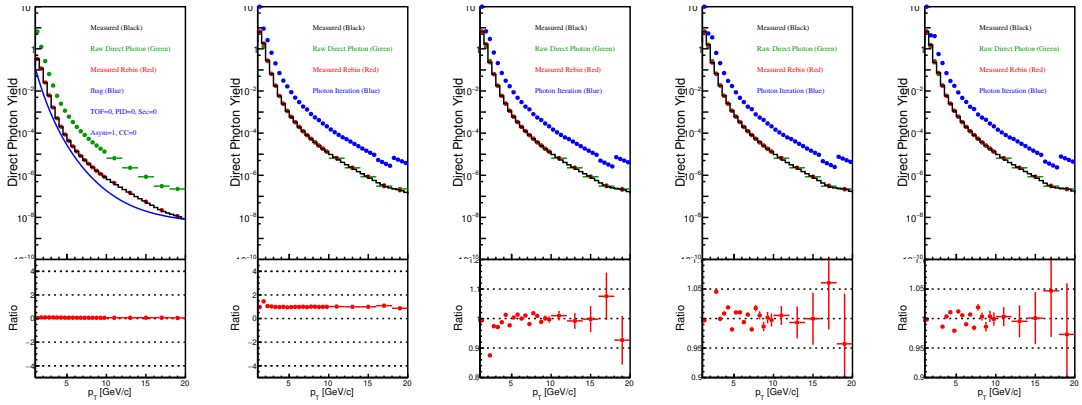

(a) cc=0, PID=0, tof=0 for PbSc.

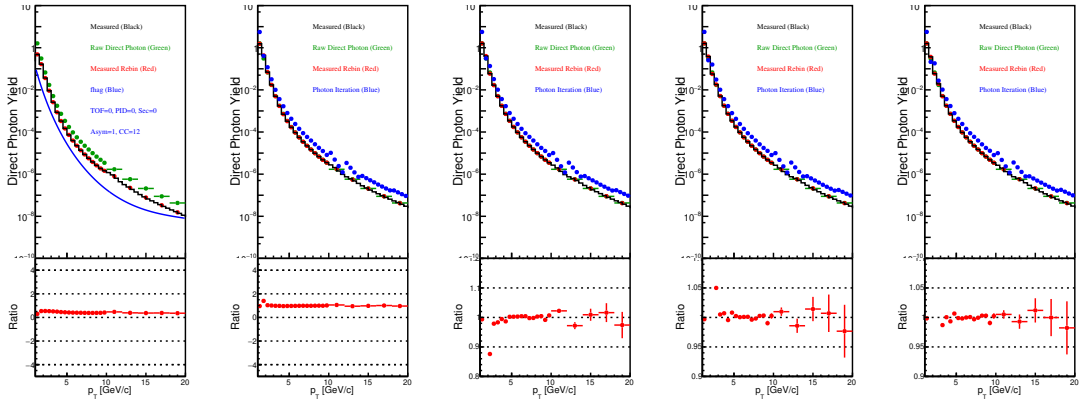

(b) cc=MB, PID=0, tof=0 for PbSc.

Figure 4.26: Corrected direct photon spectrum after 5 iteration for cc=0 on the first row and cc=MB on the second row.

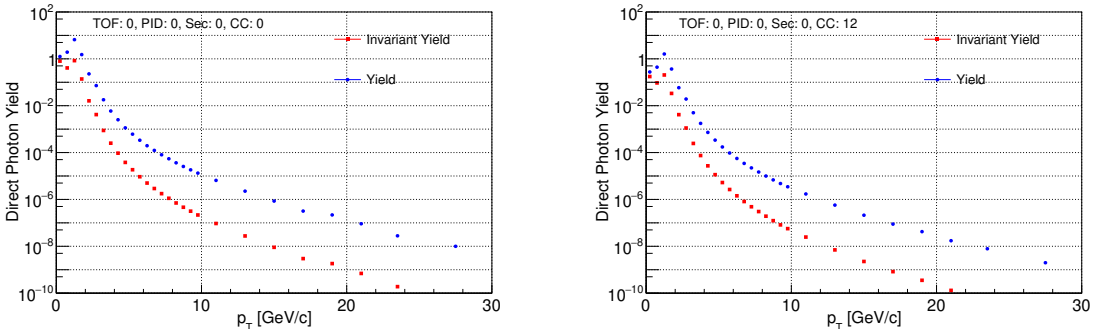

Figure 4.27: The invariant yield for corrected direct photon spectrum after 5 iteration for cc=0 on the left and cc=MB on the right with PID=1, tof=0 for PbSc.

4.8 Systematic Uncertainties

Understanding systematic uncertainties is vital for accurate measurements of π^0 and direct photon spectra. The following subsections summarize the main sources.

4.8.1 Raw π^0 Systematic Uncertainties

Raw π^0 count is extracted by the procedure mentioned in section 4.2.

PID Cut Variations

Different PID cuts ($\chi^2 < 2, 3, 4$) affect signal purity and efficiency. Figures 4.28 illustrate the impact of PID0, PID1 and PID2 on raw π^0 spectra (This output was obtained using the code Ratio_AuAu_raw_pi01.C 3.4).

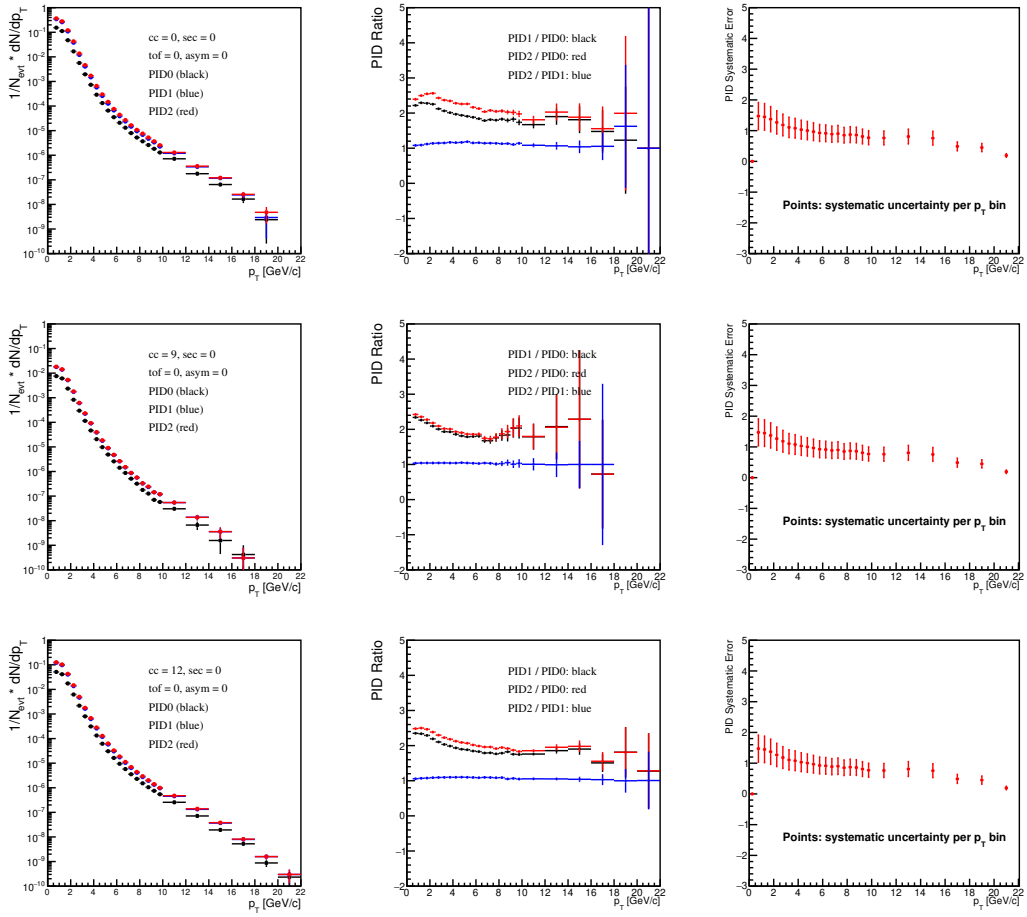

Figure 4.28: The π^0 raw yield on the left and in the middle the ratio for various PID (0, 1, 2) for TOF=0, asym=1 and on the right the systematic uncertainties.

Energy Asymmetry Cuts

The asymmetry cut controls the energy difference between photon pairs from π^0 decay. In Fig. 4.29 we display, for each individual asymmetry the raw π^0 spectra, and the ratios and systematic uncertainties. (This output was obtained using the code Ratio_AuAu_raw_pi01.C 3.4).

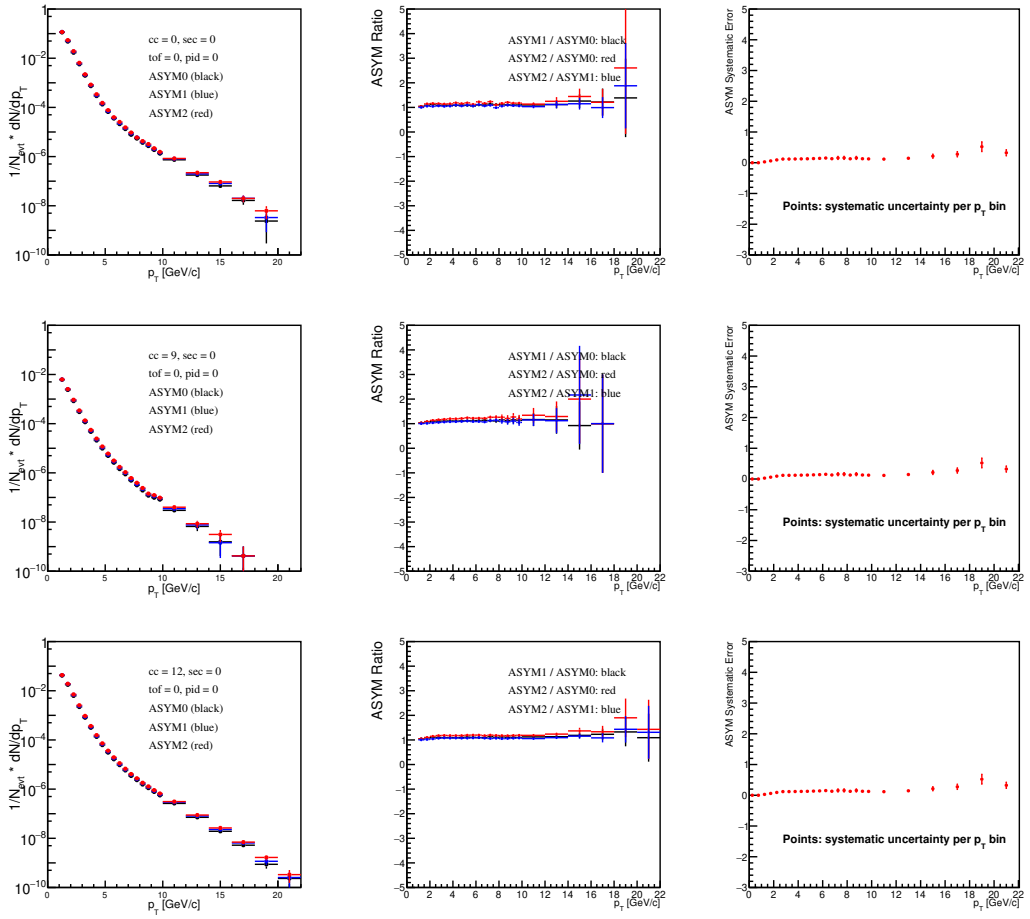

Figure 4.29: The π^0 raw yields on the left, ratios in the middle and systematic uncertainties on the right for various asymmetry 0, 1, 2 for cc=0 and cc=MB, TOF=0, PID=0.

4.8.2 π^0 Window Systematic Uncertainties

Evaluation of how different integration window sizes affect raw π^0 yields 4.30 and the corrected π^0 yields 4.31.

4.8.3 Corrected π^0 Systematic Uncertainties

PID Cut Variations

Different PID cuts ($\chi^2 < 2, 3, 4$) affect signal purity and efficiency. Figure 4.32 illustrate the impact of PID0 and PID1 and PID2 on corrected π^0 spectra.

Energy Asymmetry Cuts

The energy asymmetry cut ensures that the detected photons are consistent with the kinematics of π^0 decay. The energy asymmetry, A, is defined as:

$$A = \frac{|E_1 - E_2|}{E_1 + E_2}, \tag{4.6}$$

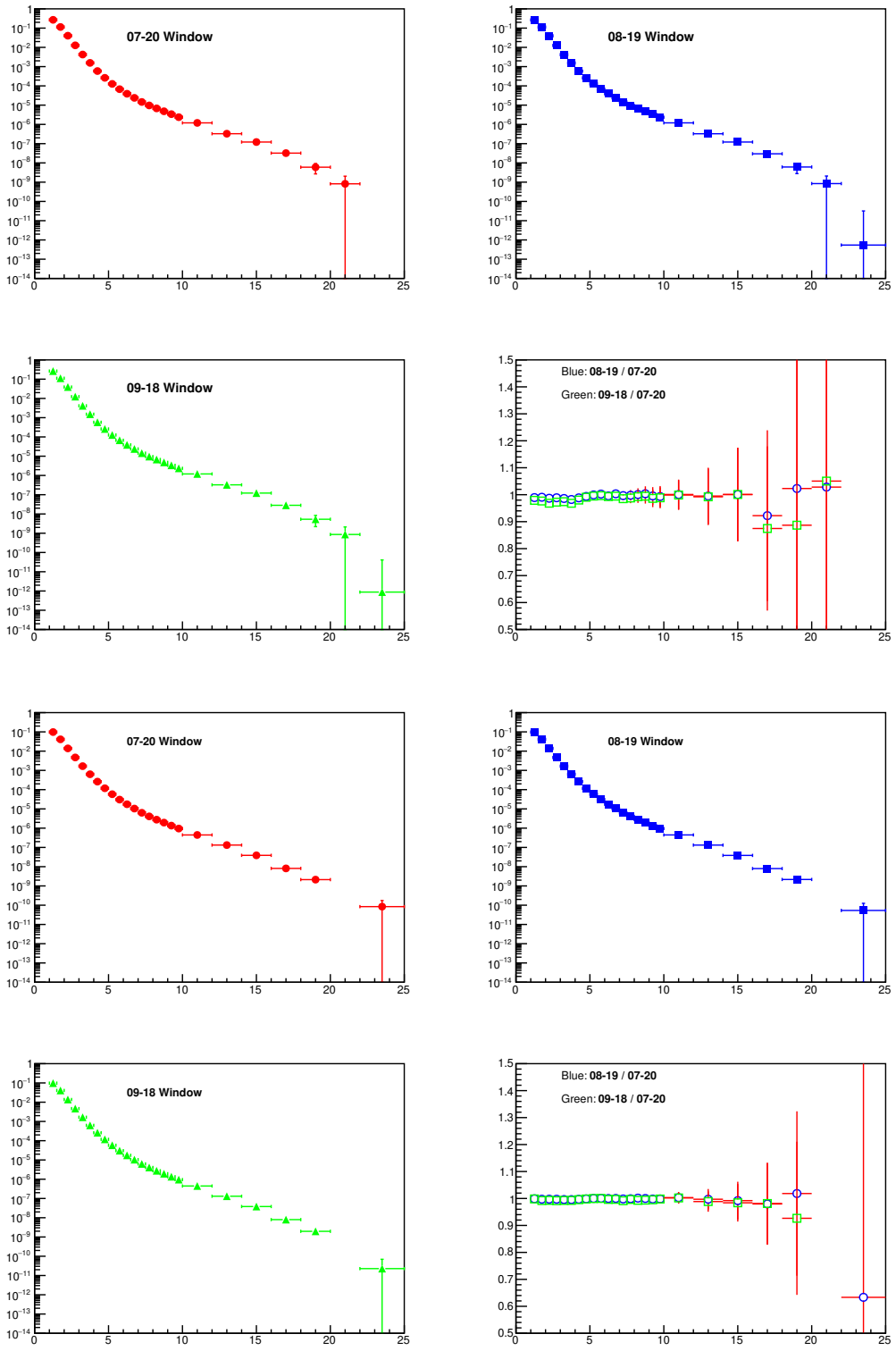

Figure 4.30: The π^0 raw yields for different window sizes on the left, ratios in the middle and systematic uncertainties at cc=0, cc=MB, asym=0, tof=0, PID=1, sec=0.

where E_1 and E_2 are the energies of the two photons from the π^0 decay. The asymmetry distribution of photons that truly come from π^0 decays is in principle

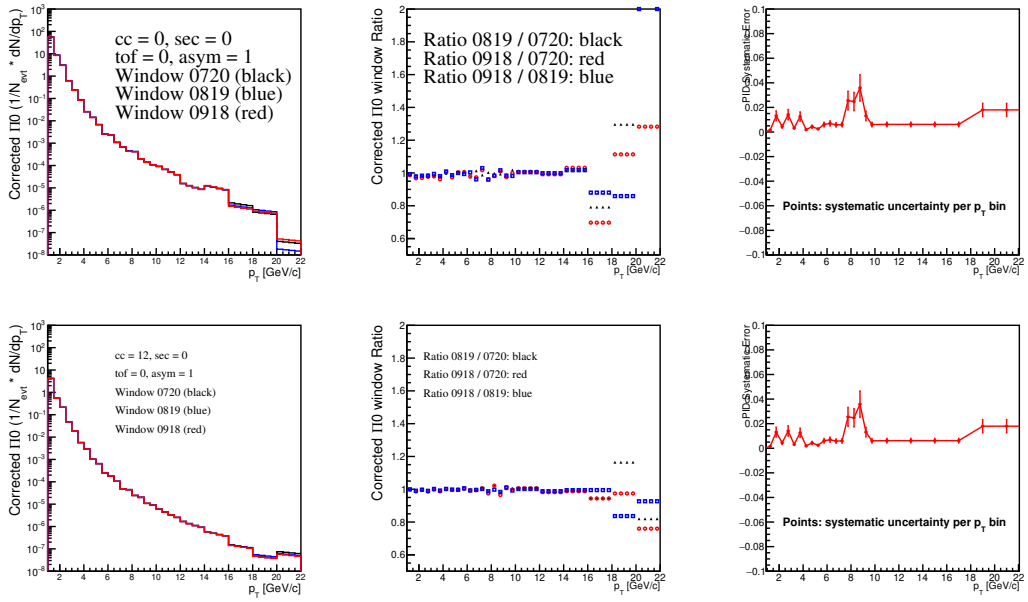

Figure 4.31: The π^0 corrected yields for different window sizes on the left, ratios in the middle and systematic uncertainties at cc=0, cc=MB, asym=0, tof=0, PID=1, sec=0.

constant, modified in the real-life experiment at very low asymmetries (loss due to cluster merging) and very high asymmetries (loss due to the single-sector requirement but substantial enhancement due to low energy clusters coming from hadrons, instrumental background (secondaries), etc. Figure 4.33 show this effect. $\frac{|E_1-E_2|}{E_1+E_2} < 0.7, 0.8, 0.9$.

4.8.4 Direct Photon Systematic Uncertainties

PID Cuts for Direct Photons

PID cuts on direct photon spectra (Figure 4.34) same method 4.8.3.

Time-of-Flight (TOF) Cuts

The background rejection and photon identification are affected by variations in TOF cuts, yet from what you can see, they are minor for both corrected π^0 and corrected direct photon (Figures 4.35a, 4.35) due to the detailed timing correction in section 3.2.

4.9 Summary of π^0 and Dir- γ Sys-Uncertainties

π^0 and direct photon was performed using key selection criteria:

- **PID:** Various particle identification levels (PID = 0,1,2) were applied to optimize signal purity.

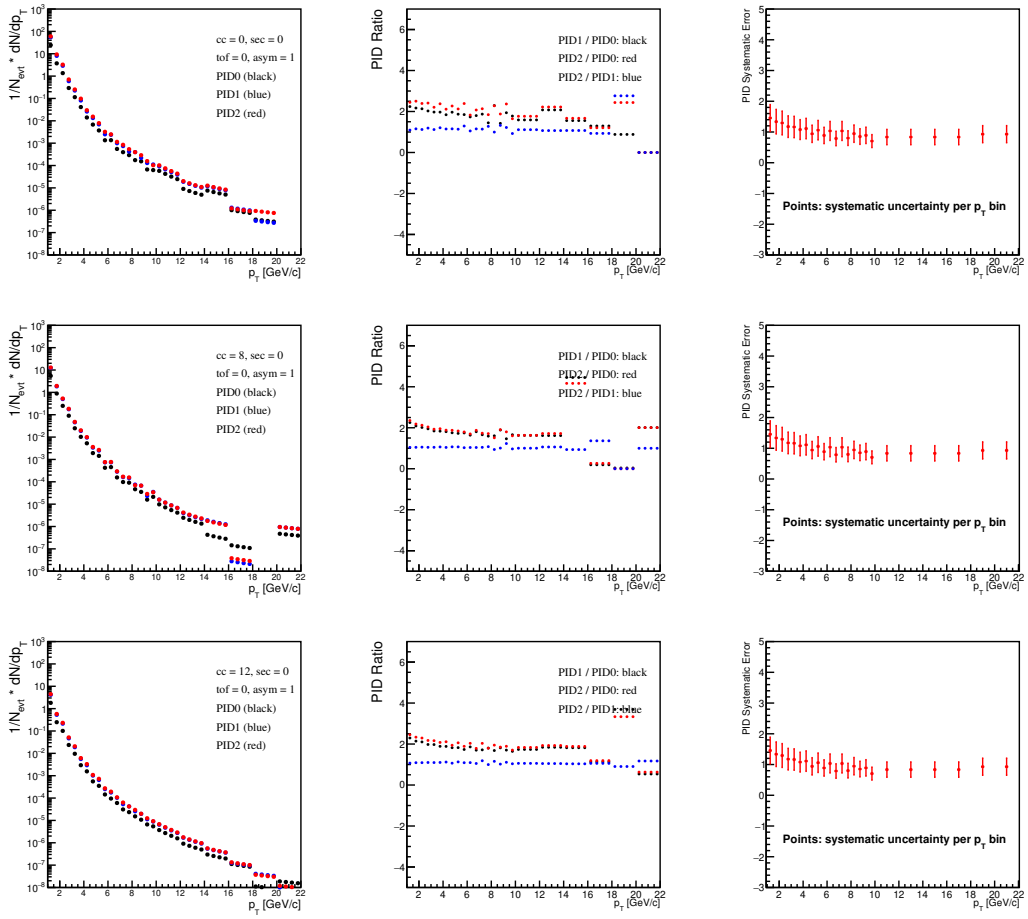

Figure 4.32: Effect of PID cut on corrected π^0 spectra for centrality classes cc=0, cc=8 and cc=MB (asym=1, tof=0, PbSc).

- **TOF:** Time-of-flight cuts (TOF = 0, 1) improved timing resolution and reduced background.
- **Asymmetry:** Different asymmetry windows (ASYM = 0,1,2) refined π^0 invariant mass reconstruction.
- **Mass Windows:** Multiple mass ranges were studied for effective π^0 peak isolation.
- **Raw and Corrected Data:** Both raw yields and efficiency-corrected data were analyzed to ensure reliable results.

This approach provided strong extraction of π^0 and direct photon signals, supporting precise physics measurements.

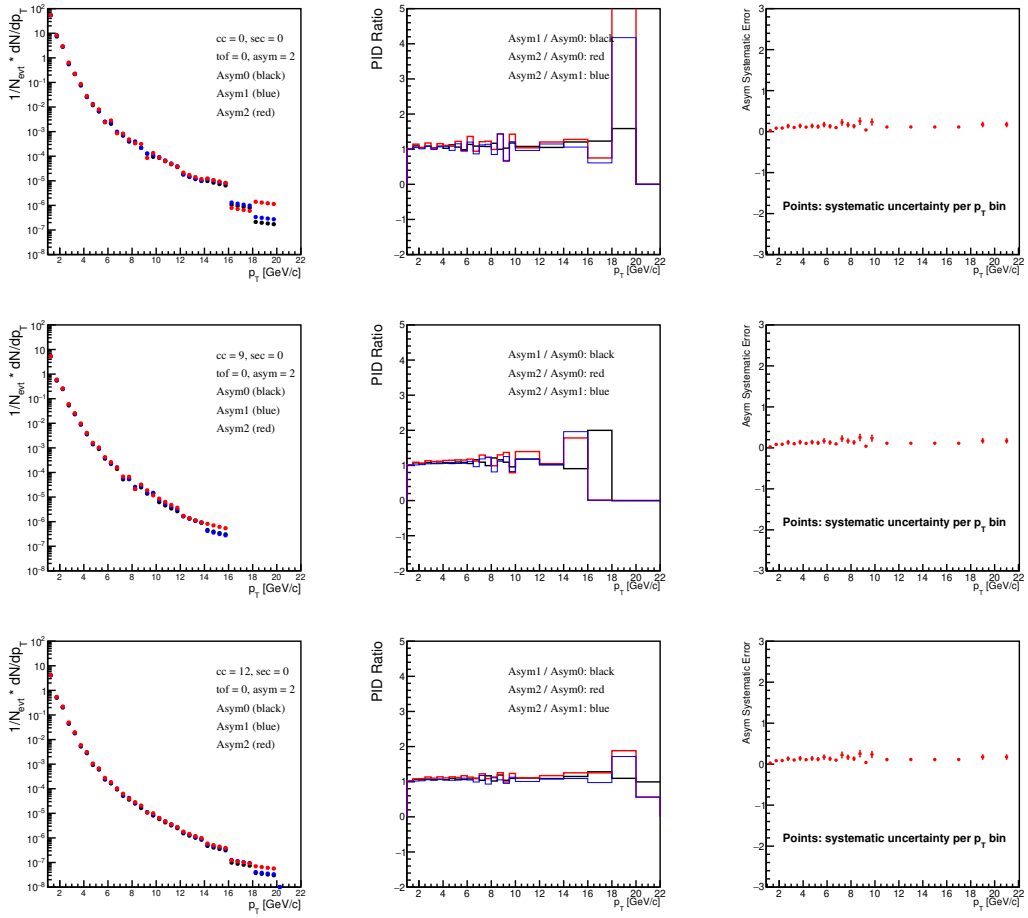

Figure 4.33: Effect of asymmetry cut ASYM on corrected π^0 spectra for cc=0,cc=9 and cc=MB with PID=1, tof=1,0 for PbSc.

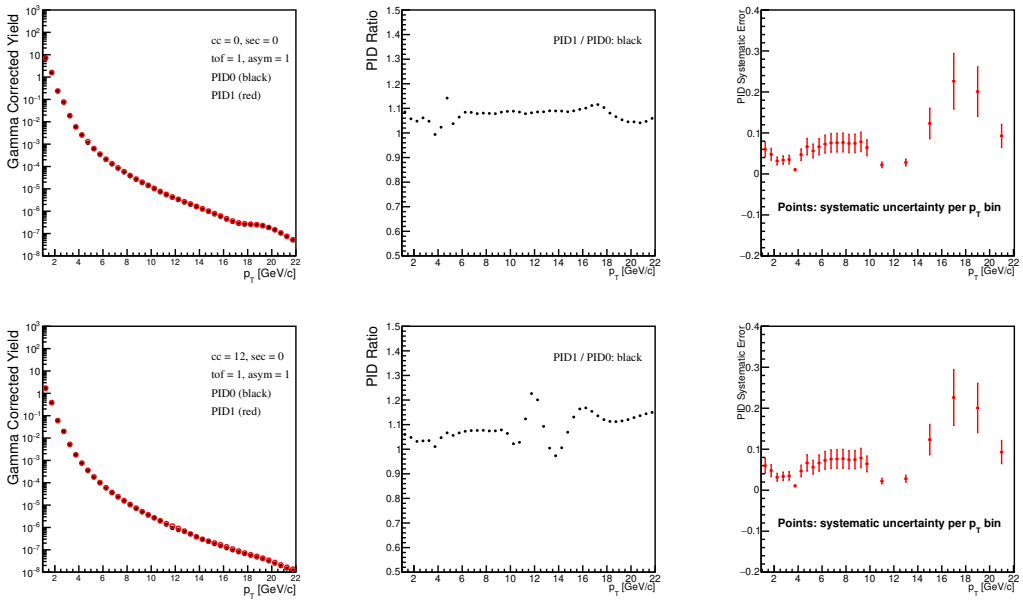

Figure 4.34: PID cut impact on direct photon spectra for cc=0 and cc=MB ASYM1 TOF1 (PbSc).

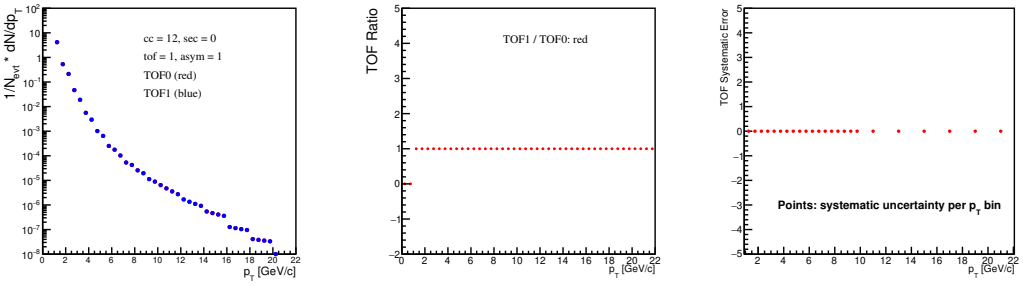

(a) TOF cut effect on corrected π^0 spectra with asymmetry=1 and PID=1 for cc=MB (PbSc).

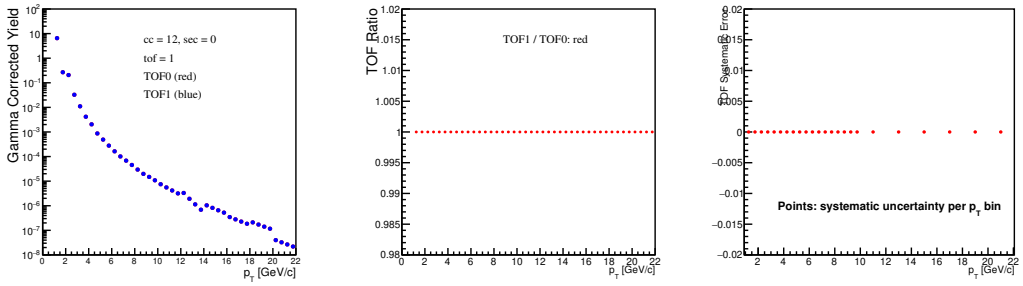

Figure 4.35: TOF cut impact on direct photon spectra for cc=MB (PbSc).

4.10 Heavy Ion Collision Results

The fully corrected π^0 and direct photon invariant yields are presented for various centrality bins, PID, and TOF cuts. It is obtained through a series of steps involving simulation and data correction:

1. **Simulation**: Generate π^0 particles and their decay photons, simulating their interactions with the detector to account for acceptance, efficiency, and smearing effects.

2. **Embedding**: Suppose simulated single-particle events onto real collision events to study detector response in a realistic environment.

3. **Response Matrix**: Construct a 2D matrix mapping the true transverse momentum (P_t) to the measured P_t using high-statistics simulated data.

4. **Unfolding**: Apply an iterative procedure to correct the raw π^0 yield by comparing the measured spectra with the trial function spectra, adjusting the trial function until convergence is achieved.

4.10.1 Raw π^0 Centrality Ratio for PbSc & PbGl

The raw yield ratios of π^0 mesons for various centrality classes are analyzed separately for the PbSc and PbGl (See figure 4.36). These ratios highlight differences in detector response and acceptance between the two subsystems.The PbSc data have steady patterns across all centrality bins, but the PbGl data have affects that are more specific to each bin. This comparison shows that the raw yield extraction is stable before any other changes are made.

4.10.2 Raw π^0 Run14 & Run16

We present a direct comparison of raw π^0 yields between Run14 and Run16 datasets (See figure 4.37). The ratio provides insight into the consistency of detector performance and data quality over different data-taking periods. Minor deviations are observed and attributed to subtle differences in calibration and run conditions. This comparison serves as a validation step before applying correction factors.

4.10.3 Corrected π^0 Invariant Yield (PPG080/Run14)

After applying acceptance, efficiency, and background subtraction corrections, we compare the corrected π^0 invariant yield with published results from PPG080 (See figure 4.38). The ratio demonstrates excellent agreement within systematic uncertainties, confirming the accuracy of our correction procedures and validating the final extracted physics observables.

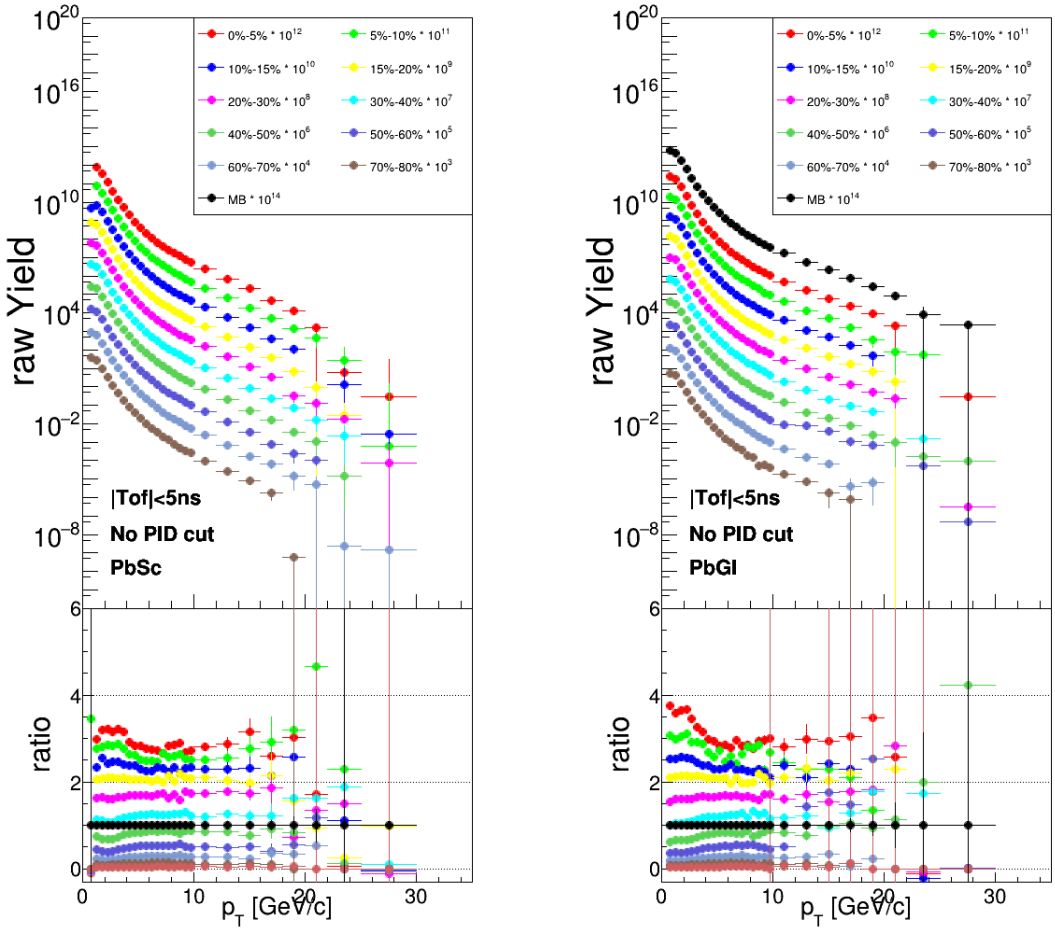

Figure 4.36: Centrality binned raw π^0 spectrum from combined MB and ERT dataset (upper panel), ratio for each centrality with MB (0-92%)(lower panel). Cuts pid=0, tof=0. PbSc (left panel) PbGl (right panel).

4.10.4 Inclusive γ (Run14 & Run16)

Since the same thing is being measured for Run14 and Run16, the results must be consistent every time. We do the studies for both runs because an extensive amount of 200 GeV Au+Au data were collected in 2014, which is a lot more than the statistics of all the similar data that was collected, but then Run16 is again huge statistics, comparable to Run14 (See figure 4.39).

Ultimately we want to add the two measurements, Run14 and Run16 - but first we have to make sure their results are consistent (otherwise at least one of the measurements must be wrong). Because of this, the systematic uncertainties can be reduced, and the range of transverse momentum readings for neutral pions and photons gets wider.

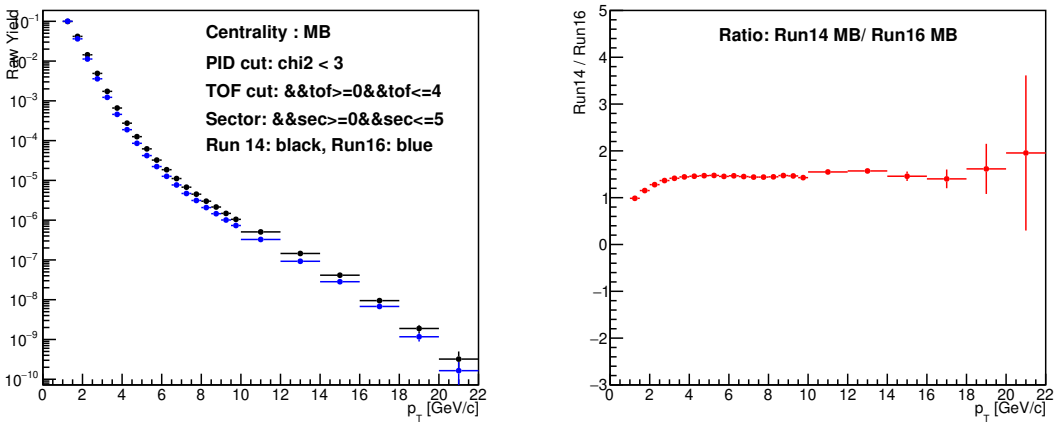

Figure 4.37: Comparison of Run 14 and Run 16 raw π^0 yield and their ratio

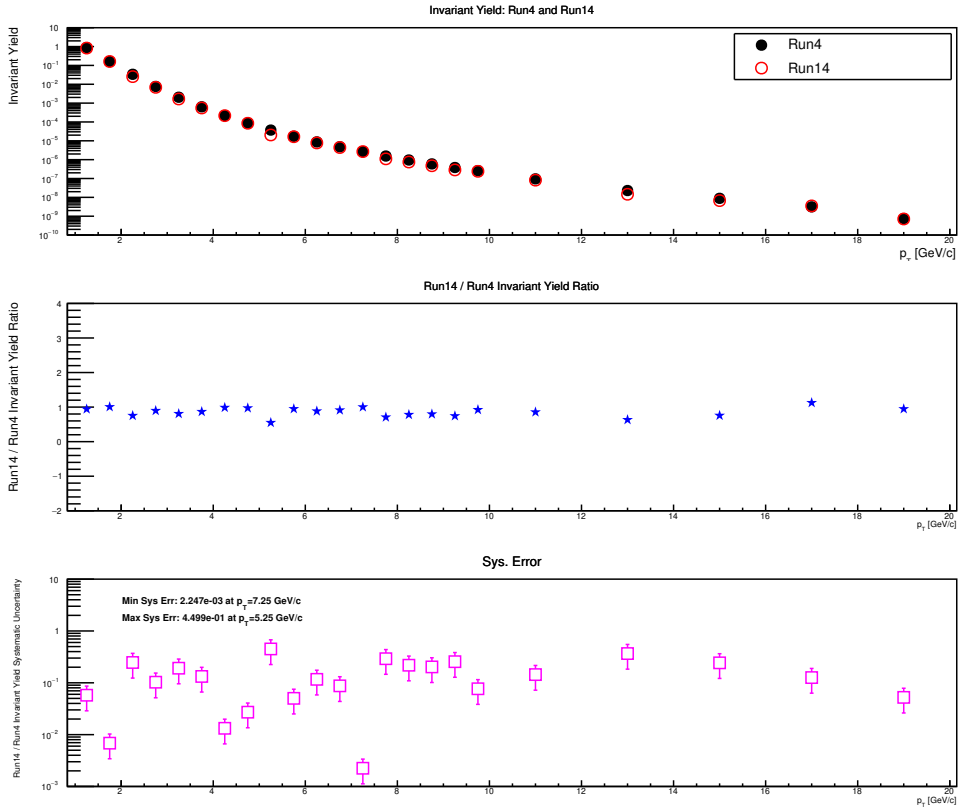

Figure 4.38: Ratio of run 14 over run 4 for cc=0 on the left and cc=MB on the right. The first panel shows run 14, the second panel shows run 4, and the third panel shows the ratio. This was done using the code `Yield_inv.py` and `PionpT_Run4_14.C` (Section 3.4).

4.10.5 Inclusive γ over Decay γ

The ratio of inclusive photons (γ_{incl}) to decay photons (γ_{decay}) is an important quantity in high-energy physics experiments. Inclusive photons include all photons produced in the collision from various sources such as direct-photon production,

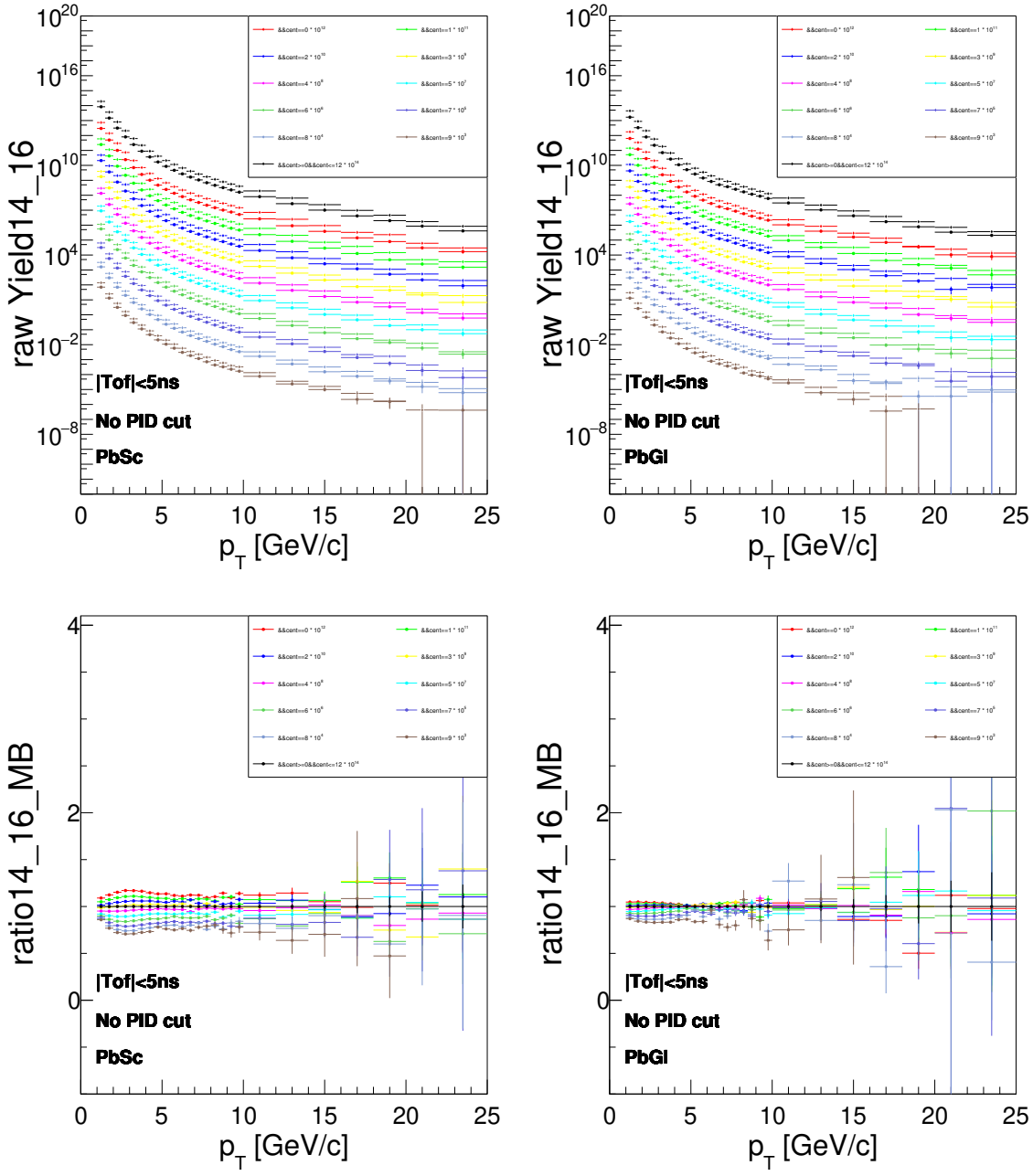

Figure 4.39: Raw inclusive photon spectra after merging MB & ERT for Run14 and Run16 for different centrality classes. The left panels show spectra for PbSc and the right panels show spectra for PbGl. Additionally, the ratio of Run14 to Run16 spectra is presented: left panels for PbSc and right panels for PbGl.

decays of hadrons (like π^0), and other processes. Decay photons, on the other hand, specifically refer to photons originating from the decay of hadrons, such as π^0. To make it clear, here the inclusive and decay photons are raw (See figure 4.40). This ratio helps to understand the contribution of direct photons (photons not originating from hadron decays) to the inclusive spectrum.

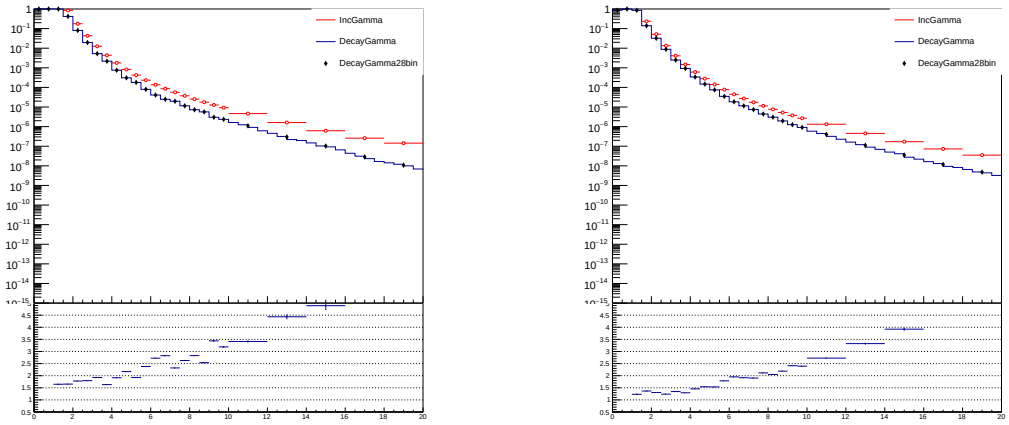

Figure 4.40: Ratio inclusive gammas over decay Gammas from Corrected π^0 for cc=0 on the left and cc=MB on the right with PID=1, tof=0 for PbSc.

4.10.6 Corrected Invariant Yields: Direct γ (ppg139/Run14)

This part focuses on the process of reconstructing the direct photon invariant yield. Firstly, the initial photon yields that include all photons are modified to correct for the existence of hadrons, namely π^0 in our scenario. Afterwards, the contributions from all raw decay photons are eliminated, resulting in just the raw direct-photon yield standing for correction. The corrected direct photon invariant yields are shown in figures 4.41.

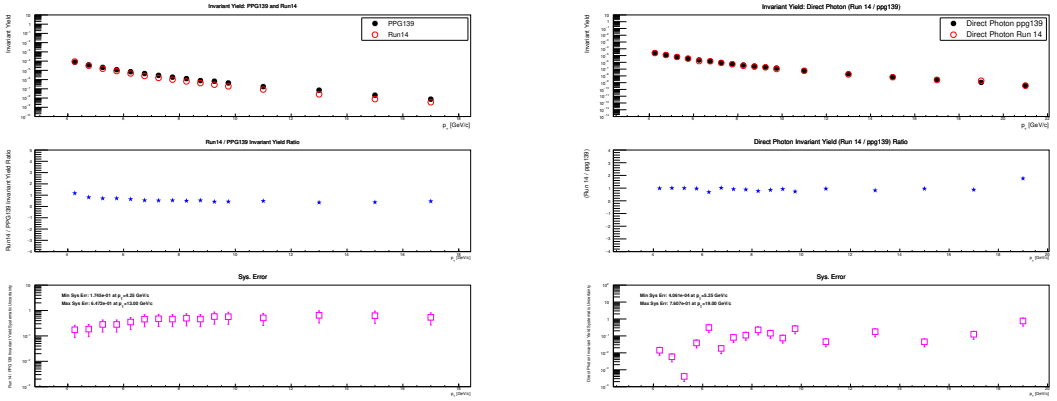

Figure 4.41: Corrected direct photon invariant yields for cc=1 (left) and cc=MB (right) with PID=1 and TOF=0 for PbSc (ppg139/Run14).

4.11 Direct Photon to π^0 Corrected Yields Ratio

At the outset, I investigated the centrality dependency of direct photon and π^0 generation in d+Au collisions dAuCentrality2025. The study introduced a completely

experimental approach for calculating the number of binary nucleon–nucleon collisions (N_{coll}) using high-p_T direct photons, eliminating Glauber model calculations. This technique relies on the assumption that the nuclear modification factor for direct photons, R_γ, is equal to unity across all centralities 4.7:

$$R_\gamma(p_T) = \frac{Y_\gamma^{\text{AuAu}}(p_T)}{N_{\text{coll}} \times Y_\gamma^{pp}(p_T)} \approx 1, \tag{4.7}$$

This indicates that photons are unaffected by the medium. Assuming that the ratio of direct photon to π^0 yields in heavy-ion collisions is directly connected to the nuclear modification factor in $Au + Au$ and $d + Au$.

$$\frac{Y_\gamma^{\text{AuAu}}(p_T)}{Y_{\pi^0}^{\text{AuAu}}(p_T)} \Big/ \frac{Y_\gamma^{pp}(p_T)}{Y_{\pi^0}^{pp}(p_T)} = \frac{R_\gamma(p_T)}{R_{\pi^0}(p_T)}. \tag{4.8}$$

If $R_\gamma(p_T) \approx 1$, the double ratio on the left-hand side becomes approximately $1/R_{\pi^0}(p_T)$. This quantity therefore encodes the same information as R_{π^0} but does not require any Glauber-model input for N_{coll}.

Figure 4.42 present these Yields for π^0 and direct photon for multiple centralities and the ratio between them. At high p_T, the ratio rises above unity, consistent with the suppression of π^0 production in Au+Au collisions. This behavior mirrors the underlying principle used in the d+Au analysis: direct photons serve as a model-independent experimental scaler for binary collisions. Thus, our Au+Au measurement provides an important *data-driven validation* of the central assumption in the d+Au paper, now tested in a large-system environment.

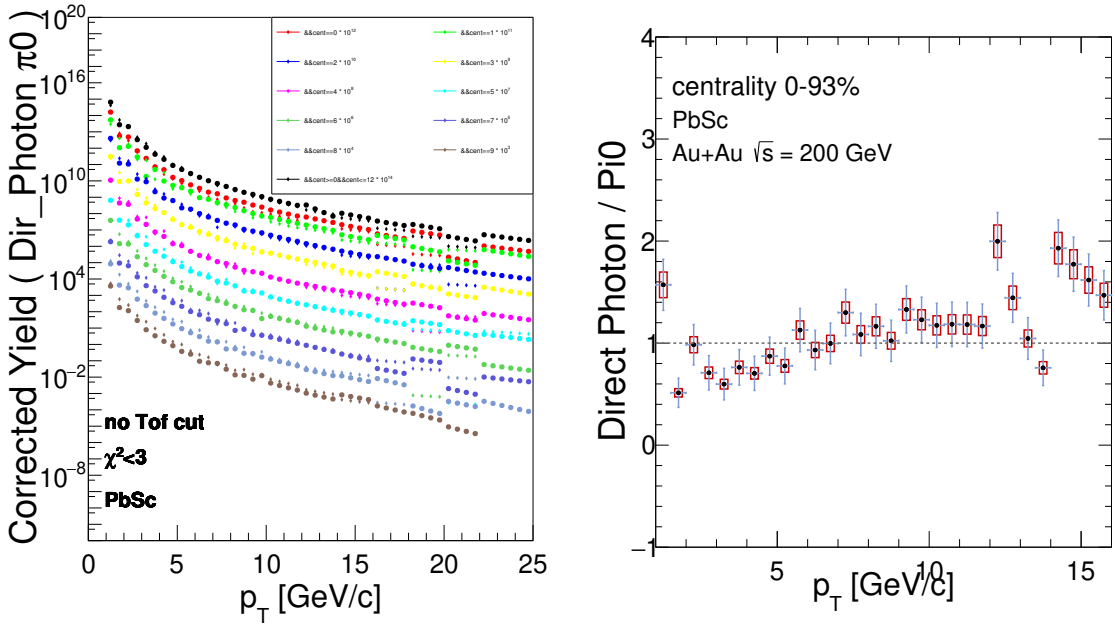

Figure 4.42: Fully corrected invariant yields for direct photons and π^0 in different cc (PID=1, TOF=1, PbSc) on the left and the ratio between them on the right.

CHAPTER 5

OUTLOOK

5.1 Conclusion For Heavy Ion Collision

The higher statistics data set of Run-14 Au+Au collisions at 200 GeV at the PHENIX experiment was examined in this work. The Dead/hot map was created by eliminating any malfunctioning towers to minimize bias, and the dead/hot towers were then included in the analysis. The timing was carefully calibrated. A calibration process resulted in an average resolution of 0.6 nanoseconds. I used the calorimeter technique to reconstruct the π^0. The raw yield of π^0 is corrected by a 2-D matrix generated from a simulation, in which tens of million of π^0's are simulated and propagated thought the simulation package(PISA). Then, a comparison is done between the 2-D matrices of run-14 and run-16.
The corrected yield of different π^0 windows are presented, followed by a comparison of the invariant yield between run-4 and run-14. Decay photons are calculated by a 2-D matrix for $\pi^0 \rightarrow \gamma\gamma$ decay, which is from the same simulation. Then raw direct photon yields were obtained by subtracting decay photons from the inclusive. Eventually, I presented the corrected yield and invariant yield of direct photon by unfolding the raw direct photon using a 2-D response matrix of single photon simulation.
After this, I investigated the systematic uncertainties by varying PID parameters and energy asymmetry cuts for the corrected yield of π^0 and corrected yield of direct γ and several comparisons conducted to prove the consistency between my findings and another PHENIX result.

5.2 Publications as First Author

- Nour Jalal Abdulameer, Stefan Oniga, Balazs Ujvari, *Advanced Big Data Solutions for Detector Calibrations for High-Energy Physics*, Electronics **14** (2025) 2088. https://www.mdpi.com/2079-9292/14/10/2088
- Nour Jalal Abdulameer, *Run14 Au+Au Dead and Hot Map*, PHENIX Analysis Note TN-486.0, 2024. https://phenix-intra.sdcc.bnl.gov/WWW/p/draft/nourja/PhD/A_T_NOTE/Run14_AuAu_Dead_Hot_Map.pdf
- Nour Jalal Abdulameer, *Calibration of EMCal ToF in Run-14 Au+Au collisions*, PHENIX Analysis Note TN-489.0, 2024. https://phenix-intra.sdcc.bnl.gov/WWW/p/draft/nourja/PhD/A_T_NOTE/TN_Timing_Run14AuAu.pdf
- Nour Jalal Abdulameer, *Run 14 π^0 and direct photon analysis in 200 GeV Au+Au collisions*, PHENIX AN 1505, 2024. https://phenix-intra.sdcc.bnl.gov/phenix/WWW/p/info/an/1505/ANALYSIS_NOTE-Run14_pi0.pdf
- Nour Jalal Abdulameer, Habeeb Allawi, Balazs Ujvari, *Study of the relationships between flares and coronal mass ejections in high-energy solar particle events during the early stages of Solar Cycle 25*, Int. J. Mod. Phys. A **40** (2025) 2542007. https://www.worldscientific.com/doi/epdf/10.1142/S0217751X25420072
- Nour Jalal Abdulameer, *Centrality Dependence of direct photon and π^0 Production in d+Au Collisions*, Moscow University Physics Bulletin **79** (2025) 7. https://link.springer.com/article/10.3103/S0027134924701133#citeas

5.3 Publications as Co-Author (PHENIX Collaboration)

As per PHENIX's requirements, I have been included as an author in all articles related to this project because of my contributions in the areas of direct photons, DHM, and timing calibration

- Abdulameer, N. J. et al., "Cross sections of η mesons in $p + p$ collisions at forward rapidity at $\sqrt{s} = 500$ GeV and central rapidity at $\sqrt{s} = 510$ GeV," arXiv:2507.04896, 2025.
- Abdulameer, N. J. et al., "Low-mass vector-meson production at forward rapidity in p+p and Au+Au collisions at $\sqrt{s_{NN}} = 200$ GeV," arXiv:2507.04463, 2025.
- Abdulameer, N. J. et al., "Measurement of inclusive jet cross section and substructure in p+p collisions at s=200 GeV," Phys. Rev. D 111, 112008 (2025), DOI: 10.1103/hpm9-qfp6.
- Abdulameer, N. J. et al., "Azimuthal anisotropy of direct photons in Au+Au collisions at $\sqrt{s_{NN}} = 200$ GeV," arXiv:2504.02955, 2025.

- Abdulameer, N. J. et al., "Measurements at forward rapidity of elliptic flow of charged hadrons and open-heavy-flavor muons in Au+Au collisions at $\sqrt{s_{NN}}$ = 200 GeV," arXiv:2409.12715, 2024.
- Abdulameer, N. J. et al., "Measurement of elliptic flow of J/ψ in Au+Au collisions at $\sqrt{s_{NN}}$ = 200 GeV," Phys. Rev. C 112, 014904 (2025), DOI: 10.1103/PhysRevC.112.014904.
- Abdulameer, N. J. et al., "Multiplicity dependent J/ψ and $\psi(2S)$ production at forward and backward rapidity in p+p collisions at $\sqrt{s}$ = 200 GeV," arXiv:2409.03728, 2024.
- Abdulameer, N. J. et al., "Centrality dependence of Lévy-stable two-pion Bose-Einstein correlations in Au+Au collisions at $\sqrt{s_{NN}}$ = 200 GeV," Phys. Rev. C 110, 064909 (2024), DOI: 10.1103/PhysRevC.110.064909.
- Abdulameer, N. J. et al., "Jet modification via π^0-hadron correlations in Au+Au collisions at $\sqrt{s_{NN}}$ = 200 GeV," Phys. Rev. C 110, 044901 (2024), DOI: 10.1103/PhysRevC.110.044901.
- Abdulameer, N. J. et al., "Identified charged-hadron production in various collision systems at RHIC energies," Phys. Rev. C 109, 054910 (2024), DOI: 10.1103/PhysRevC.109.054910.
- Abdulameer, N. J. et al., "Disentangling Centrality Bias and Final-State Effects in High-p_T Neutral Pions Using Direct Photon in d+Au Collisions at $\sqrt{s_{NN}}$ = 200 GeV," Phys. Rev. Lett. 134, 022302 (2025), DOI: 10.1103/PhysRevLett.134.022302.
- Abdulameer, N. J. et al., "Transverse single-spin asymmetry of midrapidity π^0 and η mesons in p+Au and p+Al collisions at $\sqrt{s_{NN}}$ = 200 GeV," Phys. Rev. D 107, 112004 (2023), DOI: 10.1103/PhysRevD.107.112004.
- Abdulameer, N. J. et al., "Transverse single-spin asymmetry of charged hadrons at forward and backward rapidity in polarized p+p, p+Al, and p+Au collisions at $\sqrt{s_{NN}}$ = 200 GeV," Phys. Rev. D 108, 072016 (2023), DOI: 10.1103/PhysRevD.108.072016.
- Abdulameer, N. J. et al., "Highlights from the PHENIX Experiment," Acta Phys. Polon. Supp. 16 (1), 7 (2023), DOI: 10.5506/APhysPolBSupp.16.1-A7.
- Abdulameer, N. J. et al., "Measurement of ϕ-meson production in Cu+Au and U+U collisions at RHIC," Phys. Rev. C 107, 014907 (2023), DOI: 10.1103/PhysRevC.107.014907.

5.4 Project Presentations and Posters

- Presentation: N.J. Abdulameer (Debrecen U.) Analysis of $pi0$ & direct γ in the large 2014 200 GeV Au+Au/PHENIX dataset. https://indico.cern.ch/event

/1352455/contributions/5696686/attachments/2767195/4820343/Zimanyi 2023last%20(3).pdf.

- Poster: N.J. Abdulameer (Debrecen U.) Run14 Au+Au DHM calibration of EMCal at 200 GeV. http://zimanyischool.kfki.hu/22/participants
- Presentation: N.J. Abdulameer (Debrecen U.) Centrality Dependence of dirγ and $pi0$ Production in d+Au Collisions. https://lomcon.ru/?page_id=1156.
- Poster: N.J. Abdulameer (Debrecen U.) Neutral probes in PHENIX from the large 2014 200 GeV Au+Au dataset. https://indico.cern.ch/event/1043736 /contributions/5363946/
- Poster: N.J. Abdulameer (Debrecen U.) Precision Measurement of Direct Photon Production in 200 GeV Au+Au Collisions Using the PHENIX Run-14 Dataset.
  https://indico.cern.ch/event/1479384/abstracts/193298/
- Presentation: N.J. Abdulameer (Debrecen U.) Direct Photon Measurements in Au+Au Collisions at $\sqrt{s_{NN}}$ = 200 GeV.
  https://zimanyischool.kfki.hu/25/registration

CHAPTER 6

SOLAR CYCLE 25

6.1 SEPs and Flare CMEs Relationships

This research investigates the interaction between high-energy solar particle events (SEPs), solar flares, and coronal mass ejections (CMEs) at the beginning of Solar Cycle 25. This study explores the origins and attributes of solar energetic particles (SEPs), scrutinizes the behavior of solar flares and coronal mass ejections (CMEs), and studies their interconnections via the use of sophisticated observational methods. The study highlights the range of correlations between SEP-CMEs, which are influenced by intricate magnetic interactions and propagation circumstances. These factors are essential to improve the accuracy of space weather predictions.

Additionally, the research includes an in-depth investigation of high-energy photon production in these astrophysical phenomena. Photons, especially in X-ray and gamma-ray bands, serve as direct, minimally interacting messengers that carry vital information about the early stages and extreme conditions of solar events. By studying photon emissions alongside SEPs and CMEs, the research enhances the understanding of particle acceleration and energy release mechanisms in the solar atmosphere.

Examining prior solar cycles allows us to gain understanding about the changing patterns of solar activity. This emphasizes the need of making more progress in developing predictive models and forecasts to enhance Earth's ability to withstand space weather events.

6.2 Flare and CME Overview

Solar flares and coronal mass ejections (CMEs) are important solar phenomena that have the potential to affect space weather. Flares are powerful emissions of radiation caused by the release of magnetic energy stored in the Sun's atmosphere, whereas CMEs result from the expulsion of large amounts of solar plasma and magnetic fields into space. These occurrences have the ability to propel particles to elevated levels of energy, resulting in solar energetic particle (SEP) incidents

that may impact Earth's magnetosphere and ionosphere (see Fig. 6.1).

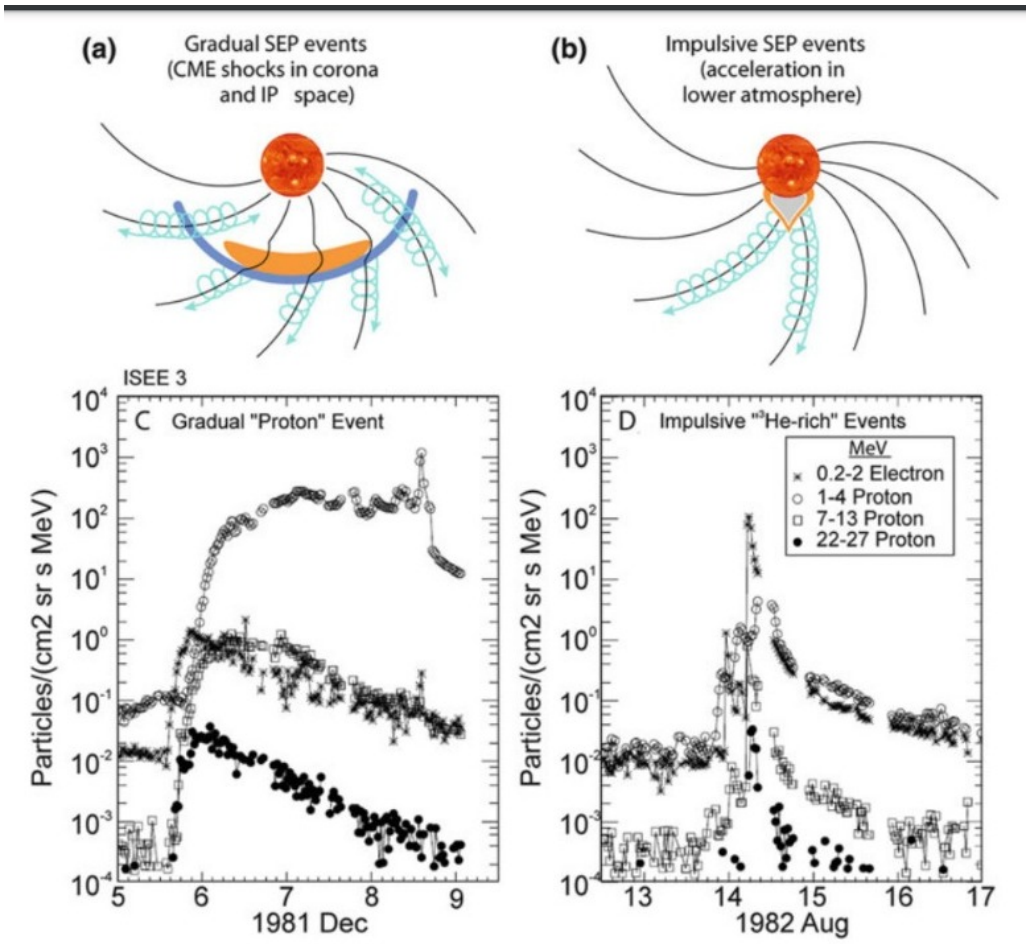

Figure 6.1: SEP events may be classified into two categories: (a) Gradual events, which are widely dispersed due to diffusive acceleration during shocks caused by coronal mass ejections (CMEs). (b) Abrupt occurrences, notably associated with solar flares. When comparing progressive versus impulsive SEP episodes, we may see clear differences in the intensity-time patterns. Gradual events refer to coronal mass ejections (CMEs) that occur without abrupt flares, while sudden events are caused by series of flares without CMEs (Adapted from Desai and Giacalone 2016, with permission from Springer) [92].

These contributions support the statistical relationships between SEP features and eruptive solar activity. These links include CME speeds and electromagnetic fingerprints in the solar atmosphere [14].

The magnetic structure determines the active-region class and the size and shape of sunspot groups. Significant space weather, such as solar flares and CMEs, can result from large and complex sunspots in active regions [93].

Dynamic processes such as plasma heating, solar flares, and CMEs are seen in active zones. Solar flares are divided into A-, B-, C-, M-, and X-classes by the brightness of their X-ray flux. This is based on the burst of electromagnetic emissions that happen across a range of wavelengths when the Sun's magnetic field reconnects (see Fig. 6.2) [94]).

Several flares, coming from Active Region 12882, including X-, M-, and C-class

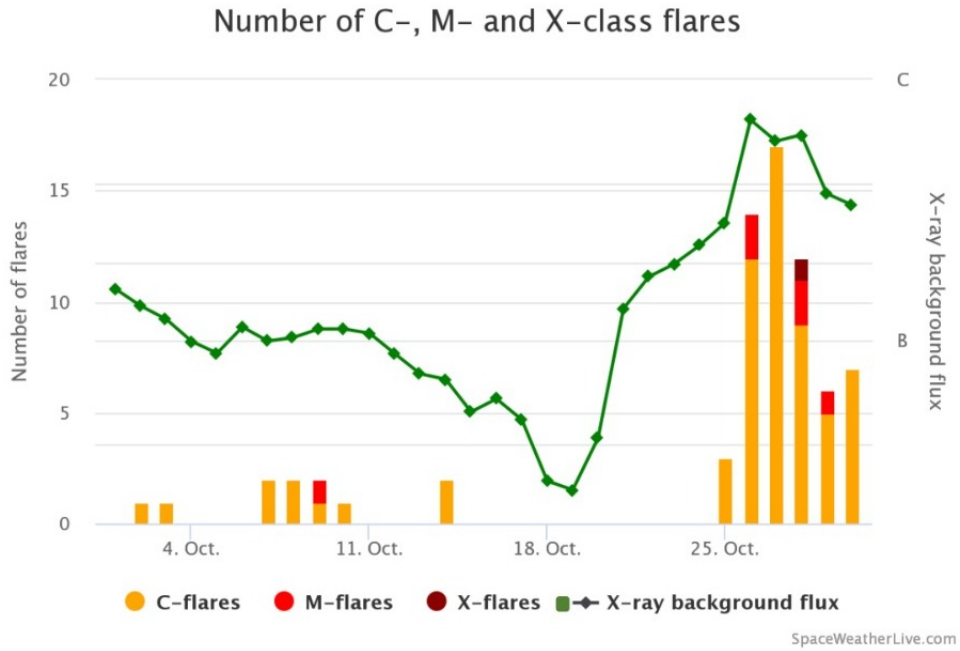

Figure 6.2: The number of classes on solar flares in October 2021.

flares, were observed in October 2021. A high Kp index due to associated CMEs caused a G2 geomagnetic storm.

6.3 Observational and Analytical Techniques

6.3.1 Photon Emission in High-Energy Solar Particle Events

High-energy solar particle events (SPEs) involve charged particles accelerated and expelled from the Sun, often associated with solar flares and shocks from coronal mass ejections (CMEs). Alongside these particles, intense photon emissions occur across the electromagnetic spectrum, providing critical insights into the underlying acceleration mechanisms [95].

Impulsive SEP events, linked with short-duration soft X-ray bursts and fast-drift type III radio emissions, produce characteristic photon signatures indicative of flare-driven acceleration. These events are often enriched with ^{3}He and heavy ions, and their photon emissions help trace the rapid energy release during solar flares.

In contrast, gradual SEP events, associated with type II radio emissions, originate from CME-driven shocks in the solar corona [96]. Photon observations in these events, including X-rays and gamma rays, reveal details of shock acceleration processes and particle interactions in the solar atmosphere [97].

Hybrid events, exhibiting features of both impulsive and gradual types, further complicate photon emission patterns and demand comprehensive multi-wavelength studies [97].

Understanding high-energy photon emissions during intense SEP events, especially those causing ground-level enhancements (GLEs) detectable by neutron monitors, is essential [98]. The temporal and spectral characteristics of these photons provide clues to particle origin, acceleration efficiency, and transport effects relevant to space weather hazards [99].

Photon monitoring is particularly crucial for space weather forecasting because high-energy photons can precede energetic particles, allowing early warning of potentially damaging solar events. Additionally, photon-induced ionization in Earth's upper atmosphere affects satellite communications and navigation systems, emphasizing the practical importance of photon studies in solar-terrestrial physics [100].

6.3.2 Solar flares study

Solar flares are examined by observing X-ray emissions via the use of satellites such as the Geostationary Operational Environmental Satellite (GOES). These satellites provide instantaneous information on the strength, duration, and categorization (A, B, C, M, X-classes) of solar flares, determined by the highest level of X-ray radiation [93] (see fig. 6.1).

6.3.3 CMEs Study

Coronal Mass Ejections (CMEs) are examined via the use of corona graphs, which are installed aboard spacecraft such as the Solar and Heliospheric Observatory (SOHO) and the Solar Dynamics Observatory (SDO). These sensors record photos of the Sun's corona, enabling us to monitor the velocity, trajectory, and magnitude of CMEs. Linear speed, angular width, and position angle (PA) are important factors for comprehending the dynamics and possible consequences of CMEs [14] (see fig. 6.1).

6.3.4 Select Dates Measurements

CME Speed, Photon Energy, and Energy Flux Analysis:

Figure 6.3 presents three graphs showing the relationship between photon energy flux and the velocity of a Coronal Mass Ejection (CME) at different photon energy densities. Each graph uses colored data points with an overlaid regression line to illustrate the trend.

- **Blue (Energy density = 10):** This graph shows a weak positive correlation between CME speed and photon energy flux. As the CME velocity increases, the photon energy flux rises slightly, but the effect is modest.

- **Green (Energy density = 50):** At this intermediate photon energy density, the positive correlation strengthens. Higher CME speeds correspond to a more noticeable increase in photon energy flux.

- **Red (Energy density = 100):** Here, the correlation is strongest. The photon energy flux increases significantly with rising CME velocity, indicating that faster CMEs produce a substantially higher photon energy output at this energy level.

Summary: The color-coded graphs demonstrate that the connection between CME velocity and photon energy flux grows stronger with increasing photon energy density. Across all cases, a clear upward trend is observed, indicating that faster CMEs tend to generate higher photon energy fluxes. This relationship provides insight into how CME dynamics influence photon emissions during solar energetic events.

Energy Density	Correlation Strength	Slope of Regression	Notes
10	Weak	Small positive	Modest increase in flux with CME speed
50	Moderate	Clear positive	More noticeable flux increase
100	Strong	Steep positive	Significant flux increase

Table 6.1: Summary of correlation between CME velocity and photon energy flux at different photon energy densities.

6.3.5 Photon Flux at Various Energy Levels Compared

Table 6.2 presents photon flux measurements for selected dates at energy thresholds of > 10 MeV, > 50 MeV, and > 100 MeV, with a constant angular width of 360°. For instance, on 2021/11/03, the photon flux is notably high (5, 0.5, and 0.1 cm^{-2} s^{-1} sr^{-1} respectively), indicating increased solar photon activity. Conversely, on 2022/01/12, flux values are significantly lower (0.1, 0.01, and 0.01 cm^{-2} s^{-1} sr^{-1}), reflecting reduced photon emissions.

In both cases, photon flux decreases as energy increases, consistent with the expected spectral behavior of solar energetic photon emissions.

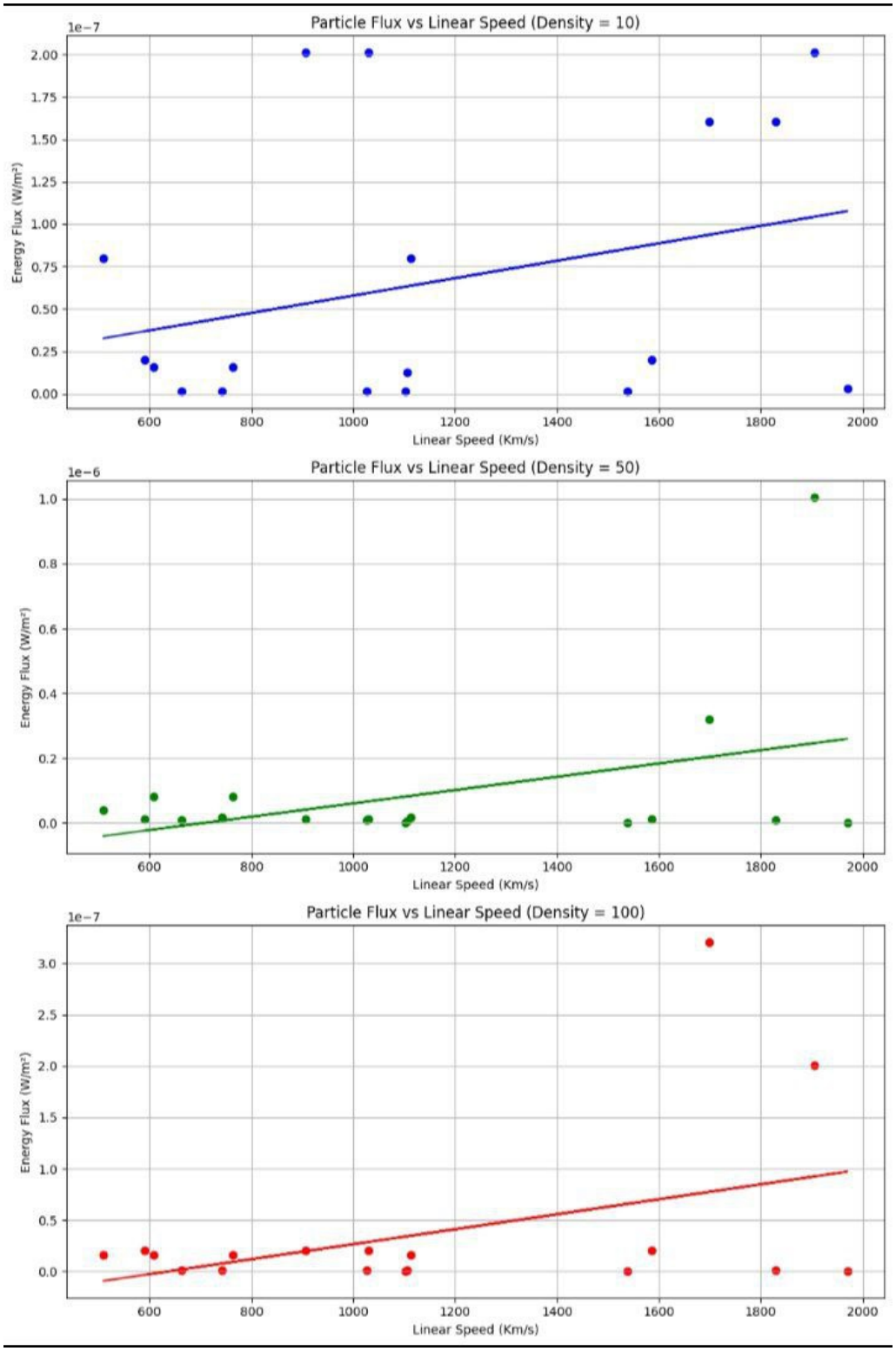

Figure 6.3: Photon energy flux vs. CME velocity for three photon energy densities: 10 (blue), 50 (green), and 100 (red). Regression lines indicate the trend for each dataset.

Table 6.2: Photon Flux Data with Angular Width and Particle Energy Levels

#	Date	A-W	P-E(MeV)	P-F(cm^{-2} s^{-1} sr^{-1})
1	2021/11/03	360°	>10	5
			>50	0.5
			>100	0.1
2	2022/01/12	360°	>10	0.1
			>50	0.01
			>100	0.01
3	2022/02/15	360°	>10	1
			>50	1
			>100	0.1
4	2022/03/10	360°	>10	1
			>50	0.1
			>100	0.1
5	2022/03/30	360°	>10	10
			>50	1
			>100	0.1
6	2022/05/21	360°	>10	1
			>50	0.9
			>100	0.1
7	2022/07/23	360°	>10	1
			>50	0.9
			>100	0.1
8	2022/07/30	360°	>10	10
			>50	1
			>100	0.1
9	2022/12/12	360°	>10	0.1
			>50	0.01
			>100	0.01
10	2023/01/18	360°	>10	0.8
			>50	0.1
			>100	0.01
11	2023/03/09	360°	>10	0.9
			>50	0.1
			>100	0.01
12	2023/03/13	360°	>10	10
			>50	4
			>100	2
13	2023/06/20	360°	>10	0.5
			>50	0.1
			>100	0.2
14	2023/07/16	360°	>10	10
			>50	0.3
			>100	0.1

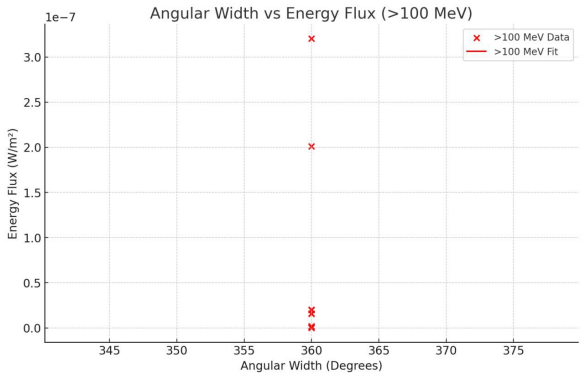

(a) a

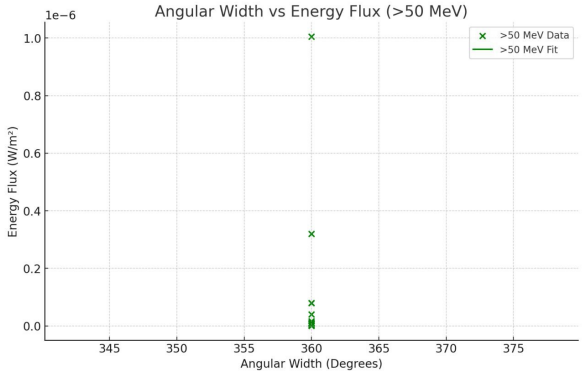

(b) b

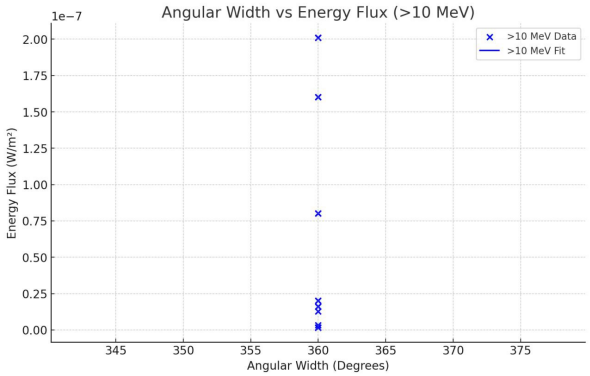

(c) c

Figure 6.4: Correlation between angular width and energy flow at various energy levels: (a) Over 100 MeV, (b) Greater than 50 MeV, and (c) Over 10 MeV. Data points cluster within a 360° angle, with energy flux ranging from 0 to 3×10^{-7} W/m². Linear regressions (red, green, and blue lines) show a weak correlation, indicating limited variability and clustering. Alternative methods or data with more variability may improve results.

Figures 6.4a, 6.4b, and 6.4c illustrate the relationship between angular width and photon energy flux at energy thresholds above 100 MeV, 50 MeV, and 10 MeV, respectively.

Data Analysis: In all three cases, the angular width data points are concentrated within a 360° range, and the photon energy flux varies within limited ranges (up to 3×10^{-7} W/m^2 for 50 and 100 MeV, and 2×10^{-7} W/m^2 for 10 MeV). There are no significant outliers, indicating photon flux is fairly stable across these angular widths.

Regression Analysis: The colored lines represent linear regressions between angular width and photon energy flux for each energy range. However, the correlation is weak and statistically insignificant in all cases, likely due to the small variability in angular width and the clustering of data points near similar values.

Explanation: The limited spread in angular widths reduces the explanatory power of linear models, resulting in poor regression fits. To improve analysis, alternative methods or datasets with greater angular variability are recommended to better capture the relationship between photon flux and angular distribution.

6.4 Findings

On May 7, 2023, it has been detected an M1.44 solar flare, which was followed by a coronal mass ejection (CME) traveling at a linear speed of 1075 km/s (Fig. 6.5). As a result of this event, there were geomagnetic storms, characterized by a peak solar wind speed of 553 km/s and a total IMF of 19 nT. The electron flux in geosynchronous orbit reached its highest point at 142 pfu.

6.5 Observation and Final Remarks

6.5.1 Solar Events Variation

The observed occurrences illustrate the diversity in the attributes of solar flares and CMEs, including variations in magnitude, velocity, and geomagnetic influence. The research emphasizes the intricate correlation between solar flares and coronal mass ejections (CMEs) and their collective impact on solar energetic particle (SEP) occurrences.

6.5.2 The Impact on Space Weather

Gaining a comprehensive understanding of the mechanisms behind flares and coronal mass ejections (CMEs) is essential to improve the accuracy of forecast models for space weather. These occurrences may have a substantial effect on the functioning of satellites, communication networks, and electrical grids on Earth. Advanced observational techniques and analytical procedures are required to accurately forecast and minimize the negative consequences of solar activity.

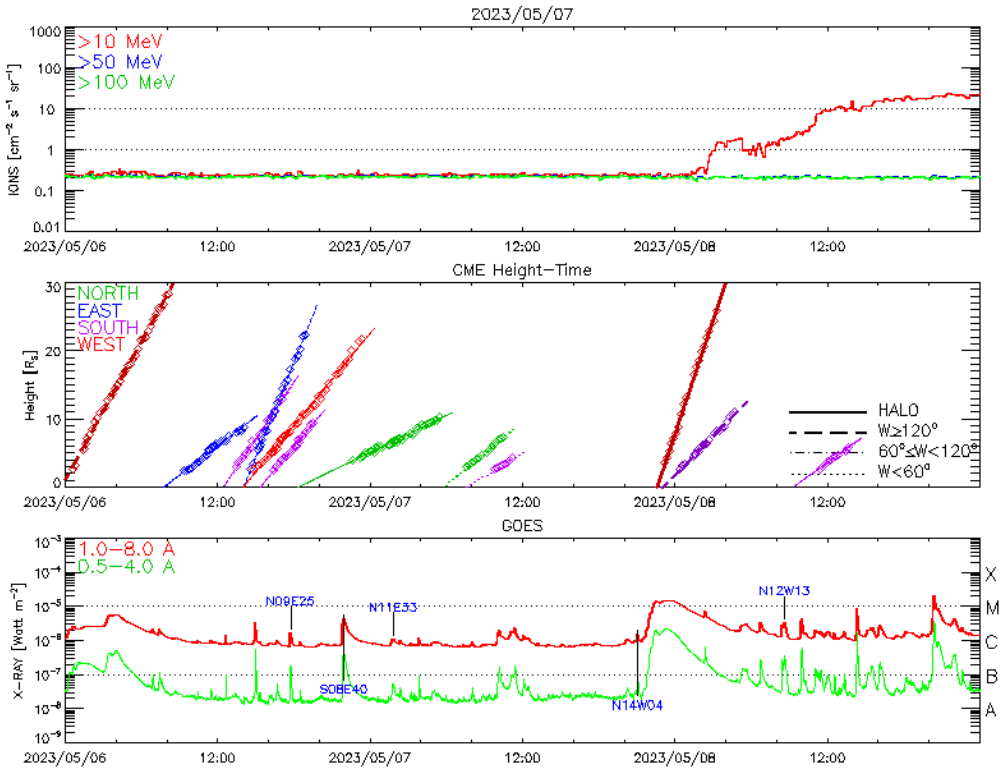

Figure 6.5: The features of the CME on May 7, 2023 are as follows: A Halo Coronal Mass Ejection (CME) occurred, with an angular diameter of 360 degrees and a linear speed of 1075 km/s. This CME resulted in notable geomagnetic disruptions.

6.6 Conclusion

In conclusion, the early phase of Solar Cycle 25 shows both familiar and novel features compared to previous cycles. While the intensity and frequency of high-energy solar events remain moderate, improvements in photon detection and measurement technologies enhance our ability to monitor solar photon emissions and their effects on space weather. Historical data on photon fluxes during past cycles reveal fluctuating solar activity levels, highlighting the complex dynamics of photon production in solar events. Insights gained from previous cycles have improved our understanding of photon-related phenomena and their impact on Earth's environment and technologies. Ongoing research focusing on photon observations is vital for advancing predictive models and developing effective mitigation strategies against space weather disturbances. Solar Cycle 25 thus offers a valuable opportunity to refine our knowledge of solar photon behavior and to strengthen Earth's resilience to solar photon-driven space weather effects.

A Summary of the Dissertation

This dissertation has focused on the study of the transverse momentum (p_T) spectra of neutral pions (π^0) and direct photons at mid-rapidity, using high-statistics data from the 2014 RHIC Run. This investigation, unlike previous studies that mostly used next-to-leading order perturbative QCD (NLO pQCD) computations, is based on directly determined standards, enabling a more direct and model-independent examination of medium-induced effects. The study extends to low-p_T direct photon generation, a region that presents experimental challenges due to significant backgrounds from hadronic decays. Isolating a thermal photon component in this area is particularly significant, since these photons are anticipated to be released from a locally thermalized material.

This study offers a larger conceptual connection between photon generation in high-energy nuclear collisions and in astronomical contexts, including solar flares and coronal mass ejections (CMEs). Despite the substantial differences in conditions—one taking place in ultra-relativistic collisions inside a laboratory, the other in the magnetized plasma of the Sun—both systems use high-energy photons as crucial probes of extreme physical states. In heavy-ion collisions, direct photons reflect the initial circumstances and early dynamics of the quark-gluon plasma (QGP). In solar flares and coronal mass ejections, high-energy photons, such as X-rays and gamma rays, indicate particle acceleration mechanisms, magnetic reconnection, and extensive energy release in the solar corona.

The study of solar photon generation has gained significance due to its consequences for space weather. Solar energetic particle (SEP) occurrences, often linked to coronal mass ejections (CMEs) and solar flares, may negatively impact satellite operations, interfere with communication networks, and risk the integrity of power grids. Recognizing the circumstances that lead to the generation of high-energy photons in these situations is crucial for enhancing prediction models and formulating appropriate mitigation strategies.

This thesis highlights the prevalent significance of high-energy photons as indicators of the earliest and most extreme stages of energetic matter by analyzing photon generation processes in nuclear and astrophysical settings. This multifaceted viewpoint indicates how methodologies and insights from heavy-ion experiments can enhance astrophysical research, while simultaneously, how space physics can motivate innovative strategies in nuclear studies, confirming the pivotal role photons play in deepening the understanding of the most energetic phenomena in the universe.

Experimental Methods

The analysis was carried out with the PHENIX detector, particularly the Electromagnetic Calorimeter (EMCal), which provides excellent energy resolution and segmentation for photon measurements. The following key methodological developments were achieved:

- **Dead/Hot Map (DHM)**: In order to reduce false hits, I create the Dead/Hot map by removing the malfunctioning (dead) towers or towers with too many false hits (hot, extra hot). First, I studied the multiplicity of the cluster in every run (order of 1000 runs are available for Run14), in 39 energy bins in order to calculate unique cuts. I extended the dead and hot towers per run and per energy bin by statistical methods to a global dead-hot map I used for the Run14 data set. I studied different dead-hot maps to achieve the best possible data quality for my direct photon analysis.

- **Timing Calibration**: At PHENIX calibration, in my Au-Au 200 GeV data set I developed a new fit for each tower to ensure precise timing for clusters. With this new ToF informations the gamma and the hadron clusters can be distinguished, the hadron backgrounds from direct photon analysis can be subtracted. I successfully implemented the PID cuts (abs(corrected ToF smaller than 5 ns) to remove effectively the contamination from hadrons to have more accurate photon identification.

- **Yield Extraction & Simulation**: I analyzed the neutral pions (π^0s) as the main origin of decay photons. The method of invariant mass reconstruction is used to identify and isolateπ^0 particles. I obtained the raw output of π^0 particles and then applied corrections to the raw output. To modify the raw output, I use a two-dimensional response matrix that I create using π^0 simulations. I confirmed the π^0 yield based on the results of the research and recorded it in the internal review conducted by the PHENIX collaboration. The systematic uncertainty were calculated for the π^0 spectrum, the raw direct photon spectrum was calculated. I performed a simulation of π^0 in order to account for detector effects such as acceptance, efficiency, and smearing. Then I used PISA to simulate the decay and interactions by generating and processing input events. I incorporated simulated energy deposits into actual events to compensate for distortions. I build a two-dimensional response matrix to provide a mapping between the produced Pt and the measured Pt. Corrections were applied through simulation-driven unfolding methods.

- **Solar Particle Events**:I do an analysis of the high-energy solar particle events (SEPs), flares, and coronal mass ejections (CMEs) showing the relationship between photon energy flux and the velocity of a Coronal Mass Ejection (CME) at different photon energy densities during Solar Cycle 25, focused on photon emission related to solar events across different energy ranges. My research analyzed correlations between CME velocity, angular width, and photon energy flux by investigating the origins, processes, and effects

of these events on space weather highlighted the importance of photon monitoring in forecasting. Emphasized the need for improved predictive models for solar-terrestrial interactions.

Main Results

The analysis produced corrected spectra for both π^0 and direct photons across a wide p_T range and for different centrality classes:

- π^0 mesons exhibit strong suppression in central collisions relative to binary-scaled p+p results, consistent with significant partonic energy loss in the QGP.
- Direct photons show no such suppression, confirming their role as unmodified probes of the initial hard scattering processes.
- The ratio of direct photon to π^0 yields was investigated systematically. This ratio provides an alternative, model-independent confirmation of nuclear modification effects, directly connecting Au+Au results to p+p references without explicit reliance on Glauber-based N_{coll} calculations.
- Furthermore, the connection to earlier PHENIX studies in small systems (d+Au collisions) was established. There, direct photons were used experimentally to determine N_{coll}, based on the assumption that $R_\gamma \approx 1$. The present Au+Au analysis provides an independent validation of this assumption, thereby strengthening the foundation of the centrality determination method in small systems.
- In addition to heavy-ion physics, this thesis draws an interdisciplinary connection to solar physics. High-energy photons, produced during solar flares and coronal mass ejections, serve as probes of magnetic reconnection and particle acceleration in the solar atmosphere. Just as in heavy-ion collisions, photons provide a direct, penetrating view of extreme physical environments. The parallel highlights the universal role of photons as messengers of early-time dynamics, whether in the QGP created in the laboratory or in natural astrophysical plasmas.

Overall, this work advances the understanding of photon production in heavy-ion collisions and its implications for both nuclear and astrophysical physics. It demonstrates that photons, across contexts, remain among the most reliable probes of the earliest and most extreme conditions in nature.

REFERENCES LIST:

[1] Daniel Neuhauser. "Photon interferometry for heavy ion collisions". In: Phys. Lett. B 182.3-4 (1986), pp. 289–292. DOI: 10.1016/0370-2693(86)90092-4.

[2] Edward V. Shuryak. "Quantum Chromodynamics and the Theory of Superdense Matter". In: Phys. Rept. 61 (1980), pp. 71–158. DOI: 10.1016/0370-1573(80)90105-2.

[3] Miklos Gyulassy and Michael Plumer. "Jet Quenching in Dense Matter". In: Phys. Lett. B 243 (1990), pp. 432–438. DOI: 10.1016/0370-2693(90)91409-5.

[4] R. Baier et al. "Radiative energy loss of high-energy quarks and gluons in a finite volume quark - gluon plasma". In: Nucl. Phys. B 483 (1997), pp. 291–320. DOI: 10.1016/S0550-3213(96)00553-6. arXiv: hep-ph/9607355.

[5] Urs Achim Wiedemann. "Transverse dynamics of hard partons in nuclear media and the QCD dipole". In: Nucl. Phys. B 582 (2000), pp. 409–450. DOI: 10.1016/S0550-3213(00)00286-8. arXiv: hep-ph/0003021.

[6] Xin-Nian Wang and Xiao-feng Guo. "Multiple parton scattering in nuclei: Parton energy loss". In: Nucl. Phys. A 696 (2001), pp. 788–832. DOI: 10.1016/S0375-9474(01)01130-7. arXiv: hep-ph/0102230.

[7] K. Adcox et al. "Suppression of hadrons with large transverse momentum in central Au+Au collisions at $\sqrt{s_{NN}}$ = 130-GeV". In: Phys. Rev. Lett. 88 (2002), p. 022301. DOI: 10.1103/PhysRevLett.88.022301. arXiv: nucl-ex/0109003.

[8] C. Adler et al. "Centrality dependence of high p_T hadron suppression in Au+Au collisions at $\sqrt{s}_{NN}$ = 130-GeV". In: Phys. Rev. Lett. 89 (2002), p. 202301. DOI: 10.1103/PhysRevLett.89.202301. arXiv: nucl-ex/0206011.

[9] A. Adare et al. "Suppression pattern of neutral pions at high transverse momentum in Au+Au collisions at $\sqrt{s_{NN}}$ = 200 GeV and constraints on medium transport coefficients". In: Phys. Rev. Lett. 101 (2008), p. 232301. DOI: 10.1103/PhysRevLett.101.232301. arXiv: 0801.4020 [nucl-ex].

[10] Serguei Chatrchyan et al. "Study of High-pT Charged Particle Suppression in PbPb Compared to pp Collisions at $\sqrt{s_{NN}} = 2.76$ TeV". In: Eur. Phys. J. C 72 (2012), p. 1945. DOI: 10.1140/epjc/s10052-012-1945-x. arXiv: 1202.2554 [nucl-ex].

[11] M. M. Aggarwal et al. "Suppression of High-p_T Neutral Pions in Central Pb + Pb Collisions at $\sqrt{s_{NN}} = 17.3$ GeV Relative to p + C and p + Pb Collisions". In: Phys. Rev. Lett. 100 (2008), p. 242301. DOI: 10.1103/PhysRevLett.100.242301. arXiv: 0708.2630 [nucl-ex].

[12] Miklos Gyulassy and Larry McLerran. "New forms of QCD matter discovered at RHIC". In: Nucl. Phys. A 750 (2005). Ed. by D. Rischke and G. Levin, pp. 30–63. DOI: 10.1016/j.nuclphysa.2004.10.034. arXiv: nucl-th/0405013.

[13] Simon Turbide et al. "Electromagnetic radiation from nuclear collisions at RHIC energies". In: Phys. Rev. C 77 (2008), p. 024909. DOI: 10.1103/PhysRevC.77.024909. arXiv: 0712.0732 [hep-ph].

[14] I. M. Chertok. "On the correlation between the solar gamma-ray line emission". In: Astronomische Nachrichten 311 (Oct. 1990), pp. 379–381. DOI: 10.1002/asna.2113110608.

[15] Paul A. M. Dirac. "The quantum theory of the electron". In: Proc 117 (1928), pp. 610–624. DOI: {10.1098/rspa.1928.0023}.

[16] P. Aurenche et al. "Prompt Photon Production at Large p(T) Scheme Invariant QCD Predictions and Comparison with Experiment". In: Nucl. Phys. B 297 (1988), pp. 661–696. DOI: 10.1016/0550-3213(88)90553-6.

[17] Siegfried Bethke. "Experimental tests of asymptotic freedom". In: Prog.Part 58 (2007), pp. 351–386. DOI: {10.1016/j.ppnp.2006.06.001}. arXiv: hep-ex/0606035.

[18] J. Beringer et al. "Review of Particle Physics (RPP)". In: Phys. Rev. D 86 (2012), p. 010001. DOI: 10.1103/PhysRevD.86.010001.

[19] David J. Gross and Frank Wilczek. "Ultraviolet Behavior of Nonabelian Gauge Theories". In: Phys. Rev. Lett. 30 (1973). Ed. by J. C. Taylor, pp. 1343–1346. DOI: 10.1103/PhysRevLett.30.1343.

[20] J. J. Aubert et al. "Experimental Observation of a Heavy Particle J". In: Phys. Rev. Lett. 33 (1974), pp. 1404–1406. DOI: 10.1103/PhysRevLett.33.1404.

[21] G. F. Chapline et al. "Highly excited nuclear matter". In: Phys. Rev. D 8 (1973), pp. 4302–4308. DOI: 10.1103/PhysRevD.8.4302.

[22] Peter F. Kolb and Ralf Rapp. "Transverse flow and hadrochemistry in Au+Au collisions at (S(NN))**(1/2) = 200-GeV". In: Phys. Rev. C 67 (2003), p. 044903. DOI: 10.1103/PhysRevC.67.044903. arXiv: hep-ph/0210222.

[23] T. D. Lee. "Abnormal Nuclear States and Vacuum Excitations". In: Rev. Mod 47 (1975). Ed. by G. Feinberg, pp. 267–275. DOI: {10.1103/RevModPhys.47.267}.

[24] John C. Collins and M. J. Perry. "Superdense Matter: Neutrons Or Asymptotically Free Quarks?" In: Phys. Rev. Lett. 34 (1975), p. 1353. DOI: 10.1103/PhysRevLett.34.1353.

[25] Edward V Shuryak. "Quantum chromodynamics and the theory of superdense matter". In: Physics Reports 61.2 (1980), pp. 71–158.

[26] Tadaaki Isobe. "Production of Direct Photons and Neutral Pions in Relativistic Au + Au Collisions". PhD thesis. Tokyo U., 2007.

[27] K. Adcox et al. "PHENIX detector overview". In: Nucl. Instrum. Meth. A 499 (2003), pp. 469–479. DOI: {10.1016/S0168-9002(02)01950-2}.

[28] K. H. Ackermann et al. "STAR detector overview". In: Nucl. Instrum. Meth. A 499 (2003), pp. 624–632. DOI: 10.1016/S0168-9002(02)01960-5.

[29] B. B Back et al. "The PHOBOS detector at RHIC". In: Nucl. Instrum. Meth. A 499 (2003), pp. 603–623. DOI: {10.1016/S0168-9002(02)01959-9}.

[30] M Adamczyk et al. "The BRAHMS experiment at RHIC". In: Nucl. Instrum. 499 (2003), pp. 437–468. DOI: {10.1016/S0168-9002(02)01949-6}.

[31] Nowo Riveli. "Direct Photon - Hadron Correlations Measurement in Au+Au Collision at Nucleon Center-Of-Mass Energy of 200 GeV With Isolation Cut Methods". PhD thesis. Ohio University, 2014.

[32] U.S. Department of Energy, Office of Science, Office of Nuclear Physics. The 2007 Long Range Plan for the Nuclear Physics Research Program. Retrieved fromhttps://www.osti.gov/servlets/purl/927374. 2007.

[33] S. A. Bass et al. "Signatures of quark gluon plasma formation in high-energy heavy ion collisions: A Critical review". In: J. Phys. G 25 (1999), R1–R57. DOI: 10.1088/0954-3899/25/3/013. arXiv: hep-ph/9810281.

[34] C. Y. Wong. Introduction to high-energy heavy ion collisions. 1995. ISBN: 978-981-02-0263-7.

[35] K. Adcox et al. "Centrality dependence of the high p(T) charged hadron suppression in Au+Au collisions at s(NN)**(1/2) = 130-GeV". In: Phys. Lett. 561 (2003), pp. 82–92. DOI: 10.1016/S0370-2693(03)00423-4. arXiv: nucl-ex/0207009.

[36] David d'Enterria. "Jet quenching in QCD matter: From RHIC to LHC". In: Nucl. Phys. A 827 (2009). Ed. by Itzhak Tserruya, Avraham Gal, and Daniel Ashery, pp. 356C–364C. DOI: 10.1016/j.nuclphysa.2009.05.078. arXiv: 0902.2488 [nucl-ex].

[37] R. Baier et al. "Induced gluon radiation in a QCD medium". In: Phys. Lett. B 345 (1995), pp. 277–286. DOI: 10.1016/0370-2693(94)01617-L. arXiv: hep-ph/9411409.

[38] PHENIX Collaboration. "Suppression of High Transverse Momentum π^0 Production in Central Au+Au Collisions at $\sqrt{s_{NN}} = 200$ GeV". In: Phys. Rev 91 (2003), p. 072301.

[39] PHENIX Collaboration. "Enhanced Production of Low Momentum π^0 in Central Au+Au Collisions at $\sqrt{s_{NN}}$ = 200 GeV". In: Phys. Rev. Lett. 101 (2008), p. 232301.

[40] A. Adare et al. "Dihadron azimuthal correlations in Au+Au collisions at $\sqrt{s_{NN}}$ = 200 GeV". In: Phys. Rev. C 78 (2008), p. 014901. DOI: 10.1103/PhysRevC.78.014901. arXiv: 0801.4545 [nucl-ex].

[41] C. Adler et al. "Disappearance of back-to-back high p_T hadron correlations in central Au+Au collisions at $\sqrt{s_{NN}}$ = 200-GeV". In: Phys. Rev. Lett. 90 (2003), p. 082302. DOI: 10.1103/PhysRevLett.90.082302. arXiv: nucl-ex/0210033.

[42] G. L. Bayatian et al. "CMS technical design report, volume II: Physics performance". In: J. Phys. G 34.6 (2007), pp. 995–1579. DOI: 10.1088/0954-3899/34/6/S01.

[43] Sanshiro Mizuno. "Measurements of Direct Photon Higher Order Azimuthal Anisotropy in $\sqrt{S_{NN}}$ = 200 GeV Au + Au Collisions at RHIC-PHENIX". PhD thesis. Tsukuba U., 2015.

[44] S. S. Adler et al. "High transverse momentum η meson production in p^+p, d^+ Au and Au+Au collisions at $S(NN)^{(1/2)}$ = 200-GeV". In: Phys. Rev. C 75 (2007), p. 024909. DOI: 10.1103/PhysRevC.75.024909. arXiv: nucl-ex/0611006.

[45] Rishi Sharma. "Quarkonium propagation in the quark–gluon plasma". In: Eur. Phys. J. ST 230.3 (2021), pp. 697–718. DOI: 10.1140/epjs/s11734-021-00025-z. arXiv: 2101.04268 [hep-ph].

[46] F. Michler, B. Schenke, and C. Greiner. "Finite lifetime effects on the photon production from a quark-gluon plasma". In: June 2009. arXiv: 0906.1734 [hep-ph].

[47] Simon Turbide, Ralf Rapp, and Charles Gale. "Hadronic production of thermal photons". In: Phys. Rev. C 69 (1 Jan. 2004), p. 014903. DOI: 10.1103/PhysRevC.69.014903. URL: https://link.aps.org/doi/10.1103/PhysRevC.69.014903.

[48] Matthew Nguyen. "Two Particle Correlations with Direct Photon and π^0 Triggers in 200 GeV p+p and Au+Au Collisions". PhD thesis. SUNY, Stony Brook, 2009.

[49] A Drees. "Electromagnetic radiation probing hot and dense nuclear matter". In: Nuclear Physics A 630.1-2 (1998), pp. 449–460.

[50] G. Sozzi et al. "Direct photon production in $\bar{p}p$ and pp interactions at $\sqrt{s}$ = 24.3-GeV". In: Phys. Lett. B 317 (1993), pp. 243–249. DOI: 10.1016/0370-2693(93)91600-R.

[51] G Ballocchi et al. "Direct photon cross-sections in proton proton and anti-proton - proton interactions at S**(1/2) = 24.3-GeV". In: Phys. Lett. B 436 (1998), pp. 222–230. DOI: 10.1016/S0370-2693(98)01001-6.

[52] M. Bonesini et al. "Production of High Transverse Momentum Prompt Photons and Neutral Pions in Proton Proton Interactions at 280-GeV/c". In: Z. Phys. C 38 (1988), p. 371. DOI: 10.1007/BF01584385.

[53] C. De Marzo et al. "A Measurement of Direct Photon Production at Large Transverse Momentum in $\pi^- p$, $\pi^+ p$ and pp Collisions at 300-GeV/c". In: Phys. Rev. D 36 (1987), p. 8. DOI: 10.1103/PhysRevD.36.8.

[54] A. L. S. Angelis et al. "Direct Photon Production at the CERN ISR". In: Nucl. Phys. B 327 (1989), pp. 541–568. DOI: 10.1016/0550-3213(89)90305-2.

[55] E. Anassontzis et al. "High p(t) Direct Photon Production in p p Collisions". In: Z. Phys. C 13 (1982), pp. 277–289. DOI: 10.1007/BF01572345.

[56] L. Apanasevich et al. "Measurement of direct photon production at Tevatron fixed target energies". In: Phys. Rev. D 70 (2004), p. 092009. DOI: 10.1103/PhysRevD.70.092009. arXiv: hep-ex/0407011.

[57] C. Albajar et al. "Direct Photon Production at the CERN Proton - anti-Proton Collider". In: Phys. Lett. B 209 (1988), pp. 385–396. DOI: 10.1016/0370-2693(88)90968-9.

[58] J. Alitti et al. "A Measurement of single and double prompt photon production at the CERN $\bar{p}p$ collider". In: Phys. Lett. B 288 (1992), pp. 386–394. DOI: 10.1016/0370-2693(92)91118-S.

[59] F. Abe et al. "A Precision measurement of the prompt photon cross-section in $p\bar{p}$ collisions at $\sqrt{s}$ = 1.8 TeV". In: Phys. Rev. Lett. 73 (1994). [Erratum: Phys.Rev.Lett. 74, 1891–1893 (1995)], pp. 2662–2666. DOI: 10.1103/PhysRevLett.73.2662.

[60] S. Abachi et al. "Isolated photon cross-section in the central and forward rapidity regions in $p\bar{p}$ collisions at $\sqrt{s}$ = 1.8 TeV". In: Phys. Rev. Lett. 77 (1996), pp. 5011–5015. DOI: 10.1103/PhysRevLett.77.5011. arXiv: hep-ex/9603006.

[61] P. Aurenche et al. "A Critical phenomenological study of inclusive photon production in hadronic collisions". In: Eur. Phys. J. C 9 (1999), pp. 107–119. DOI: 10.1007/s100529900018. arXiv: hep-ph/9811382.

[62] Thomas Peitzmann and Markus H. Thoma. "Direct photons from relativistic heavy ion collisions". In: Phys. Rept. 364 (2002), pp. 175–246. DOI: 10.1016/S0370-1573(02)00012-1. arXiv: hep-ph/0111114.

[63] W. Vogelsang and M. R. Whalley. "A Compilation of data on single and double prompt photon production in hadron hadron interactions". In: J. Phys. G 23 (1997), A1–A69. DOI: 10.1088/0954-3899/23/7A/001.

[64] T. Åkesson et al. "Inclusive Photon Production in P a and A-a Collisions at 200-GeV/u". In: Z. Phys. C 46 (1990), pp. 369–376. DOI: 10.1007/BF01621024.

[65] R. Albrecht et al. "Upper limit for thermal direct photon production in heavy ion collisions at 60-A/GeV and 200-A/GeV". In: Z. Phys. C 51 (1991), pp. 1–10. DOI: 10.1007/BF01579555.

[66] R. Baur et al. "Search for direct photons from S - Au collisions at 200-GeV/u". In: Z. Phys. C 71 (1996), pp. 571–578. DOI: 10.1007/s002880050204.

[67] M. M. Aggarwal et al. "Direct photon production in 158-A-GeV Pb-208 + Pb-208 collisions". In: (June 2000). arXiv: nucl-ex/0006007.

[68] Jan-e Alam et al. "Photons from Pb Pb collisions at CERN SPS". In: Phys. Rev. C 63 (2001), p. 021901. DOI: {10.1103/PhysRevC.63.021901}. arXiv: hep-ph/0008074.

[69] A. Dumitru et al. "Nuclear broadening effects on hard prompt photons at relativistic energies". In: Phys. Rev. C 64 (2001), p. 054909. DOI: 10.1103/PhysRevC.64.054909. arXiv: hep-ph/0103203.

[70] K. Gallmeister, Burkhard Kampfer, and O. P. Pavlenko. "A Unique large thermal source of real and virtual photons in the reactions Pb-158-A/GeV + Pb, Au". In: Phys. Rev. C 62 (2000), p. 057901. DOI: 10.1103/PhysRevC.62.057901. arXiv: hep-ph/0006134.

[71] P. Huovinen, P. V. Ruuskanen, and S. S. Rasanen. "Photon emission in heavy ion collisions at the CERN SPS". In: Phys. Lett. B 535 (2002), pp. 109–116. DOI: 10.1016/S0370-2693(02)01721-5. arXiv: nucl-th/0111052.

[72] Dinesh Kumar Srivastava and Bikash Sinha. "Radiation of single photons from Pb + Pb collisions at the CERN SPS and quark hadron phase transition". In: Phys. Rev. C 64 (2001), p. 034902. DOI: 10.1103/PhysRevC.64.034902. arXiv: nucl-th/0006018.

[73] Jan-e Alam et al. "Photon interferometry and size of the hot zone in relativistic heavy ion collisions". In: Phys. Rev. C 67 (2003), p. 054902. DOI: 10.1103/PhysRevC.67.054902. arXiv: nucl-th/0302054.

[74] Gergely G. Barnafoldi et al. "High P(T) pion production in heavy ion collisions at RHIC energies". In: 32nd International Symposium. Dec. 2002, pp. 145–148. DOI: {10.1142/9789812704962_0029}. arXiv: nucl-th/0212111.

[75] Dinesh Kumar Srivastava. "Intensity interferometry of thermal photons from relativistic heavy ion collisions". In: Phys. Rev. C 71 (2005), p. 034905. DOI: 10.1103/PhysRevC.71.034905. arXiv: nucl-th/0411041.

[76] H. Hahn et al. "The RHIC design overview". In: Nucl. Instrum. Meth. A 499 (2003), pp. 245–263. DOI: 10.1016/S0168-9002(02)01938-1.

[77] In: (). DOI: \url{https://science.osti.gov/np/Facilities/User-Facilities/RHIC}.

[78] Brookhaven National Laboratory. "RHIC Runs". In: (). Accessed: 2024-06-30.

[79] K Adcox et al. "PHENIX detector overview". In: Nuclear Instruments 499.2-3 (2003), pp. 469–479.

[80] K. Adcox et al. “Construction and performance of the PHENIX pad chambers”. In: Nucl. Instrum. Meth. A 497 (2003), pp. 263–293. DOI: 10.1016/S0168-9002(02)01791-6.

[81] K. Adcox et al. “PHENIX central arm tracking detectors”. In: Nucl. Instrum 499 (2003), pp. 489–507. DOI: {10.1016/S0168-9002(02)01952-6}.

[82] Y. Akiba et al. “Ring imaging Cherenkov detector of PHENIX experiment at RHIC”. In: Nucl. Instrum. Meth. A 433 (1999). Ed. by A. Breskin, R. Chechik, and T. Ypsilantis, pp. 143–148. DOI: 10.1016/S0168-9002(99)00319-8.

[83] L Aphecetche et al. “PHENIX calorimeter”. In: Nucl. Instrum. Meth. A 499 (2003), pp. 521–536. DOI: 10.1016/S0168-9002(02)01954-X.

[84] H. Gong. “Measurement of Direct Photons in Ultra-Relativistic Au+Au Collisions.” In: Zenodo. (2014). DOI: 10.5281/zenodo.4430119..

[85] WA98 Collaboration. CERN Report No. SPSLC 91-17. Tech. rep. SPSLC 91-17. CERN, 1991.

[86] T. C. Awes et al. “High-energy beam test of the PHENIX lead scintillator EM calorimeter”. In: (Feb. 2002). arXiv: nucl-ex/0202009.

[87] In: (). URL: https://www.phenix.bnl.gov/experiment/trigger.html.

[88] In: (). URL: Technical%20Note:%20Calibration%20of%20EMCal%20ToF%20in%20Run-14%20Au+Au%20collisions%20at%20$%5Csqrt%7B%7B200%7D%7D$%20GeV..

[89] In: (). URL: https://phenix-intra.sdcc.bnl.gov/phenix/WWW/offline/wikioff/index.php/THmulf.

[90] In: (). URL: Technical%20Note:%20tn488.0,%20Calibration%20of%20EMCal%20ToF%20in%20Run-16%20Au+Au%20collisions%20at%20$%5Csqrt%7Bs_%7BNN%7D%7D=200$%20GeV..

[91] Stephen Adler and Y. Aronson. “Centrality Dependence of ÏÂ° and Î· Production at Large Transverse Momentum in â(ssub NN)=200 GeV d+Au Collisions”. In: Physical Review Letters - PHYS REV LETT 98 (Apr. 2007), pp. 172302–172302. DOI: 10.1103/PHYSREVLETT.98.172302.

[92] O. Malandraki. “Solar Energetic Particles and Space Weather: Science and Applications”. In: Solar Particle Radiation Storms Forecasting and Analysis. National Observatory of Athens, 2018, pp. 1–26. DOI: 10.1007/978-3-319-60051-2_1.

[93] S. Eren et al. “Flare-production potential associated with different sunspot groups”. In: Monthly Notices of the Royal Astronomical Society 465.1 (2017), pp. 68–75. DOI: 10.1093/mnras/stw2752.

[94] C. O. G. Waterfall et al. “High energy solar particle events and their relationship to associated flare, CME and GLE parameters”. In: Space Weather 21.3 (2023), e2022SW003334. DOI: 10.1029/2022SW003334. URL: https://doi.org/10.1029/2022SW003334.

[95] H. V. Cane, R. E. McGuire, and T. T. von Rosenvinge. "Two classes of solar energetic particle events associated with impulsive and long-duration soft X-ray flares". In: The Astrophysical Journal 301 (1986), pp. 448–459. DOI: 10.1086/163913. URL: https://doi.org/10.1086/163913.

[96] D. V. Reames. "Particle Acceleration at the Sun and in the Heliosphere". In: Space Science Reviews 90 (1999), pp. 413–491. DOI: 10.1023/A:1005105831781. URL: https://doi.org/10.1023/A:1005105831781.

[97] N. Gopalswamy. "Coronal Mass Ejections and Solar Radio Emissions". In: Planetary and Space Science 70 (2012), pp. 1–9. DOI: 10.1016/j.pss.2012.05.023. URL: https://doi.org/10.1016/j.pss.2012.05.023.

[98] M. A. Shea and D. F. Smart. "Fifty Years of Cosmic Radiation Data". In: Space Science Reviews 93 (2000), pp. 229–262. DOI: 10.1023/A:1026561301132. URL: https://doi.org/10.1023/A:1026561301132.

[99] E. W. Cliver, E. D'Huys, and N. B. Crosby. "CMEs and Ground Level Enhancement Events". In: Advances in Space Research 38 (2006), pp. 441–449. DOI: 10.1016/j.asr.2005.05.090. URL: https://doi.org/10.1016/j.asr.2005.05.090.

[100] J. Zhang et al. "Earth-Affected Solar Transients: A review of progresses in solar cycle 24". In: Progress in Earth and Planetary Science 8.1 (2021), p. 56. DOI: 10.1186/s40645-021-00426-7. URL: https://doi.org/10.1186/s40645-021-00426-7.

APPENDIX A

1 Good Run List for Run 14 Taxi Job

Run Number	Run Number	Run Number	Run Number
405864	405868	405869	405966
405972	405977	405981	405982
405990	405996	406089	406090
406093	406094	406099	406180
406182	406190	406259	406265
406268	406539	406540	406543
406544	406549	406555	406579
406581	406582	406584	406661
406662	406663	406666	406671
406674	406675	406676	406677
406696	406697	406698	406700
406745	406746	406747	406753
406754	406761	406762	406766
406767	406773	406830	406832
406833	406848	406849	406850
406851	406853	406857	406858
406859	406861	406869	406871
406881	406882	406889	406893
406898	406905	406920	406921
407086	407143	407145	407146
407147	407176	407195	407197
407198	407199	407200	407269
407270	407271	407272	407276
407361	407362	407367	407368
407369	407370	407371	407372
407375	407376	407377	407378
407379	407381	407445	407447
407448	407454	407455	407456
407457	407459	407523	407524
407526	407558	407608	407610
407611	407614	407618	407620

407621	407660	407661	407662
407664	407666	407669	407671
407672	407673	407675	407676
407711	407712	407786	407792
407796	407797	407798	407799
407800	407802	407842	407944
407945	407946	407948	407950
407951	407953	407959	407960
407963	407964	407965	407966
408070	408073	408074	408075
408076	408077	408078	408175
408176	408181	408182	408183
408184	408217	408218	408219
408220	408224	408225	408226
408227	408229	408321	408322
408323	408324	408325	408328
408329	408330	408332	408333
408334	408335	408336	408404
408405	408406	408408	408409
408410	408432	408433	408434
408435	408436	408437	408438
408439	408440	408567	408574
408575	408577	408578	408579
408580	408582	408583	408584
408585	408586	408587	408588
408589	408641	408642	408643
408644	408645	408646	408647
408648	408649	408650	408670
408672	408673	408675	408798
408799	408801	408804	408805
408857	408858	408859	408881
408882	408883	408885	408886
408887	408888	408889	408920
408921	408923	408924	408925
408994	408995	408997	408998
408999	409004	409006	409009
409010	409011	409012	409014
409082	409084	409086	409087
409088	409089	409092	409115
409116	409118	409120	409121
409124	409125	409147	409149
409150	409151	409152	409153
409154	409200	409222	409223
409224	409226	409228	409229
409230	409231	409232	409235
409236	409237	409239	409241

409243	409295	409297	409298
409299	409302	409303	409304
409305	409306	409307	409310
409312	409429	409430	409431
409432	409438	409439	409440
409442	409454	409455	409456
409457	409458	409459	409465
409467	409469	409471	409547
409548	409549	409550	409551
409552	409553	409554	409555
409611	409612	409613	409614
409616	409617	409619	409620
409622	409637	409638	409639
409640	409641	409642	409643
409644	409647	409678	409680
409681	409682	409683	409684
409687	409694	409695	409696
409697	409698	409699	409700
409702	409703	409705	409706
409707	409709	409714	409716
409718	409720	409723	409825
409826	409827	409828	409829
409830	409831	409832	409833
409835	409836	409837	409838
409839	409841	409842	409885
409887	409889	409894	409897
409900	409902	409967	409968
409971	409972	409973	409974
409975	409977	410009	410010
410011	410012	410013	410014
410015	410065	410066	410104
410105	410106	410107	410108
410110	410111	410112	410114
410115	410118	410119	410120
410122	410166	410167	410168
410169	410185	410221	410222
410224	410225	410226	410227
410228	410230	410231	410261
410262	410263	410265	410266
410267	410653	410654	410655
410656	410659	410675	410677
410678	410682	410685	410721
410723	410725	410726	410728
410729	410748	410749	410750
410752	410754	410796	410797
410803	410808	410810	410835

410836	410838	410842	410843
410920	410921	410922	410924
410929	410937	410938	410939
410940	410941	410942	410943
410944	411008	411009	411010
411011	411012	411013	411014
411015	411018	411019	411020
411022	411024	411025	411139
411154	411155	411159	411173
411266	411267	411269	411270
411271	411272	411273	411274
411275	411276	411349	411350
411351	411352	411354	411356
411404	411423	411425	411456
411458	411459	411460	411461
411462	411497	411500	411502
411503	411506	411507	411508
411509	411540	411541	411542
411543	411544	411545	411551
411553	411554	411555	411556
411557	411558	411559	411561
411596	411597	411598	411599
411600	411601	411602	411635
411636	411637	411638	411639
411640	411643	411644	411651
411763	411817	411818	411823
411826	411912	411913	411914
411915	411918	411922	411924
411925	411926	411991	411993
411994	411995	412065	412067
412068	412069	412092	412093
412094	412148	412150	412214
412215	412216	412317	412318
412319	412320	412321	412322
412324	412328	412329	412410
412411	412412	412413	412414
412415	412416	412419	412424
412426	412427	412428	412429
412430	412431	412433	412483
412484	412485	412486	412487
412488	412489	412490	412491
412512	412514	412515	412516
412517	412518	412519	412520
412521	412646	412647	412648
412705	412706	412708	412709
412742	412745	412804	412805

412806	412807	412808	412836
412841	412842	412848	412849
412850	412851	412878	412879
412883	412884	412932	412933
412934	412979	412984	412985
412986	412988	412990	412994
413074	413075	413076	413080
413081	413086	413087	413090
413092	413142	413144	413150
413151	413154	413155	413157
413158	413160	413162	413163
413164	413165	413183	413187
413240	413241	413242	413243
413264	413265	413267	413268
413382	413383	413384	413392
413435	413436	413439	413440
413508	413513	413539	413540
413541	413546	413549	413551
413552	413553	413555	413556
413560	413561	413562	413563
413564	413604	413608	413609
413610	413611	413612	413631
413633	413636	413638	413639
413642	413643	413662	413663
413664	413665	413667	413669
413672	413708	413709	413710
413712	413715	413716	413717
413721	413722	413723	413747
413748	413749	413753	413755
413756	413843	413844	413924
413925	413926	413927	413933
413936	413940	414049	414050
414052	414053	414059	414060
414061	414071	414072	414073
414074	414075	414076	414078
414079	414132	414133	414134
414135	414136	414138	414140
414148	414152	414153	414154
414157	414186	414187	414191
414195	414196	414197	414198
414200	414201	414202	414203
414205	414206	414207	414284
414425	414427	414428	414430
414431	414432	414434	414499
414505	414511	414512	414515
414517	414518	414519	414520

414557	414559	414560	414562
414563	414564	414565	414599
414604	414605	414606	414608
414626	414627	414629	414631
414632	414633	414634	414635
414636	414702	414703	414704
414705	414706	414707	414726
414728	414729	414731	414824
414825	414826	414827	414828
414829	414830	414832	414847
414848	414849	414850	414851
414852	414853	414854	414855
414857	414884	414885	414886
414887	414888	414889	414890
414893	414899	414976	414978
414980	414981	414985	414986
414987			

2 Bad Run List for Run 14 Taxi Job

Run Number	Run Number	Run Number	Run Number
405860	409225	405961	405962
405863	405865	412090	405964
409227	405971	412097	412098
405973	412099	405975	412149
405984	409244	405995	406087
406088	409300	409301	406095
412326	409308	406181	412407
409311	406183	409313	406257
409428	406258	406261	412417
409435	409436	409437	406546
409443	406556	412523	412651
412652	412655	406760	412707
406764	412743	406769	406772
406774	406831	412843	412847
409688	411992	414982	406866
406867	406870	406872	406887
413079	406891	406902	407175
407178	407196	409840	409890
409892	409893	413512	413542
413543	413544	413557	413603
413605	413607	410156	407670
413634	407790	413666	407839
410668	410670	410679	410680
413724	410718	413751	410720
410722	410724	408071	413932
413934	410753	408177	414048
410759	410800	410802	408218
410837	414077	410840	410923
414149	414151	414156	414158
414204	408566	411152	414285
414309	408572	414310	408573
411156	414311	414312	414327
414328	414329	411268	414330
414331	414332	414334	414335
414336	414337	414338	411277
414339	414340	408592	414424
411353	411411	411419	411422
414507	408671	408802	411501
411504	408860	408996	411645
411652	411764	411921	411767
411819	411825	409123	414892
411916	414979		

APPENDIX B

3 Code locations for this study

This analysis's ROOT files and plotting macros are safely backed up on HPSS at this path:
hsi
`/home/nourja/phd/phd.tar`

The files are also located in my user directory as the following:

3.1 The taxi module and macros

- Mainpath:/gpfs/mnt/gpfs02/phenix/plhf/plhf1/nourja/taxi/
- Dataset:
- Mainpath/Run14AuAu200CAnVXMBP106/19894
- Mainpath/Run14AuAu200CAnVXERTP106/19895
- CVS module:
- /offline/AnalysisTrain/Run14AuAu_nourPi0Photon
- Macro:
- /offline/AnalysisTrain/pat/macro/Run_Run14AuAu_nourPi0Photon.C
- /offline/AnalysisTrain/Run14AuAu_nourPi0Photon/Combination.cc
- /offline/AnalysisTrain/Run14AuAu_nourPi0Photon/KCluster.cc
- /offline/AnalysisTrain/Run14AuAu_nourPi0Photon/RecalEMCalTOF.cc
- /offline/AnalysisTrain/Run14AuAu_nourPi0Photon/KEvent.cc

3.2 DHM Calibration

- Mainpath:/gpfs/mnt/gpfs02/phenix/plhf/plhf1/nourja/Run14AuAuDHM/phd
- MainPath/DHM/STEP1/preCheck.C
- MainPath/DHM/STEP2/individualDHM.C & creatPlotsForAuAu.C
- MainPath/DHM/STEP3/DHM.C
- MainPath/DHM/STEP4/unionE.C
- MainPath/DHM/STEP5/energyStudy.C & runCheckForAuAu.C
- MainPath/DHM/STEP6/percentChangesAuAu.C
- MainPath/DHM/STEP7/plotFinalDHMAuAu.C
- MainPath/DHM/STEP8/finalEnergyBinCheck.C & findMissingRunAuAu.C & findMissingRunForCluster.

3.3 Timing Calibration

- MainPath/TIMING/1st_step/estimateBinning.C & rebin.C & preRebin.C
- MainPath/TIMING/2nd_step/fit.C
- MainPath/TIMING/3rd_step/secbysec.C
- MainPath/TIMING/4th_step/rebinwithrunsec.C
- MainPath/TIMING/5th_step/fitwithrunsec.C
- MainPath/TIMING/MB_ERT/TofvsRunno.C

3.4 Raw π^0 Extractions

- MainPath/ANALYSIS_NOTE/Pi0_Extraction/1st_Step/MergeExample.job & MergeExample.sh
- MainPath/ANALYSIS_NOTE/Pi0_Extraction/2nd_Step/Pi0ExtractionExample.C & Pi0extract.job & Pi0extract.sh & Ratio_Run14_Run16.C
- MainPath/ANALYSIS_NOTE/Pi0_Extraction/3rd_Step/ Ratio_Norm_ERT_MB.C
- MainPath/ANALYSIS_NOTE/Pi0_Extraction/4th_Step/ Ratio_AuAu_raw_pi01.C

3.5 Raw π^0 Window Study

- MainPath/pi0windowStudy/Extract/07_20
- MainPath/pi0windowStudy/Extract/08_19
- MainPath/pi0windowStudy/Extract/09_18
- MainPath/pi0windowStudy/Combine/0720
- MainPath/pi0windowStudy/Combine/0819
- MainPath/pi0windowStudy/Combine/0918
- MainPath/pi0windowStudy/Pi0Unfolding
- MainPath/pi0windowStudy/SYS_WINDOW

3.6 Raw inclusive γ

- MainPath/ANALYSIS_NOTE/INC_PHOTON/1st_Step/
  Gammaextract_0210.C & Gammaextract.job & Gammaextract.sh
- MainPath/ANALYSIS_NOTE/INC_PHOTON/2nd_Step/
  rawGamma_20220414.C & rawGamma.sh
- MainPath/ANALYSIS_NOTE/INC_PHOTON/3rd_Step/
  RatioOfGamma_MB_ERT.C
- MainPath/ANALYSIS_NOTE/INC_PHOTON/4th_Step /
  Ratio_gamma_Run14_Run16.C

3.7 π^0 Simulation

- MainPath/ANALYSIS_NOTE/Pi0_Simulation/1st_Step/all_new_result.root
  & PisaEmbed.csh & PisaEmbed.job
- MainPath/ANALYSIS_NOTE/Pi0_Simulation/2nd_Step/myEmbedPi0NoWeight.C
  & ratio2dMatrix_Run14and16.C
- MainPath/ANALYSIS_NOTE/Pi0_Simulation/3rd_Step/
  By_Point/Pi0_Point_corr.C
- MainPath/ANALYSIS_NOTE/Pi0_Simulation/3rd_Step/Fitting/
  Pi0Correction_last.C
- MainPath/ANALYSIS_NOTE/Pi0_Simulation/3rd_Step/power_law_fit/
  power_law_fit.C
- MainPath/ANALYSIS_NOTE/Pi0_Simulation/4th_Step/run4_14/Yield_inv.py
  & PionpT_Run4_14.C

3.8 Direct Photon Simulation

- Mainpath/phd/ANALYSIS_NOTE/Direct_Photon_Simulation/1st_Step/ 4_pisaNembed_gamma.csh & 4_pisaNembed_gamma.job & all_new_result.root
- Mainpath/phd/ANALYSIS_NOTE/Direct_Photon_Simulation/2nd_Step/ myEmbedGammapAu_new_new.C & myEmbedGammapAu.h
- Mainpath/phd/ANALYSIS_NOTE/Direct_Photon_Simulation/3rd_Step/ CorrPi0_2D_DecayGamma.C & myEmbedPi0pAu.h & Pi0_DecayGammaMatrix.C
- Mainpath/phd/ANALYSIS_NOTE/Direct_Photon_Simulation/4th_Step/ GammaCorrection_for_new_simu.C
- Mainpath/phd/ANALYSIS_NOTE/Direct_Photon_Simulation/5th_Step/ photonpT_139_14.C

3.9 π^0 Systematic Uncertainties

- MainPath/ANALYSIS_NOTE/Pi0_Simulation/5th_Step/SYS_CORR_pi01.C
- MainPath/ANALYSIS_NOTE/Pi0_Simulation/5th_Step/SYS_CORR_pi02.C
- MainPath/ANALYSIS_NOTE/Pi0_Simulation/5th_Step/SYS_CORR_pi03.C

3.10 γ Systematic Uncertainties

- Mainpath/phd/ANALYSIS_NOTE/Direct_Photon_Simulation/6th_Step/ SYS1_CORR_photon.C
- Mainpath/phd/ANALYSIS_NOTE/Direct_Photon_Simulation/6th_Step/ SYS2_CORR_photon.C